ISTANBUL TECHNICAL UNIVERSITY ★ GRADUATE SCHOOL OF SCIENCE ENGINEERING AND TECHNOLOGY

A NOVEL AAO BASED SERS SUBSTRATE FOR CHARACTERIZATION OF PROTEINS

Ph.D. THESIS

Zehra Beril AKINCI

Department of Materials Science and Engineering

Materials Science and Engineering Programme

DECEMBER 2013

ISTANBUL TECHNICAL UNIVERSITY ★ GRADUATE SCHOOL OF SCIENCE ENGINEERING AND TECHNOLOGY

A NOVEL AAO BASED SERS SUBSTRATE FOR CHARACTERIZATION OF PROTEINS

Ph.D. THESIS

Zehra Beril AKINCI
(521072004)

Department of Materials Science and Engineering

Materials Science and Engineering Programme

Thesis Advisor: Prof. Dr. Mustafa URGEN
Co-Advisor: Prof. Dr. Candan TAMERLER

DECEMBER 2013

İSTANBUL TEKNİK ÜNİVERSİTESİ ★ FEN BİLİMLERİ ENSTİTÜSÜ

YÜZEYCE GÜÇLENDİRİLMİŞ RAMAN SPEKTROSKOPİSİ İLE PROTEİN KARAKTERİZASYONU İÇİN AAO ŞABLONLAR İLE ALTLIK ÜRETİMİ

Doktora TEZİ

Zehra Beril AKINCI
(521072004)

Malzeme Bilimi ve Mühendisliği Anabilim Dalı

Malzeme Bilimi ve Mühendisliği Programı

Tez Danışmanı: Prof. Dr. Mustafa ÜRGEN
Eş Danışman: Prof. Dr. Candan TAMERLER

ARALIK 2013

To my family,

FOREWORD

It has been six years of hard work, endless experiments, dirty lab coats, many chemical, analysing results, repeating the same things everyday for months, failing, feeling clueless and frustrated, then starting all over again and again…

It has also been six years of joy, fun, laughter, good results (or at least promising results), success, making new friendships, seeing new cities …

Through all this time I have met some of the most important people in my life.

First, my advisor, Mustafa Ürgen whom I admire for his limitless curiosity and love of science, and whom I can never thank enough for his support, encouragements and mentoring. I am lucky to have been a student in his courses but I feel honoured to have worked with him for my PhD.

My other advisor, Candan Tamerler who always been my biggest inspiration with her sparkling personality and her curiosity for science. I surely would not have been where I am right now without her help and guidance from the beginning of my academic career.

I have to thank some of the very special people here because without them this thesis could not have been accomplished. I am deeply grateful to Gültekin Göller, for his support both in terms of ideas, facilities and for his trust on me, to Mustafa Çulha, who always took the time to listen and give priceless comments on my work, to Özgür Özer for his open-minded remarks who made me see different side of the things, to Fatma Neşe Kök, for her enthusiasm and encouragements and at last to Mehmet Sarıkaya for his inspirational presence and for what it is worth being the first person who made me want to pursue a scientific career.

A very special thanks is reserved in my heart for Özgür Birer and Barış Yağcı from Koç University. I don't know what would have become this thesis without their help. They opened their lab to me when I most needed it and I am forever indebted to them for their support and trust. They made me feel at home at KUYTAM and I surely did loved working there and felt always welcome.

So many other people have also been part of this thesis in many ways. I would like to thank especially two of them; Kürşat Kazmanlı, who always was there to lend a hand at any subject regardless of the hour or day of the week and Oğuzhan Gürlü, who I knew I could always knock on his door and who I respect deeply for the way he is standing up among all the shambles.

I am thankful to all the staff and to my colleagues of Metallurgical and Materials Engineering department but especially to Talat Tamer Alpak, Seyhan Atik, Hüseyin Sezer, Sevgin Türkeli and to Kübra Yumakgil. Their help made my work so much easier.

Everybody who goes through the dark and difficult days of a PhD knows very well that without help it is impossible to survive those years. This help and support comes in many ways but comes always through some exceptional people. I was lucky to have been surrounded by them, everyday for so long. I want to mention first Deniz Polat, with whom I shared not just the office room but also life's ups and downs and second Önder Güney and Burçak Ebin who kept me always motivated, informed and who provided coffee and so much more to keep me going.

I think that a PhD is not only a series of experiments and hard work but definitely a personal journey also. As you get immersed in this journey everybody around become also part of it through its good and bad times. I can honestly say that only good friends can make it worth going through this journey without loosing your way.

I want to take a moment here and express my gratitude to Senem Donatan. I was lucky to work with her. I was inspired by her. I learned from her.

Ahu Güneş and Deniz Özer were unsought rewards of the Metallurgical and Materials Engineering studies for me. I am blessed to have met them and their existence enlightened my way.

If I learned one thing for sure through those years it is that the most important thing in life is the family. In the end, they are the people you always come home to either it is the family you are born into or the one you make for yourself.

Yasemin Zöngür, Gözde Karakaptan, Pınar Başlar and Tuğba Talınlı are not only good friends, they are my sisters. Harun Başlar and Derin Talınlı are also family to me. I cannot thank them all enough for every time they picked me up when I stumbled and felled and for all the great moments we shared and will share in the future.

My aunt, Betül Kırdar encouraged me, believed in me and has always been an example not only for my PhD but also through all my life. I cannot imagine my life without her. My brother, Burak Akıncı has been by my side all my life and made my life so much richer, beautiful and fun in every possible way.

Finally it is hard to find the proper words to express my gratitude for my dedicated and loving parents. My mom Nilüfer Akıncı and my dad Tahsin Akıncı were always there for me, supported me in every way, morally or financially, respected all my decisions and trusted me. I have always felt privileged to belong to such a big and great family.

September 2013 Z. Beril Akıncı

TABLE OF CONTENTS

Page

FORWORD ..... **ix**
TABLE OF CONTENTS ..... **xi**
ABBREVIATIONS ..... **xiii**
LIST OF TABLES ..... **xv**
LIST OF FIGURES ..... **xvii**
SUMMARY ..... **xxi**
ÖZET ..... **xxiii**
1. INTRODUCTION **1**
2. LITERATURE REVIEW OF RAMAN SPECTROSCOPY **5**
2.1 The Raman Effect 6
2.1.1 Discovery of the Raman Effect 6
2.1.2 Theory and mathematical explanations 10
2.1.3 Instrumentation 17
2.2 Surface Enhanced Raman Spectroscopy (SERS) 21
2.2.1 Overview of SERS 21
2.2.2 Discovery and a basic description of the SERS effect 25
2.2.3 Definition of SERS enhancement factors 26
2.2.4 Enhancement Mechanisms 29
2.3 SERS Substrates 36
2.4 Applications of SERS 40
3. TEMPLATE ASSISTED FABRICATION OF NANOSTRUCTURES **45**
3.1 Introduction 45
3.1.1 Properties of anodic oxide films 47
3.1.2 Methodologies used for barrier layer opening 55
3.2 Materials and Methods 57
3.3 Experimental 57
3.4 Results and discussions 60
3.4.1 Template morphology of AAO films 61
3.4.2 Barrier layer opening and optimization 64
3.4.3 DC electrodeposition of metallic nanowires 73
3.5 Conclusions 81
4. EVALUATION OF GOLD AND SILVER NANOWIRE ARRAYS AS SERS SUBSTRATES **83**
4.1 Introduction 83
4.2 Materials and Methods 84
4.3 Experimental 85
4.4 Results and discussion 86
4.4.1 UV-vis Absorbance characteristics of gold nanowire arrays 88
4.4.2 Evaluation of the effect of the aspect ratio to the SERS properties 90
4.4.3 SERS mapping of Au Nanowire substrates 95
4.4.4 SERS mapping of Au Nanowire substrates 97
4.5 Conclusions 98

5. PROBING THE PROTEIN ORIENTATION ON FREE-STANDING GOLD NANOWIRE ARRAYS BY SERS 101
5.1 Introduction 101
5.1.1 SERS and Biological Molecules 101
5.1.2 Background Information on BSA and on relevant SERS studies of proteins 102
5.2 Materials and Methods 106
5.3 Experimental 107
5.4 Results and discussions 107
5.5 Conclusions 116
6. PROBING PROTEIN STRUCTURE AND ORIENTATION OF GOLD BINDING PEPTIDE (GBP) ON FREE-STANDING GOLD NANOWIRES BY SERS 117
6.1 Introduction 117
6.1.1 Geneteticaly engineered peptides for inorganics (GEPI's) 118
6.1.2 Gold binding peptides (GBPs) 119
6.1.3 Protein behaviour at solid liquid interfaces 123
6.2 Materials and Methods 125
6.3 Experimental 126
6.4 Results and Discussions 126
6.4.1 Raman Spectrum of Solid GBP 129
6.4.2 Assesment of the influence of the solution charge to the adsorption behavior of GBP monitored by SERS 131
6.5 Conclusions 141
7. CONCLUSIONS AND FUTURE PROSPECTS 145
REFERENCES 149
CURRICULUM VITAE 163

ABBREVIATIONS

SERS	**:** Surface Enhanced Raman Spectroscopy
AAO	**:** Anodized Aluminium Oxide
R6G	**:** Rhodamine 6G
AES	**:** Auger Electron Spectroscopy
SAM	**:** Scanning Auger Microscopy
BSA	**:** Bovine Serum Albumin
GEPI	**:** Genetically Engineered Peptide for Inorganics
NMR	**:** Nuclear Magnetic Resonance
LSPR	**:** Localized Surface Plasmon Resonance
GBP	**:** Gold Binding Peptide
OCP	**:** Open Circuit Potential
PZT	**:** Point of Zero Charge

LIST OF TABLES

Page

Table 4.1 : Aspect ratio and interwire gap size variation according to anodization conditions 91
Table 4.2 : Raman and SERS positions of the main R6G peaks and their assignements according to the literature (Baia et al., 2005; Saini et al., 2009)..... 93
Table 5.1 : Band assignment of the Raman spectrum of solid BSA 111
Table 5.2 : Amino acid content of BSA 112
Table 5.3 : Tentative band assignments of BSA SERS bands. 114

Table 6.1: Amide I band positions (cm^{-1}) and their general attributions to the secondary structure of proteins. 128
Table 6.2: Tentative Raman band assignments of solid GBP at pH 7.4. 130
Table 6.3 : Surface and peptide charge conditions according to solution pH. 132

LIST OF FIGURES

Page

Figure 2.1 : Fundamentals of Raman and Krishnan's Experiment. 8
Figure 2.2 : The first Raman spectra (Raman, 1928)..... 9
Figure 2.3 : A schematic Jablonski diagram that illustrates both electronic (bold lines) and rotational/vibrational (thin lines) energy levels. 11
Figure 2.4 : Simplified Jablonski diagrams of Fluorescence process (a) and Rayleigh (b) and Raman (c) scattering. 13
Figure 2.5 : Simplified Jablonski diagrams for Stokes (a) and anti-stokes (b) Raman scattering. 14
Figure 2.6 : a) Oscillation of the dipole moment of the molecule due to incident radiation, b) Change of polarizability resulting in a change in the amplitude of the dipole moment oscillation seen in c, d) Components of the varied amplitude (Larkin, 2011). 15
Figure 2.7 : Schematic representation of Raman Spectrometer. 18
Figure 2.8 : The grating and the CCD detector (www.horiba.com) 21
Figure 2.9 : SERS publication trends over the last ten years. Source web of science with SERS and "Surface Enhanced Raman Spectroscopy" in title or topic. 22
Figure 2.10 : Important steps in the discovery and applications of SERS. 24
Figure 2.11 : SERS Enhancement Mechanisms related to enhancement type (adapted from Miranda et al., 2012). 28
Figure 2.12 : Optical properties of some metals. Real and imaginary parts of the dielectric function are plotted against the wavelength (Dietzek, 2010).32
Figure 2.13 : Schematic represenation of the three different possible chemical enhancement processes. 35
Figure 2.14 : Plasmon resonance wavelenght ranges for SERS supporting three principal metals (Van Duyne et.al., 2012). 36
Figure 3.1 : Schematic diagram showing (a) barrier-type film and (b) porous-type film on aluminum with inner and outer oxide sections (Choi, 2003). .. 48
Figure 3.2 : The schematic representation of the transformation of ideal cylindrical cells to hexagonal close packed array (adapted from Keller et al, 1953). ……..49
Figure 3.3 : A) Structure of AAO and B)Cross-sectional view of the structure (after Sulka, 2008). 50
Figure 3.4 : Current density-anodization time behavior transients of porous layer and barrier layer formations and their schematic representations (adapted after Choi, 2003). 51
Figure 3.5 : The process of field enhanced dissolution and new oxide formation through ionic movements..... 54

Figure 3.6 : Nucleation of smaller pores after controlled voltage reduction, the nset shows schematic representation of the pore perforation after voltage reduction steps (the inset is adapted from Saedi & Ghorbani, 2005). .. 55
Figure 3.7 : Fabrication steps of porous AAO template. A) Annealing, B) Electropolishing, C) 1st step anodization, D) Chemical etching and D) 2nd step anodization. 58
Figure 3.8 : AAO template morphology after the first step anodization 61
Figure 3.9 : The formed pattern on the base of the AAO template after the chemical etching..... 62
Figure 3.10 :AAO template morphology after the second step anodization with distinct hexagonal pore arrays 62
Figure 3.11 : Pore bottom morphology of a porous anodic aluminium oxide template..... 63
Figure 3.12 : A) Formation of AAO template through anodization, B) Zincating of the pore bottoms, C) DC electrodeposition of metallic nanowires on the zincate treated AAO template and D) Freestanding metallic nanowire arrays after the dissolution of AAO and metallic aluminum in an alkaline solution. 65
Figure 3.13 : The surface (a) and cross-sectional (b) micrographs of nanoporous AAO film after the two-step anodization procedure..... 66
Figure 3.14 : Effect of zincate treatment on barrier layer thickness at stagnant conditions at A) 22 °C and B)30 °C. The SEM micrographs shows the barrier layer thikness after 60s sec for A and 40 sec for B. 66
Figure 3.15 : Effect of zincate treatment on barrier layer thickness with ultrasonication at 22 °C and 30 °C zincate bath temperatures. 68
Figure 3.16 : Pore diameter enlargement with zincate treatment time both for 30 °C and 22 °C under ultrasonic conditions. 69
Figure 3.17 : The surface (A) and cross-sectional (B) micrographs of barrier layer thinned nanoporous anodic aluminum oxide film after the two-step anodization procedure. 70
Figure 3.18 : Zincate treatment time effect on barrier layer thickness 20 sec and 30 sec respectively and pore diameter change versus zincate treatment time in barrier layer thinned AAO at 30°C 71
Figure 3.19 : Scanning electron microscopy images of the AAO surface during sputtering process..... 72
Figure 3.20 : Auger scanning electron microscopy results of a zincate treated (45 sec) AAO membrane..... 73
Figure 3.21 : Surface image of electrodeposited nickel nanowire arrays. The inset in the figure shows diameter distribution percentage of the nanowires.... 75
Figure 3.22 : Cross sectional image of the free-standing nickel nanowire array..... 76
Figure 3.23 : Surface and cross-section images of electrodeposited nickel nanowire arrays on a NaOH treated AAO template. 77
Figure 3.24 : Surface image of electrodeposited nickel nanowire arrays.The inset in the figure shows diameter distribution percentage of the nanowires.... 78
Figure 3.25 : Energy dispersive x-ray spectra of the gold nanowire array 78
Figure 3.26 : Cross sectional image of the free-standing gold nanowire array..... 79
Figure 3.27 : General surface view of the free-standing silver nanowire array. 80
Figure 3.28 : Surface view and nanowire diameter size distribution of the silver nanowire array. 80
Figure 3.29 : Cross sectional image of the free-standing silver nanowire array. 81

Figure 4.1 : Absorbance spectra and the molecular structure of Rhodamine 6G molecule (Saini et al., 2009). 84
Figure 4.2 : Schematically explanation of a) propagating surface plasmons on a flat surface and b) localized dipolar surface plasmons on a noble metallic nanoparticle (Aizpurua, 2013). 87
Figure 4.3 : Various nanostructure shapes with different the field distribution patterns, (a) metal sphere in a different medium, (b) metal nanoshell, (c) metal nanoshell presenting an asymmetric Plasmon mode, (d) metal nanorod under polarization parallel to rod axis (e) metal nanorod under polarization perpendicular to rod axis (Wang & Shen, 2006)..... 87
Figure 4.4 : UV-Vis spectrum of freestanding gold nanowire array. 89
Figure 4.5 : Polarization dependence of the SERS spectrum of 10-4M R6G..... 90
Figure 4.6 : Nanowire arrays fabricated through modification of AAO template preparation parameters. A) Array anodized at 60V for 2 min at the second anodization, B) Array anodized at 60V for 5 min at the second anodization, C) Array anodized at 70V for 2 min at the second anodization, D) Array anodized at 70V for 5 min at the second anodization, E) Array anodized at 70V for 7 min at the second anodization and F) Array anodized at 80V for 5 min at the second anodization..... 92
Figure 4.7 : SERS spectrum of 10-5M R6G on gold nanowire array..... 93
Figure 4.8 : Aspect ratio and Raman intensity relationship at 1505 cm^{-1}. Results averaged after 3-consequetive accumulations from different locations over the substrate. 94
Figure 4.9 : SERS spectra of R6G on all substrates with different aspect ratios..... 95
Figure 4.10 : Evaluation of the reusability of the substrates after three consecutive cleanings..... 96
Figure 4.11 : Evaluation of the reproducibility of the results among different substrates produced under the same conditions. 97
Figure 4.12 : Mapping image for the 611 cm-1 band of R6G 98
Figure 4.13 : Mapping image of the same region as in figure 4.10 for the 1340 cm-1 band of R6G..... 98
Figure 5.1 : Crystal structure of BSA showing three different domains and the main tryptophan residue (www.pnas.com)……...105
Figure 5.2 : Free-standing gold nanowire SERS substrate. A) The surface view, B) Cross-section view.....108
Figure 5.3 : Diameter distribution of freestanding gold nanowires.....108
Figure 5.4 : SERS spectrum of 10^{-6}M Rhodamine 6G on gold nanowire array 10^{-1} M Rhodamine 6G on flat gold surface.....109
Figure 5.5 : Raman spectrum of solid BSA……111
Figure 5.6 : SERS of 0.5 mg/mlBSA acquired on Au nanowire substrate.....113
Figure 5.7 : Tentative band assignments of BSA SERS bands. 114
Figure 6.1 : The positionment of GBP on a) {111} gold surface and b) {211} gold surface. Blue residues are polar, green represents charged residues and red residues are the hydrophobic ones (adapted from Braun et al., 2002). 121
Figure 6.2 : Representation of the predicted geometric orientation of 3rGBP1 on the Au{111} surface. The inset shows surface representation of potential

inter-molecular interactions with 3rGBP1 while bound to Au{111}, highlighting free polar (green), nonpolar (white), and cationic (blue) surfaces. The polypeptide backbone is represented in ribbon format (yellow) with docking residues (M1, T11, Q13, S14, T22, S23, T25, and K32, identified along the sequence shown on the top of the figure) (adapted from So et al., 2009). 122
Figure 6.3 : Representation of the amino acid structure, R represents the side chain (a) formation of a covalent peptide bond to form a dipeptide (b) Zwitterionic state formed through ionization of amino acids (c) (Adapted from Stewarts and Fredericks, 1999). 124
Figure 6.4 : Electrical double layer at solid-liquid interface. 125
Figure 6.5 : Raman bands of solid GBP 130
Figure 6.6 : Variation of potential with pH of the gold coated QCM electrode in 100 ml KCL containing phosphate buffer. The slope of the solid line is 5.6 mV per pH unit (Donatan et al., 2011, unpublished data). 132
Figure 6.7 : SERS spectra of GBP at pH 7.4 135
Figure 6.8 : SERS spectra of GBP at pH 4.5 136
Figure 6.9 : Comparison of the solid GBP Raman bands with the SERS spectrum of GBP at pH 4.5 137
Figure 6.10 : SERS spectra of GBP at pH 10.28 138
Figure 6.11 : Comparison of solid GBP Raman bands with the SERS spectra of the GBP at pH 10.28 139
Figure 6.12 : SERS spectra of GBP at pH 12 140
Figure 6.13 : SERS spectrum of GBP at various pH values. All spectrum are background substracted. 141

A NOVEL AAO BASED SERS SUBSTRATE FOR CHARACTERIZATION OF PROTEINS

SUMMARY

The discovery of the Raman effect (and following the Raman spectroscopy technique) was an important step in physical, chemical and analytical sciences. After its discovery there has been a great surge of interest to the field but very soon the weaknesses of the Raman scattering stalled the progress of the technique. In 1974 another equally important breakthrough bridging Raman effect with nanotechnology and materials science has regenerated the scientific public's attention to the subject. The novel technique, named later as "surface enhanced Raman spectroscopy" (SERS), made possible to analyse and detect the Raman signals of even trace amounts of molecules placed in the very close vicinity of noble metallic nanostructures when excited with light. SERS take its route from two separate enhancement mechanisms, which act cumulatively. The first and biggest part of the enhancement comes from the so-called "electromagnetic enhancement" mechanism. The smaller contribution is coming from a chemical (or charge-transfer) enhancement mechanism. Since the electromagnetic mechanism is the biggest contributor to SERS therefore controlling the enhancement through careful tailloration of metallic nanostructures is the key point in fabricating well-performing SERS substrates.

So far, conventional substrates such as electrochemically roughened electrode surface or colloidal suspensions of metallic nanoparticles have all been more or less unsatisfying in the reproducibility issues and reliability of the results. More recently developed substrates through lithographic nanofabrication techniques suffer from complicated and time consuming production procedures requiring expensive equipments. At this point using a template-based approach seems to be the most efficient way of producing a good SERS substrate.

In this dissertation we used a nanoporous template produced by the anodic oxidation of aluminium (AAO) in a suitable electrolyte under appropriate conditions. AAO templates are constituted of hexagonally arranged nanoporous structure with pore bottoms covered by an insulating barrier layer. The barrier layer hinders the electodeposition of metals into the template therefore should be removed by an additional method. We adapted a technologically long-known method, zincating, to the treatment of AAO templates by replacing the oxide at the pore bottoms by a thin zinc layer. This zinc layer besides making the electrical connection of the metallic base with the solution is also prohibiting the reoxidation of aluminium. Pore-bottom activated aluminium templates are subsequently used for the DC electrodeposition of metallic nanowires. Freestanding arrays of nickel, gold and silver nanowires are used as an illustration of the technique.

Gold nanowire arrays are chosen as SERS substrates due to the plasmonic properties of gold under the desired excitation wavelengths. First the efficiency of the substrates was tested with the probe molecule Rhodamine 6G.The SERS sensitivity was

elucidated by the investigation and optimization of the aspect ratio-enhancement relationship. Following the identification of the ideal fabrication parameters for the highest SERS enhancement, the substrates were evaluated for biological molecule related SERS studies. To show the SERS functionality of the substrates for biological molecules, a bigger protein molecule, bovine serum albumin (BSA), was investigated. The results obtained here were compared to the literature data and the suitability of the templates was justified. The substrates did not caused any conformational changes and the secondary structure of the protein was successfully elucidated and compared to the literature data.

Finally the substrates were used in the evaluation of the adsorption behaviour of a small genetically engineered peptide: gold binding peptide (GBP) under different surface charge conditions for the first time in literature. The results were interpreted both in terms of solution charge and peptide charge effects on the adsorption properties of GBP. The obtained data indicated that at pH 4.5 the peptide was adsorbed to the surface through its negatively charged carboxyl residues and an increase in its beta-sheet conformation was observed suggesting that the peptide placed itself horizontally to the gold surface. Other pH conditions gave also results conform to previous studies.

YÜZEYCE GÜÇLENDİRİLMİŞ RAMAN SPEKTROSKOPİSİ İLE PROTEİN KARAKTERİZASYONU İÇİN AAO ŞABLONLAR İLE ALTLIK ÜRETİMİ

ÖZET

Raman etkisinin keşfedilmesi fizik, kimya ve malzeme biliminde çok önemli ilerlemelere neden olmuştur. Fakat göreceli olarak zayıf bir saçılma olan Raman saçılması keşfedilmesinin üzerinden geçen süre zarfında ilk etkisini yitirmiş ve kızılötesi saçılma sektroskopisi gibi yöntemlere kıyasla çok kullanılmayan bir yöntem haline gelmiştir. Bu durum 1974 yılında "yüzeyce güçlendirilmiş Raman saçılmasının" (SERS) bulunması ile son bulmuş ve bu alana olan ilgi tekrar artmıştır. Yüzeyce güçlendirilmiş Raman saçılması, isminin de belirttiği üzere nano boyutta yapılandırılmış malzemelerinin yüzey özelliklerinin uygun bir ışık kaynağı ile uyarılması sonucu ile oluşan ve yüzeye çok yakın bir bölgede bulunan moleküllerden alınan Raman saçılmasını kuvetlendirici etkiye sahip bir yöntemdir. Bu sayede çok düşük miktarlardaki moleküllerin bile Raman sinyalleri güçlü bir şekilde alınmakta ve moleküllerin tanımlanması yapılabilmektedir. Bu yöntemde gözlemlenen güçlenmenin iki temeli vardır. Bunlardan ilki "elektromanyetik kuvvetlenmedir". Elektromanyetik etki, metal yüzeyine düşen ışığın, yüzey plazmonlarını uyarması ve bu yüzey plazmonlarının toplu şekilde salınım yaparak bir elektrik alan oluşturması ile oluşur. Bu elektrik alan içerisinde bulunan molekülden gelen Raman saçılması ise elektrik alanın etkisiyle kuvvetlenmiş olarak ölçülür. İkinci güçlenme mekanizmasının ise moleküllerin elektronik bulutu ile metal yüzeyinin elektronik alanı arasında bir şarj iletimi oluşması yoluyla meydana geldiği düşünülmektedir. Kimyasal bağlanma kaynaklı bu etkinin toplam kuvvetlenmeye katkısı elektromanyetik etkiye oranla çok daha düşüktür. Görüldüğü üzere SERS yöntemi ile Raman analizi yapılabilmesinin ilk kuralı uygun malzemelerden nano yapılı düzenenli ve kontrollü yüzeylerin hazırlanmasıdır.

Bu tez çalışmasının üç temel hedefi vardır. Bunlar 1) SERS için uygun yüzeylerin (altlıkların) anodik alüminyum oksit içerisine maskeleme yöntemi kullanılarak doğru akım altında elektrokimyasal olarak biriktirilmesi, 2) hazırlanan yüzeylerin SERS etkinliğinin optimize edilmesi (en/boy oranlarının kullanılan uyarıcı ışık kaynağı altında en şiddetli kuvvetlenmeyi vermesi için ayarlanması), SERS kuvvetlenme faktörürünün hesaplanması ve hazırlanan altlıkların biyolojik moleküller için uygunluğunun denenmesi, 3) üretilmiş ve optimize edilmiş olan nanoyapılı yüzeyler üzerinde SERS yöntemi ile "altına özgü olarak bağlanan peptidlerin" (GBP) bağlanma mekanizmalarının yüzey yükü değiştirilerek incelenmesi ve bu sayede farklı yüzey yüklerinde peptid-altın ilişkisinin irdelenmesi.

Şimdiye kadar kullanılan geleneksel SERS altlıkları çoğunlukla çözelti içerisindeki kolloidal nanoparçacıklar, elektrokimyasal yöntemlerle pürüzlülüğü arttırılmış elektrot yüzeyleri ve litografik yöntemlerle üretilmiş yüzeylerden oluşmaktadır. Pürüzlü yüzeylerde kontrolsüz düzensizlikler nedeniyle homojen bir yapı elde

edilememktedir, bu durum da yapılan ölçümlerin tekrarlanabilir olmasını engellemektedir. Kolloidal çözeltilerde topaklanma sorunu mevcuttur ve dolayısıyla da elde edilen sonuçların verimsiz ve tekrar edilemez olması problemleri vardır. Düzensizlik ve kontrolsüz yüzey özellikleri sorunlarını çözen litografik yötemler ise çok pahalı ekipmanlar gerektirmekte olup, zaman alan ve üretilebilen yüzey alanı çok sınırlı olan zahmetli prosedürlerdir.

Bu nedenle nano yapılı yüzeylerin elde edilmesinde uzun zamandır kullanılmakta olan anodik alüminyum oksit (AAO) ile maskeleme yöntemi SERS altlıklarının üretilmesi için ideal bir yöntem olarak karşımıza çıkmaktadır. Zahmetsiz ve hızlı bir şekilde, saf alüminyumun asidik bir elektrolit içerisinde anodik olarak polarizasyonu sonucu düzgün altıgen boşluklara sahip bal peteği dokulu bir oksit yapısı elde edilir. Yapının boşluk çapı, derinliği, boşluklar arası mesafe gibi özellikleri anodizasyon parametrelerine bağlı olup, bu parametreler üzerinden yapılan değişiklikler ile kontrol edilebilmektedir. Bu yapının direk olarak elektrokimyasal malzeme biriktirme yönteminde maske olarak kullanılmasına tek engel ise nano boşlukların tabanında oluşan ve elektrik geçişine engel olan yalıtkan oksit tabakasının varlığıdır. Bu nedenle AAO maskelerin alüminyum altlığından ayrılıp boşlukların kimyasal yöntemlerle tabanlarının açılması gerekmetedir. Bu işlem ise çok kırılgan ve boşluk çapları değişken maskeler elde edilmesine neden olur. Oysa alüminyum teknolojisinde uzun zamandır kullanılmakta olan fakat nano yapılı AAO yüzeylere ilk defa grubumuz tarafından uygulanan çinkolama işlemi ile tabandaki yalıtkan oksit tabakanın yerine çok ince bir çinko kaplaması basit bir şekilde biriktirilmiştir. Bu sayede AAO taban alüminyum metalinden ayrılmadan iletken hale gelmektedir. Bu tezde çinkolama işlemi AAO yüzeyler için ilk defa optimize edilmiş ve AAO'in boşluklarının büyüme mekanizması sıcaklık ve zaman değişkenlerine göre kontrol altına alınmıştır. Daha sonra hazırlanan ve boşluk dipleri iletken hale gelmiş olan AAO maskeler, nikel, altın ve gümüş metallerinin doğru akım altında elektrokimyasal olarak biriktirimesinde kullanılmıştır. Elektrokimyasal biriktirme sonrasında aluminium altlık ve AAO tabakaları çözülerek, kendiliğinden ayakta durabilen, düzgün metal nanotel yüzeyler elde edilmiştir. Nanotel çapları ortalam %70 oranda 100-150 nm arasındadır. Bu yüzeylerin SERS altlığı olarak optimizasyonu, boy/çap oranlarına göre yapılmış ve iki örnek molekül kullanılarak doğrulanmıştır. Boy/çap oranının metalik nanotellerde yüzy plazmonlarının oluşmasında çok önemli bir faktör olduğu bilinmektedir. Yüzeylerin optimizasyonunda kullanılan moleküllerden ilki (Rhodamine 6G) SERS kuvvetlenmesinin hesaplanması için kullanılmış ve yüzeylerin kuvvetlendirme faktörü $5x10^6$ olarak hesaplanmıştır. Ikinci molekül olan "bovine serum albumin" (BSA) ise yüzeylerin protein moleküllerinin incelenmesi için uygunluğunun test edilmesi amacı ile incelenmiştir. Bu çalışmadan alınan sonuçlar, literatürdeki sonuçlar ile karşılaştırıldığında göstermiştir ki, üretilmiş olan altlık malzemeleri ile protein moleküllerinin yüzeye bağlanma ve bu yüzeylerdeki davranışlarını incelemek mümkündür. BSA molekülünün yüzey üzerinde konformasyonunun bozulmadan kaldığı ve SERS spektrumunda tüm önemli bağlarının görüldüğü belirtilmiştir. Bunun yanı sıra üretilen altlıkların yüzey özelliklerinin Raman kuvvetlendirmesini tüm yüzeyde tutarlı bir şekilde yaptığı, yüzeylerin tekrar kullanılabilir olduğu ve farklı ışık kaynakları ile uyarılmanın gerekmesi durumunda anodizasyon parametrelerinde değişiklikler yapılarak uygun ebatlarda üretilebileceği gösterilmiştir. Tüm bu özellikler AAO yöntemi kullanılarak hazırlanan SERS altlıklarının çok hassas ölçümler yapılması gereken biyolojik çalışmalar için ideal

olduğunu kanıtlamıştır. Ayrıca altlıkların kolay üretilebilir, dayanıklı olması ve geleneksel altlık malzemelerinin aksine SERS

SERS yönteminin küçük peptidelerin yüzeye bağlanma özelliklerinin incelenmesi için çok uygun bir yöntem olduğu yapılan literature araştırmaları sonucu anlaşılmıştır. SERS etkisi yüzeyden uzaklaştıkça azalmakta olduğundan peptid spektrumlarında en şiddetli elde edilen pikler, peptidin yüzeye hangi bölgesi ile bağlandığı hakında bilgi verebilmektedir Malzeme-peptid yüzey etkileşimlerinin ne şekilde gerçekleştiğinin anlaşılması çok fonksiyonlu melez nano yapıların üretilmesi açısından önemlidir. Özellikle yüzeylere özgül olarak bağlanma özellikleri olan kombinatoriyal genetik yöntemlerle seçilmiş peptidlerin bağlanma mekanizmalarının anlaşılmasında, SERS sonuçlarının atomik kuvvet mikroskobu, nükleer manyetik rezonans ve kuvars kristal mikro terazi ölçümleri ile elde edilmiş olan sonuçlar ile beraber yorumlanması çok önemli bilgilere ulaşılmasına olanak verir. Özellikle altına özgü olarak bağlanan peptidlerin tanımlanması ve bağlanma özelliklerinin incelenmesini içere bir çok çalşma mevcut olmasına rağmen bağlanma mekanizması halen tam olarak anlaşılmış değildir. Çalışmalar peptidin yüzeyi geleneksel thiol bazlı mekanizmalar üzerinden değil de elektrostatik ve hydrofobik etkileşimler sonucu tanımakta olduğunu ortaya koymaktadır.

Bu çalışmada kullanılan model peptid MHGKTQATSGTIQS amino asit dizisinin üç kere tekrar edilmesi ile oluşan 3rGBP peptididir. Altına bağlanan peptidlerin, dört farklı yüzey yükü altında bağlanma mekanizmaları SERS tekniği kullanılarak literatürde ilk defa incelenmiştir. Yüzey yükü üzerinde yapılan değişilikler bu peptidle ilgili var olan çalışmaların yapıldığı nötral pH olan 7.4 temel alınarak incelenmiştir. 7.4 pH değerinde peptidin toplam yükü + 3'tür. Diğer pH değerlerinde yükler sırasıyla +6 (pH 4.5), izoelektrik nokta (pH 10.28) ve -1 (pH 12) olarak seçilmiştir. Çözelti pH'ında yapılan değişikliklerin metal-çözelti arayüzeyindeki yük dengesini de değiştirmektedir. Bu değişikliğin sonucunda bağlanma mekanizmasında olan değişiklikler daha önce elektrokimyasal kuvars kristal mikroterazi yöntemi ile detaylı olarak grubumuz içerisinde incelenmiştir. SERS ile yapılan bu çalışmada alınan sonuçlar ise daha önce yapılmış olan çalışmaları desteklemektedir. Buna göre GBP'ler elektrostatik çekim kuvvetleri ve hidrofobik etkileşimler sonucunda yüzey yükündeki değişimlere bağlı olarak farklı amino asit bölgeleri ile yüzeyle etkileşime geçmektedir.Ayrıca peptidin yüzeye normal şartlar altında bağlanması beklenmeyen koşullar altında bile konformasyonunu değiştirerek yüzey ile dinamik bir denge oluşturmakta ve neredeyse tüm amino asitlerini kullanarak yüzeye temas etmektedir.

Bu çalışmanın sonucunda SERS yönteminin, uygun altlık malzemeleri kullanılması durumunda, özellikle biyolojik moleküllerin incelenmesi ile ilgili çalışmalarda çok etkin olduğu anlaşılmıştır. Aynı yöntemin altın nanotel yüzeyler yerine diğer teknolojik öneme sahip ve plazmonik özellikler gösteren metaller ile altlıkların üretilmesi durumunda anorganiklere özgül bağlanan diğer peptidlerin de incelenesi kullanılabileceği öngörülmektedir. Üretilen altlıkların büyük yüzey alanına sahip olması, kolay üretilebilir olması, temizleme işlemleri sonrası yapılarının bozulmadan tekrar kullanılabilir olması en önemli özellikleridir.

1. INTRODUCTION

Since its discovery almost nearly a century ago, Raman spectroscopy has always had an up-and-down relationship with scientists from many different fields. Sure it had brought a huge insight to analytical sciences. It was without doubt a rapid, non-destructive, non-invasive technique that could be used on both liquid and solid samples. And most importantly the results could provide fingerprint information about the identity of molecules and their structures. All these features attracted the attention of many physicists and chemists at first but the technique started to stall after the boom of the first years. It turned out that besides its advantages, the method had also some severe limitations. The sensitivity was low compared to IR absorption (which is much more likely to occur compared to Raman scattering process), the strong Rayleigh scattering at the visible excitation range overshadowed Raman data unless a large number of molecules were present in the sampling volume or highly optimized optical detection systems were used and the interpretation of the results was difficult due to the inevitable fluorescence interference accompanying the Raman process.

Fortunately, at 1974 "Surface Enhanced Raman Spectroscopy (SERS)" the more prominent descendant of the Raman spectroscopy have emerged as a new analytical tool. Once completely figured out, SERS revealed to be one of the most sensitive techniques with its detection limits pushing up to 10^{14} times enhancements of the regular Raman signal for single molecule studies (Kneipp et al. 2002). Although that high enhancements were only reported as special cases 10^4 to 10^8 times enhancements are nowadays easily attainable.

The physical roots behind this powerful boost of the Raman scattering was lying on the SERS substrate properties. In fact it was Prof. Van Duyne from Northwestern University who named the technique as "*surface* enhanced" Raman spectroscopy, a term emphasizing precisely that the origin of the enhancement was lying on the substrate itself on which molecules were residing (Jeanmaire & Van Duyne, 1977). As Moskovitz stated SERS is a technique, which is based on a literally "surface"

related phenomenon with its enhancement capability strongly decaying within 5 to 10 nm distance from the surface (Moskovitz, 2005). The amplification of the Raman signal via the substrate is a combined effect arising from the contribution of the electromagnetic field of surface Plasmon resonances reflecting on the molecule's Raman spectrum. Moreover the enhancement may involve sometimes a chemical charge transfer mechanism between the molecule and the substrate. In this dissertation, only plasmonic origins of SERS will be taken into consideration since chemical enhancement is highly molecule specific, much weaker and hard to predict and control. As mentioned the surface (and material) properties plays the most significant role for Raman signal enhancement. Therefore controlling substrate properties both in terms of material choice and structural features is the paramount objective for a successful SERS application. Conventional SERS substrates include electrochemically roughened electrode surfaces, colloidal suspensions of metallic nanoparticles, nanorods and nanowires. The major handicap of all these methods is the lack of reproducibility due to inhomogeneous or uncontrolled substrate natures.

The main focus of this dissertation is to fabricate a robust, homogeneous SERS substrate via electrochemical methods ensuring reproducibility, ease-of-fabrication and versatility.

This thesis is organized as follows.

In the following chapter, (chapter 2) an overview of Raman spectroscopy and SERS will be given. The background and mechanism of SERS will be assessed as an introduction to structure-function relationship of plasmonic materials and to clarify what is expected from a good SERS substrate. This chapter is written in an introductory manner and includes the historical development of Raman spectroscopy to give a better insight and understanding of the subject.

The third chapter will cover the template-assisted fabrication of freestanding metallic nanowire arrays. Production methodologies for anodized aluminium templates, which is the selected template for the production of free standing nanowires, is introduced in this section and the optimization of a novel technique which allows the direct electrodeposition of metallic nanowires on AAO templates will be discussed. As an illustration for metallic nanowire arrays fabricated by this way nickel, gold and silver nanowire arrays will be presented.

In the fourth chapter evaluation of the performance of gold and silver nanowire arrays as SERS substrates will be covered. Special emphasis will be given to gold nanowires since the follow-up of this chapter will focus on SERS enhancement biologically relevant materials, proteins and peptides. As it is very well known gold has a bio-inert and non-toxic nature and has great potential for in-vitro and in-vivo plasmonic sensing and diagnostic applications (Cobley et al, 2011).

The fifth chapter will cover the SERS study of a relatively large protein (BSA) on gold nanowire arrays. The protein will be investigated at two different concentrations and the substrate's compatibility and sensitivity for biological research will be evaluated. The studies are realized to show the usability of the gold nanowire SERS substrates for detection and characterization of biological molecules.

The last chapter will discuss the orientation and adsorption properties of a small genetically engineered peptide: gold binding peptide (GBP) for the first time in literature to our knowledge. The choice of this specific peptide is related to the intrinsic properties of SERS technique. Since the major enhancement in SERS is a near field effect, the biggest contribution to the signal amplification coming from the first few nanometres of the substrate, the adsorption mechanism of GBP can be thoroughly investigated.

Every chapter will comprise an introduction and literature review in itself related to the discussed topics in that chapter, an experimental section, a results and discussion part and will be concluded by pointing out the relevance of the work with the forthcoming sections.

2. LITERATURE REVIEW OF RAMAN SPECTROSCOPY

""I propose this evening to speak to you on a new kind of radiation or light emission from atoms and molecules." With these prophetic words, Professor C. V. Raman of Calcutta University began his lecture to the South Indian Science Association in Bangalore on March 16, 1928." (Raman, 1930).

Eighty-four years later after the discovery of the Raman effect, Raman spectroscopy is today without a doubt one of the most powerful technique in analytical sciences with a wide application spectrum ranging physics, chemistry, biosciences, to nanotechnology and arts and archaeology.

The first published Raman spectra following the discovery of the Raman effect were almost entirely in the physics field studying mainly the vibrational and rotational motion of the molecules. However towards the end of the 1930's the use of Raman spectroscopy became popular for chemical studies as well. The two main advantages of the technique were definitely the possibility to analyse mixtures of non-conductive (inorganic or organic) materials and obtain fingerprint information about the constituents and the interpretation of the intensity of the lines for deducing some quantitative information.

By 1960's the availability of lasers as a more intense light sources and by 1980's the development of computer based data handling technologies made commercial Raman spectrographs available for diverse scientific studies. Nevertheless the first decade's boom on Raman spectroscopy slowed down remarkably once the origin and the limitations of the effect was completely studied and understood. At this point, another equally important discovery as the Raman effect itself was reported by Fleischmann, Hendra and McQuillan in 1974 in their paper on the intensification of the Raman signal of pyridine molecule adsorbed at silver electrodes (Fleischmann et al., 1974).

The discovery led quickly to the naming of the technique as “Surface enhanced Raman spectroscopy (SERS)” and it turned out to be a major innovation for surface science and vibrational spectroscopy communities. After 35 years since this first report, SERS had become a state-of-the art surface science spectroscopic tool. The growing popularity and versatility of the technique is also clearly reflected to the escalating number of publications.

2.1 The Raman Effect

2.1.1 Discovery of the Raman Effect

"A phenomenon whose universal nature has to be recognized.”

C.V. Raman

Sir Chandrasekhara Venkata Raman (1888-1970) was an important figure in Indian scientific life. He was born to a father who was a professor of mathematics and physics and to an educated mother in Madras Province of the British India. He studied physics at the university of Madras and graduated at the age of 16. After graduation he worked as a bank officer in Calcutta but nevertheless kept being a presence in the Indian scientific scene by becoming a member of the Indian Association of Cultivation of Science (IACS). He published the Bulletins and Proceedings of IACS, which became later in 1926 the Indian Journal of Physics.

His scientific career began in 1914 when he was offered a position as professor of Physics at Calcutta University. Up to 1920’s he worked there mostly on acoustics and astronomy and later on optics. However after 1920 he was primarily interested in the scattering of light inspired by the work of Rayleighs.

In 1922, on board of a ship for a voyage to Oxford, Raman was charmed by the deep blue colour of the Mediterranean Sea and carried out a simple experiment on the ship to understand the origins of this blue colour (Singh, 2002). Motivated by the result of this experiment he started a series of experimental and theoretical studies on the scattering of light and finally in 1922 he wrote a paper entitled “Molecular Diffraction of Light” (Raman, 1922). In this monograph he discussed Einstein’s light quantum hypothesis, which was causing avid discussions simultaneously in Europe and he examined how energy could be transferred between light quanta and

molecules and how the quantum nature of the light would show itself through scattering.

Another important publication by Raman in 1922 was about proposing an explanation for the blue colour of the sea (Raman, 1922). In this paper he conflicted Lord Rayleigh's theory on the blue colour of the sea. Rayleigh who discovered in 1899 that the blue colour of the sky was due to the scattering of the light by the molecules in the atmosphere had stated later in 1910 that the colour of the sea was simply the reflection of the blue colour of the sky (Rayleigh,1922).

However in his paper of 1922, Raman discussed that the blue colour of the sea was caused by the diffraction of the light from water molecules. This finding and recent developments on the quantum nature of light, led Raman to study the diffraction phenomenon from molecules and liquids more thoroughly.

Around the same time in the United States, in 1923, Compton had discovered that the inelastic scattering of a photon by a charged particle resulted in a change in its energy. Inspired by this result, Raman (and his student K.R. Ramanathan) also observed that the polarizability of the scattered light depended on the wavelength and linked this polarizability dependence to the presence of a "*feeble fluorescence*" or "*trace of fluorescence*". Both of those terms were directly related to Compton's work. However, a few years later another student of Raman, K.S. Krishnan who continued the scattering studies, observed that the new radiation was partially polarized, thus different than the ordinary fluorescence, which was intrinsically unpolarized (Krishnan and Shankar, 1981).

Later in 1926, he would design the experiment leading to the solid discovery of the Raman effect. The experiment was based on the visual observation of colour and not on the measurements of the light's wavelength as one would expect (Figure 2.1). Raman and Krishnan placed a blue-violet filter in the path of the incident light, and a yellow-green filter between the sample and the observer. They observed that the scattered light coming through the filter had an obvious frequency shift and repeated theses experiments for more than sixty different liquids and gas scattering samples. The results showed clearly that the new radiation was distinctly different from the usual fluorescence because of its feebleness and strong polarization characteristics.

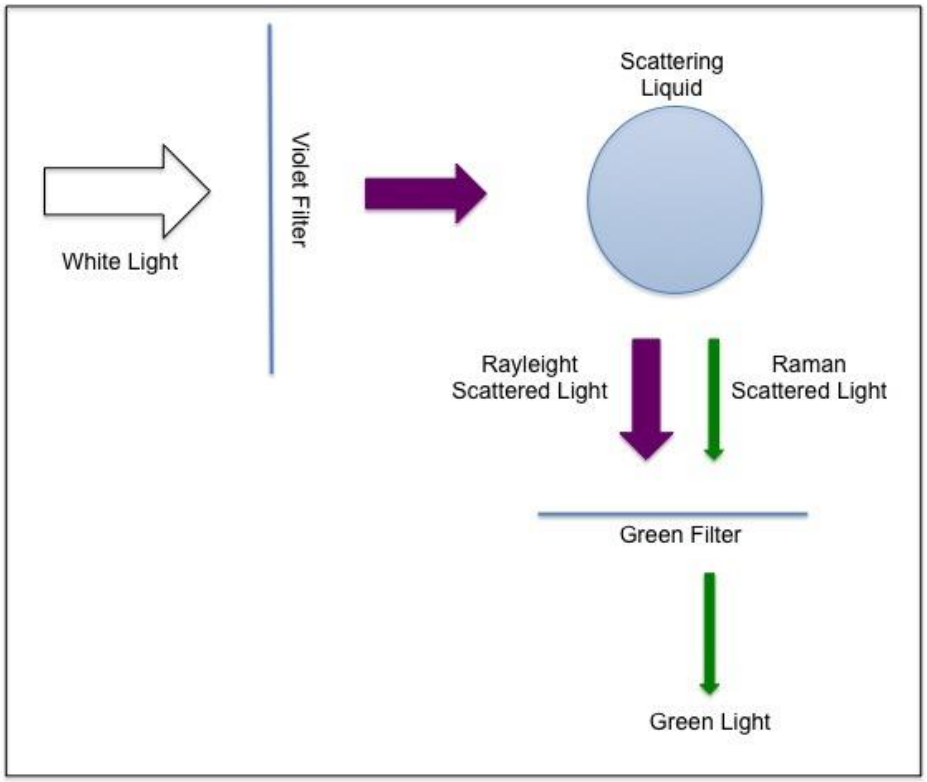

Figure 2.1 : Fundamentals of Raman and Krishnan's Experiment.

They immediately recognized the importance of these results and published their findings in two short letters in Nature, one entitled as "A New Type of Secondary Radiation" and the other entitled "The Optical Analogue of the Compton effect" in 1928 (Raman and Krishnan, 1928).

However those letters did not contain any spectra. Because Raman effect is weak, (only one in a million of photons exhibit the wavelength shift) the intensity of the primary light source was extremely important to be able to record the spectra. This is also why the effect was not noticed earlier since all the scattering studies utilized sunlight as the primary source of excitation. In 1928 Raman used Mercury arc lamps and a quartz spectrograph to photograph the spectrum of the scattered light and measured its wavelength in order to obtain the first quantitative results of the Raman effect (Raman, 1928). The first published Raman spectrums (Figure 2.2) following the discovery were displayed in the Indian Journal of Physics and Raman himself sent the reprints of that article to 2000 scientists to announce his discovery worldwide.

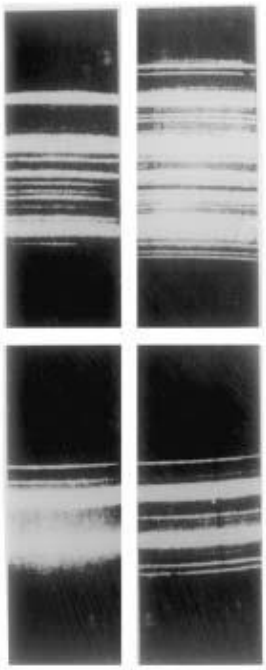

Figure 2.2 : The first Raman spectra (Raman, 1928).

The upper-left photograph is the spectrum of the mercury arc lamp after going through a blue filter. The upper-right photograph is the same spectrum but this time the light has been scattered by liquid benzene. The spectrum is recorded with a small Adam Hilger spectroscope. The lower-left and the lower-right photographs consist of the same spectra but this time a different filter is used instead of the blue one (Singh, 2002).

It should also be mentioned that at the same time with C.V. Raman other scientists around the world also observed the same effect, which by the way was already theoretically predicted by the French scientist Léon Brillouin (1922), and by the Austrian scientist Adolf Smekal (1923). A Soviet physicist, Leonid Isaakovich Mandelstam, discovered together with G. S. Landsberg the inelastic combinatorial scattering of light, which is the basis of the Raman spectroscopy. Mandelstam made this discovery at the Moscow State University just one week earlier than Raman but published his results two months after Raman's Letters to Nature (and to one of which he also made a reference). Because of the work of Mandelstam the effect is named as "combinatorial scattering of light" (due to the combination of frequencies of photons and molecular vibrations) in Russian scientific literature and not "Raman Scattering". Similarly in France, Auguste Rousset noticed a parasite effect while he

was doing his Ph.D. but understood its origins and meaning only after reading the publications of C.V. Raman.

In 1929 Pringsheim stated that the new scattering effect was an entirely new and unique phenomenon and therefore the effect should be named as the "Raman Effect" and the spectrum of new lines as the "Raman spectrum" (Menzies, 1930). Only two years after his discovery Raman received the Nobel Prize in Physics in 1930 ''for his work on the scattering of light and for the discovery of the effect named after him.''

2.1.2 Theory and mathematical explanations

"It seemed indeed that the study of light-scattering might carry one into the deepest problems of physics and chemistry, and it was this belief which led to the subject becoming the main theme of our activities at Calcutta from that time onwards."

C.V. Raman, Nobel Lecture, 1930

It was well established by Raman, Rayleigh and many others that whenever light interacts with matter and it gets either scattered or absorbed and as a result of this interaction detailed information about the structure of the matter could be obtained. The principal and most studied scattering related phenomena are Rayleigh and Raman scattering. To clarify the fundamentals of Raman scattering first the electronic structure of molecules will be discussed in this section. Next, the absorption and scattering phenomena of light will be briefly introduced and afterwards the Raman effect related concepts such as polarizability, selection rules and Raman cross-sections will be explained more thoroughly.

The interaction between monochromatic radiation with an angular frequency ω_1 and molecules is determined by the energy levels of the degrees of freedom of the molecule. Two kind of outcome is possible as the result of this interaction: 1) Movements of electrons (a change in electronic energy levels) and 2) Movements of atoms (vibrational, rotational and translational energy levels). According to Born-Oppenheimer approximation all these different kind of energy levels can be treated independently as shown in equation 2.1. (Larkin, 2011).

$$E = E_{electronic} + E_{rotational} + E_{vibrational} + E_{translational} \quad \textbf{(2.1)}$$

The energy levels of molecules and the various transitions between them are illustrated through a "Jablonski Diagram" presented in Figure 2.3.

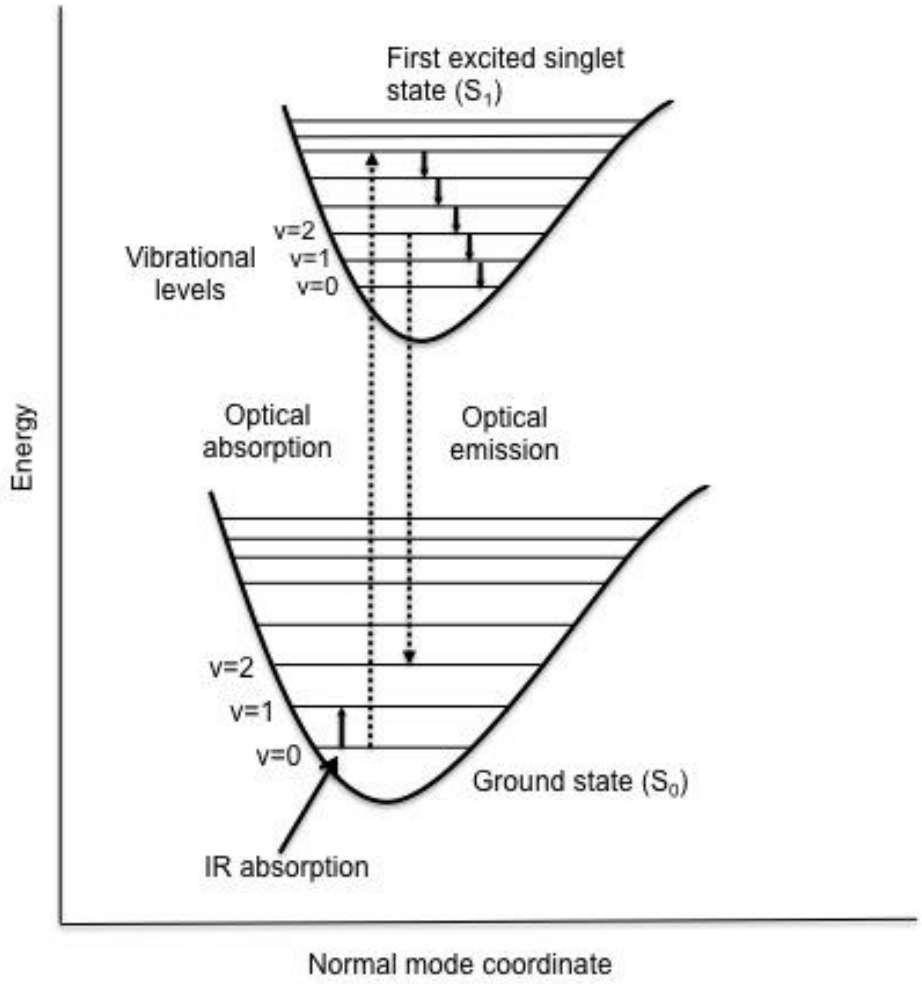

Figure 2.3 : A schematic Jablonski diagram that illustrates both electronic (bold lines) and rotational/vibrational (thin lines) energy levels.

The bold lines in the Jablonski diagram characterize electronic states. The transitions between the ground state, S_0, to an excited state, S_1 (or above such as S_2 or S_3), are arranged vertically and grouped horizontally according to spin multiplicity. The transitions between electronic states are called *electronic transitions*. They are coupled with either absorption or loss of energy. When the energy of the incoming light corresponds to an absorption band of the molecule an electron is excited to a higher energy level. Therefore there is an energy transfer from the photon to the electron. This process is only allowed for some characteristic energy differences between the two levels of the particular molecule. The motional states, represented by the thin lines, include the rotation of a molecule, vibration of its constituent atoms and translations. When the excited molecule relaxes there are several possible

mechanisms such as vibrational relaxation, internal conversion, fluorescence, etc., which can happen. Translational states are irrelevant because they are too close together and hence their spectroscopic investigation is not possible. So, the transitions between motional states are called *internal or vibrational transitions*. These transitions can either be radiative or non radiative.

The molecular motions resulting from characteristic vibrations are described by internal degrees of freedom. For vibrations in a linear molecule the degree of freedom is defined as 3N-5 and for a non-linear molecule as 3N-6. N is the number of atoms in a molecule each one with 3 degrees of freedom in x, y and z directions. Translations constitute 3 of these motions while the other 3 are formed by the rotations. The remaining 3N-6 (for non-linear molecules) are the motions caused by the change of the distance between the atoms or bonds between the angles.

The optical processes involving the emission or absorption of a single photon are;

- Optical absorption where the photon energy is transferred to the molecule and the molecule is either excited to a higher electronic state (the case for *UV/Vis spectroscopy* studies) or its excited to a higher vibrational/rotational level in the same electronic level (the case for *IR spectroscopy*, which probes the vibrational structure of the molecule).

- Emission, which is the opposite of absorption with the relaxation of the molecule from an excited state by emitting a photon.

- Fluorescence is the most common form of the *luminescence* (absorption of a photon followed by its emission). It is a two-step process occurring simultaneously. The emission wavelength is longer than the adsorbed photon's wavelength and hence its energy lower. Since an initial excitation is required for the fluorescence to occur it's a wavelength dependent process and therefore the fluorescence intensity forms the *fluorescence spectrum* of a molecule. This spectrum gives information about the electronic and the vibrational structure of molecules. The energy of the incident beam (E_L) is greater than the energy of relaxation through fluorescence (E_S) and therefore the fluorescence peak of a molecule is seen at a longer wavelength (lower energy) than its absorption peak. This difference of the energy between

absorption and fluorescence maxima is called the *Stokes Shift* (named after Irish physicist George G. Stokes).

- Another important kind of optical process is called *scattering* processes and it involves simultaneous absorption of a photon and emission of another photon. Scattered photons are composed of Rayleigh scattering, approximately 0.1% of all and Raman scattered photons, which constitute roughly 1 in 10^6 or 10^7. There are two types of scattering depending on energy loss: Elastic and inelastic scattering

Elastic scattering happens when the absorbed and scattered photons have the same energy. This is the case of Rayleigh scattering for molecules and Mie scattering for spherical nano-particles.

Inelastic scattering happens when the incident and scattered photons have different energy levels. This energy difference is due to a transition between two states in the molecule and therefore gives information about its internal structure. The most important inelastic scattering type is Raman scattering where a transition between vibrational/rotational energy levels occur.

There are two important differences to be noted between Raman scattering and fluorescence. First, the latter involves an intermediate step between the electronic excitation and the emission within a finite lifetime. Secondly, Raman scattering does not involve a direct absorption of a photon and hence no electronic transitions occurs in the molecule at the incident wavelength. The different types of scattering processes and the fluorescence process are illustrated in Figure 2.4.

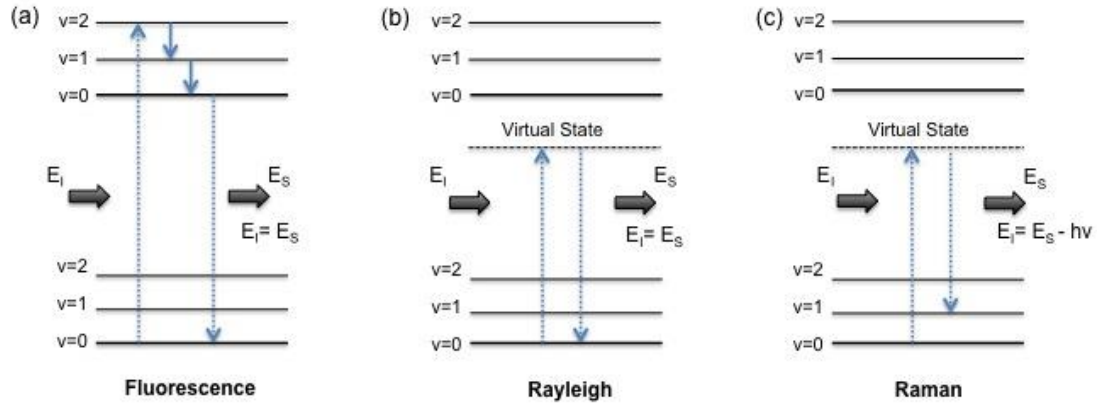

Figure 2.4 : Simplified Jablonski diagrams of Fluorescence process (a) and Rayleigh (b) and Raman (c) scattering.

In quantum mechanical terms the scattering process can be visualized via an intermediate virtual step, namely the "*virtual state*". In quantum mechanics scattering is described as the absorption of the incident photon followed by the simultaneous emission of the scattered photon. This virtual state visualization is helpful since for absorption to occur, the molecule must be excited to a higher energy level yet this level may not exist physically. On the other hand if this virtual state corresponds to a real electronic level in the molecule then the effect is called "resonant scattering" and the scattering process is "*resonant Raman scattering*", which is greater by several orders of magnitude than the regular Raman scattering.

A given Raman spectrum is represented for each Raman band by a wavenumber shift, ν_v from the wavenumber of the excitation radiation, ν as $\Delta\nu = \nu - \nu_v$. By definition $\Delta\nu$ is positive for Stokes Raman scattering and negative for anti-Stokes Raman scattering (Figure 2.5) (Smith and Dent, 2005). Since according to the Boltzman distribution the number of excited molecules is much more smaller than the ones at ground state anti-Stokes band are much more weaker than the Stokes bands.

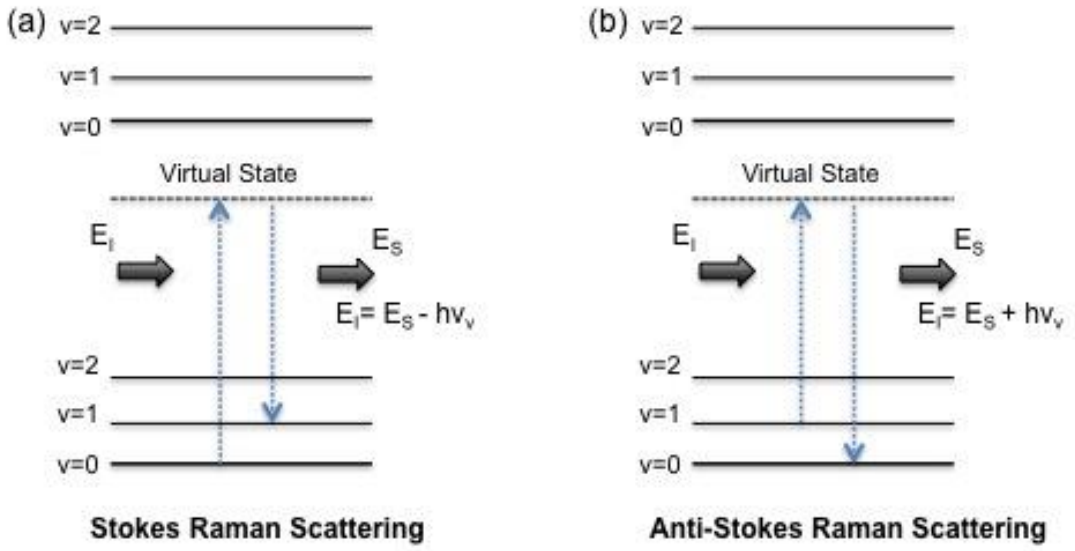

Figure 2.5 : Simplified Jablonski diagrams for Stokes (a) and anti-stokes (b) Raman scattering.

Another important concept that should be introduced when explaining Raman scattering is the notion of "*polarizability*". Scattering can also be described in terms of electromagnetic (EM) radiation produced by the oscillating dipoles induced in the molecule via the EM field of an incident radiation. This induced dipole moment is

formed as a result of molecular polarizability represented by α. The term polarizability describes the deformation extend of the electron cloud about the molecule due to the presence of an external electric field and is represented as μ.

$$\mu = \alpha E \quad \textbf{(2.2)}$$

E is the incident electric field and both E and α varies with time. This variation results in a change in the amplitude of the oscillation of the dipole moment of the molecule. This modified wave has mathematically three components with frequencies ν_0 (Rayleigh), ν_0-ν_M (Stokes) and ν_0+ν_M (anti-Stokes) (Figure 2.6). From this principle it is evident that if an incident wave does not change the polarizability of the molecule, which is the amplitude modulation of the dipole moment oscillation, there would be no Raman signal to be observed.

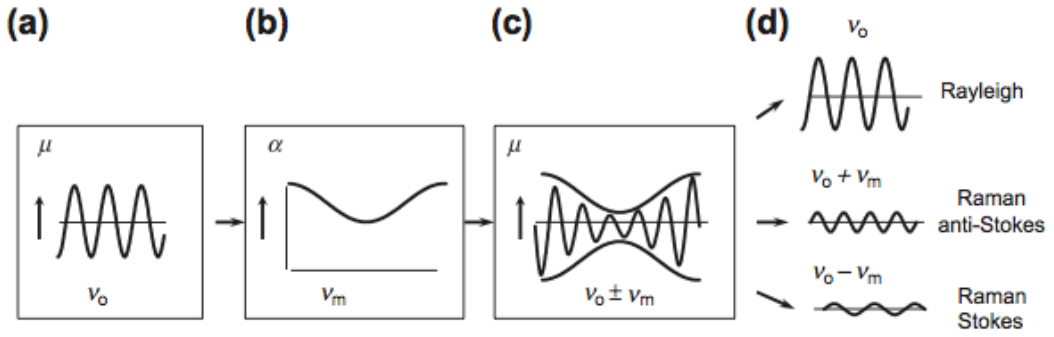

Figure 2.6 : a) Oscillation of the dipole moment of the molecule due to incident radiation, b) Change of polarizability resulting in a change in the amplitude of the dipole moment oscillation seen in c, d) Components of the varied amplitude (Larkin, 2011).

To analyse deeper mathematically how these three different frequency changes may occur we should start by replacing time dependent components of the electric field and polarizability in the equation 2.3 presented below by the induced dipole moment (Dietzek et al., 2010)

$$E = E_0 \cdot \cos(w_0.t) \quad \textbf{(2.3)}$$

When the polarizability expression α= α (Q) is extended in Taylor series around the equilibrium nuclear geometry q_0 we get the equation 2.4:

$$q = q_0 \cdot \cos(w_q.t) \quad \textbf{(2.4)}$$

If 2.3 and 2.4 are replaced in 2.2:

$$\mu(t) = [\ \alpha_0 + (\frac{\partial\alpha}{\partial q})_{q0}.\ q_0\ .\ \cos\ (w_q.t)]\ .\ E_0\ .\ \cos\ (w_0.t)\ ] \qquad \textbf{(2.5)}$$

Using trigonometric formula for the product of two cosine fractions we can rewrite the equation 2.5 as

$$\mu(t) = \alpha_0 E_0 \cos(w_0.t) + \frac{1}{2}(\frac{\partial\alpha}{\partial q})_{q0}\ .\ q_0 E_0 \cos[(w_0 - w_q).t] + \frac{1}{2}(\frac{\partial\alpha}{\partial q})_{q0}\ .\ q_0 E_0 \cos[(w_0 + w_q).t] \qquad \textbf{(2.6)}$$

From equation 2.6 one can easily distinguish the three distinct frequency terms. The first one, w_0t, as elastic Rayleigh scattering having the same frequency as the excitation radiation. The second term, $w_0 - w_q$, is the inelastic Stokes scattering. Its dipole moment is red-shifted compared to the excitation frequency. The last one is the blue-shifted anti-Stokes scattering. Albeit, Stokes and anti-Stokes scattering are identical spectrums the latter has a much more strongly reduced intensity due to Boltzmann distribution (stating that the probability to find molecules in thermally excited states s lower).

As a consequence of the above mathematical explanations, for inelastic scattering to occur the electronic polarizability $(\frac{\partial\alpha}{\partial q})_{q0}$ must be different than zero because otherwise the induced dipole moment will oscillate at the incident radiation's frequency and hence no Raman active vibration will be observed. This condition is called the "*Selection Rules*" for Raman scattering and it constitutes the basis of the differentiation between Raman scattering and Infrared absorption (IR). Selection rules determines which transitions are allowed and which are not. In other words, it is the symmetry of a molecule, which determines if a specific vibration will be Raman or IR active. Generally symmetric or in-phase vibrations and non-polar groups are Raman active. For small molecules with a centre of symmetry no vibration can be both Raman and IR active. For those molecules, vibrations that retain the centre of symmetry are Raman active. In case of no centre of symmetry some vibrations can be both Raman and IR active. However except for di and tri-atomic molecules, calculating which vibrations will be or will not be Raman active is not a straightforward task. For more complex molecules band assignments can be made by the use of *Group Theory* once the symmetry of the molecule is established. However while the classical interpretation of light and matter gives a good explanation for Raman positions and band intensities it has some important shortcomings. For instance the rotational Raman spectra is not explained in classical

theory simply because classical theory does not contain any discrete frequencies for rotational transitions. Moreover without considering quantum mechanical explanation of light, processes such as resonant Raman scattering (RRS) or Surface Enhanced Raman Scattering (SERS) could not be explained (Long, 2002). These concepts will be explained thoroughly further in this dissertation.

2.1.3 Instrumentation

The first Raman experiment was realized using sunlight as the light source and a set of complimentary filters mainly blue and green. However, as seen previously in this chapter, the intensity of scattering is related to the power of the excitation source and to the fourth power of its frequency in addition to the polarizability of the molecule, therefore performing Raman experiments with a weak excitation source was not a reliable option. As a consequence, albeit pioneered in 1928 by C.V. Raman, modern Raman experiments were not possible to realize until the discovery of the lasers in 1960's.

Moreover, the development of charge coupled devices (CCD) another important by Willard S. Boyle and George E. Smith in 1970's replaced the photomultiplier tubes and enabled fast multi channel detection of the received signals. This discovery also brought the Nobel Prize in Physics to its developers in 2009 and made possible the fabrication of modern Raman instruments.

In addition to laser sources and CCD detectors the use of confocal optical microscopes combined with Raman spectrometers in 1990's instead of simple lenses also allowed the collection of Raman signals with a higher efficiency due to larger numerical apertures. And finally with the combination of all those tools Raman spectroscopy became accessible to a larger scientific community in the last 20 years.

Figure 2.7 shows a schematic representation of the main components of a typical Raman microscope. Currently most Raman spectrometers comprise a visible laser excitation source, a set of focusing mirrors, a notch (or edge filter), a set of dispersive spectrograph gratings and a CCD detector (Smith and Dent, 2005).

Confocal Microscopes:

The principle of confocality means to have the same focus as the excitation source. The sample is illuminated through a point source and the image is collected via a

pinhole placed in front of the detector. The illumination source and the pinhole are placed in the same focal plane so that the only light reaching the detector is emitted from the focal plane and neither light coming from above or below the focused point does not contribute to the image. The two main advantages of this confocal setup are:

Limiting the fluorescence: Fluorescence background can easily overwhelm the Raman signal since its strength can be six orders of magnitude higher. The only way to eliminate the fluorescence would be using an excitation wavelength below the fluorescence excitation of the sample. However lowering the excitation sources frequency would also limit the Raman signal. The confocal setup limits the detection of fluorescence compared to the collection of photons from the focal plane, which reduces the fluorescence background drastically.

Allowing the analysis of transparent samples and thin films: An optical cross section of the sample can be made through a confocal setup without cutting the sample. Plus, thin films mounted on other substrates, especially the ones giving strong Raman signals such as glass or silicon can be analysed by staying focused on the film. Otherwise substrates below submicron films would give hundreds times more stronger Raman signals and thin film analysis would have been impossible.

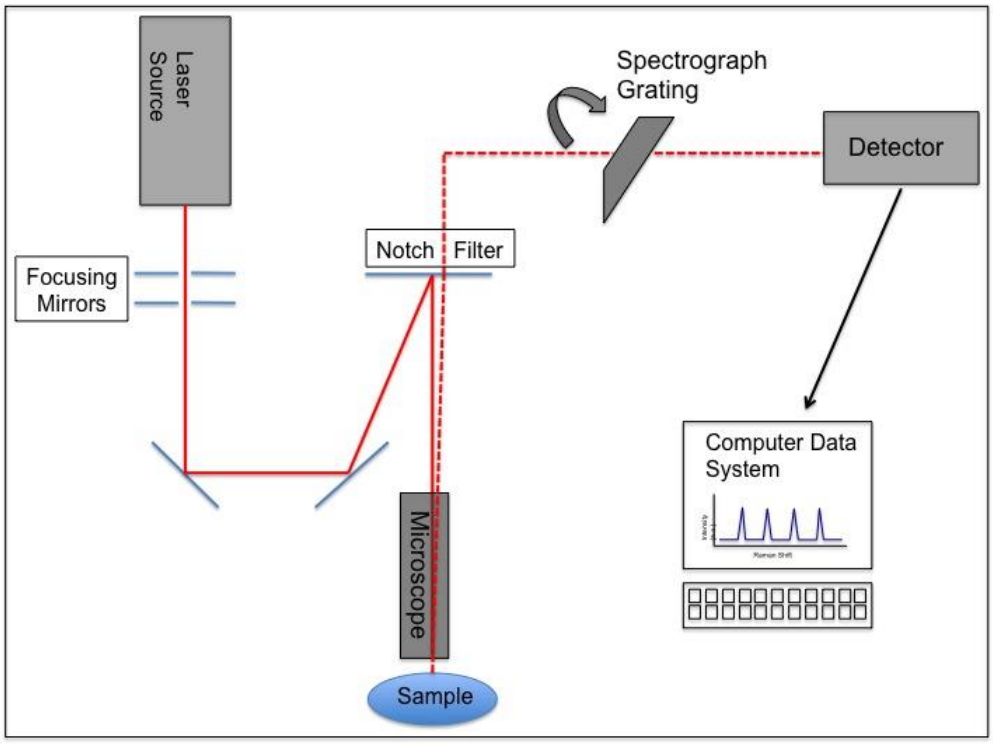

Figure 2.7 : Schematic representation of Raman spectrometer.

Laser sources:

The choice of the laser wavelength affects strongly the outcomes of a Raman spectrum. As we know the scattering intensity changes with the fourth power of the excitation frequency. This means that a spectrum will be 16 times stronger when excited with a 400 nm laser instead of a 800 nm laser beam. However fluorescence background occur more easily at lower wavelengths such as UV or blue region of the spectrum compared to red or NIR region and therefore should also be taken into consideration when choosing a laser wavelength.

Another important factor to be noticed when selecting excitement frequency is the lateral resolution of the spectrum. The lateral resolution changes according to the following formula (equation **2.7)**:

$$\Delta x = 0.61 \text{ x } \frac{\lambda}{NA} \qquad \textbf{(2.7)}$$

Δx is the shortest distance between two points, λ is the excitation wavelength and NA is the numerical aperture of the objective. Hence the available objective choice is also a factor affecting the quality of the spectrum. The limited amount of objectives with a small numerical aperture for UV lasers is an important setback for this wavelength even thought the scattering intensity is quite high. At visible excitation wavelengths fluorescence is still strong with a small aperture but for NIR region there is a wider choice range for suitable objectives giving optimum resolution. For longer wavelengths Raman efficiency drops strongly.

Optical Filters:

The purpose of the optical filters is to selectively stop and filter the laser (Rayleigh) line from the Raman line going towards the spectrometer and than to the detector. The filters are made specifically for each individual laser line. The two main types of filter used most commonly are Notch filters and Edge filters.

In particular Notch filters are used rather frequently. They have a discrete absorption band, chosen at the Raman line. They typically collect the light within 200 cm^{-1} of the excitation frequency. Notch filters have a finite lifetime and has to be changed according to the laser line. Yet, they also have the advantage of being small and very efficient.

The edge filters on the other hand absorbs all wavelengths up to a certain point, and then transmits with high efficiency all wavelengths above this point. They are stable and have almost an infinite lifetime.

Spectrometer:

The scattered light is collected through the filter and transmitted to the spectrometer gratings before going to the detector (Figure 2.8). The gratings are 80% effective meaning that the loss of the collected light at the mirrors of the grating is reduced considerably. They are spectrographic mirrors classed according to their grove density per mm i.e. 1800 gr/mm. For Raman spectroscopy instruments they vary from 300 gr/mm to 3600 gr/mm, the former for lowest resolution and the latter for very specific high-resolution applications.

The spectrometer's focal length, distance of the optical path between the grating and the detector are also important parameters, which should be carefully designed according to special applications, affecting the spectral resolution.

CCD Detectors:

A charge-coupled device or CCD is used to measure and convert to a digital value the movement of an electrical charge. They are composed of an array of Si-photodiodes and are very sensitive to light, thus highly suitable for detecting the weak Raman signal. A big advantage of CCD detectors is to allow multichannel detection meaning that an entire Raman spectrum can be detected at one acquisition step. They are constituted of thousands of individual pixels, each pixel creating a charge when interacting with light. The brighter the light and/or the longer the interaction the stronger is the charge reproduced at the detector. A typical detector size for a spectroscopic detection is 1024 × 127 pixels. They have to be cooled for optimum detection ranges and Peltier or liquid nitrogen cooled models are available for Raman spectroscopes.

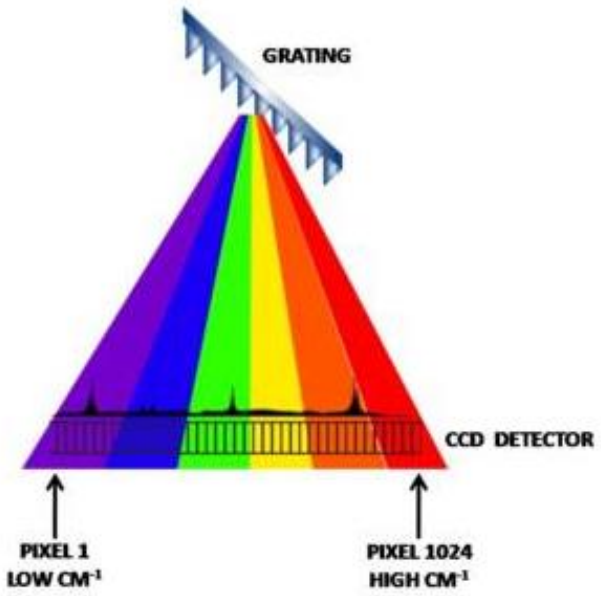

Figure 2.8 : The grating and the CCD detector (url-1).

2.2 Surface Enhanced Raman Spectroscopy (SERS)

2.2.1 Overview of SERS

The notion of Surface Enhanced Raman Spectroscopy (or Scattering depending on whether the technique is used as a spectroscopic tool or for when the physical aspect of scattering process itself is studied) comes from the intensification of the Raman signal through the electromagnetic interaction of light with some specific metallic surfaces. This interaction amplifies the laser's electric field by exciting a phenomenon called "Plasmon resonances". When molecules are in sufficiently close proximity of the metal's surface they will "feel" those Plasmon resonances and their Raman signal also benefits from this effect and gets "enhanced" up to several orders of magnitude.

As mentioned in its name SERS is literally a surface science technique in two very obvious ways. First the effect depends uniquely on the surface properties of metals and second in order to benefit from this effect molecules must be adsorbed to the metallic surface (Moskovitz, 2005).

The discovery of the technique in early 70's brought the huge advantage to overcome the traditional low sensitivity of the Raman spectroscopy. Right from its discovery a massive amount of scientific work, both on the understanding of the effect itself and

on the profits of the technique for sensitive detection of analytes has been undertaken all over the world. Figure 2.9 shows the increase of the research on the subject over the last ten years. Today the applications of SERS range from electrochemistry, biology and materials research to solid-state physics and medicine.

While the first reports on SERS stated modest enhancement factors such as 10^3 later work showed that enhancements up to 10^{11} could be achieved under resonance conditions for dye molecules and more importantly up to 10^{14} without resonance for single molecule works. Those enhancements are extremely strong especially when compared with the feeble Raman cross-sections, ~10–30 cm^2 of the molecules in question. Those cross-sections are several orders of magnitude lower than the fluorescence excitation cross-sections (Hossain and Ozaki, 2009).

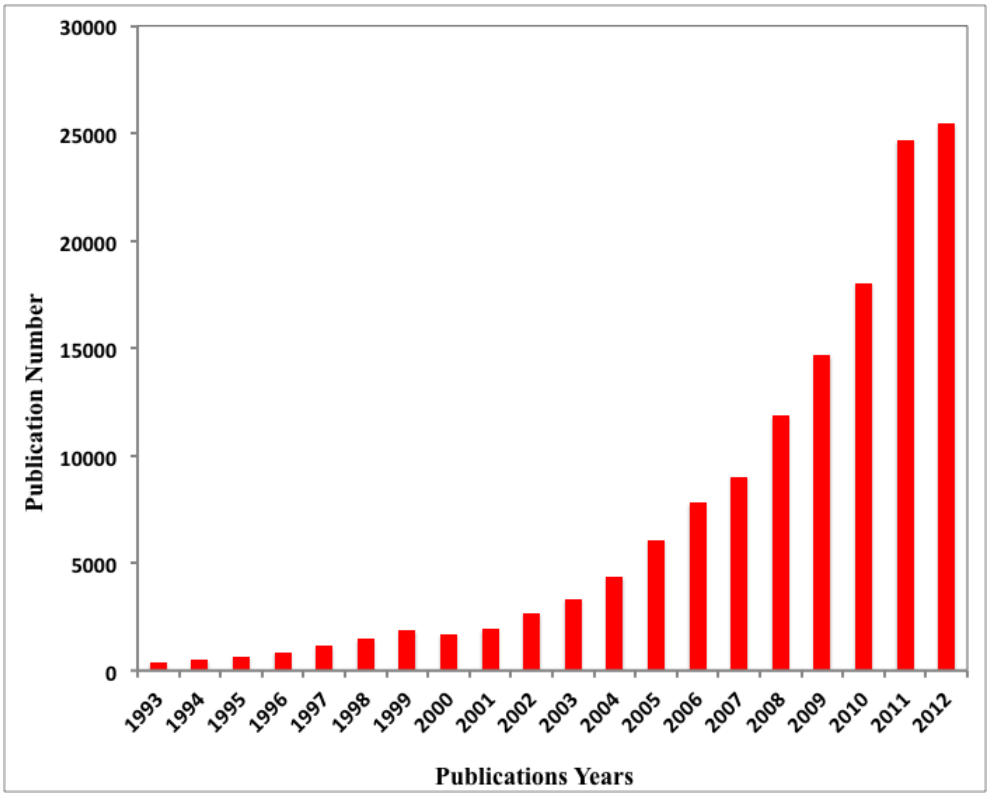

Figure 2.9 : SERS publication trends over the last ten years. Source web of science with SERS and "Surface Enhanced Raman Spectroscopy" in title or topic.

Today, with more than thousands of paper and several excellent reviews and books published, SERS, the effect itself and the application possibilities that it brings up, had opened a brand new field in spectroscopic sciences. Several sub branches of the technique such as "Surface Enhanced Resonance Raman Spectroscopy (SERRS)", "Surface Enhanced Hyper-Raman Spectroscopy (SEHRS)", single-molecule SERS

(SM-SERS), “Tip Enhanced Raman Spectroscopy (TERS)” have been exploited. Indeed Figure 2.10 shows a schematic timeline of the research in this field from the very first observation of the effect and some important work done so far.

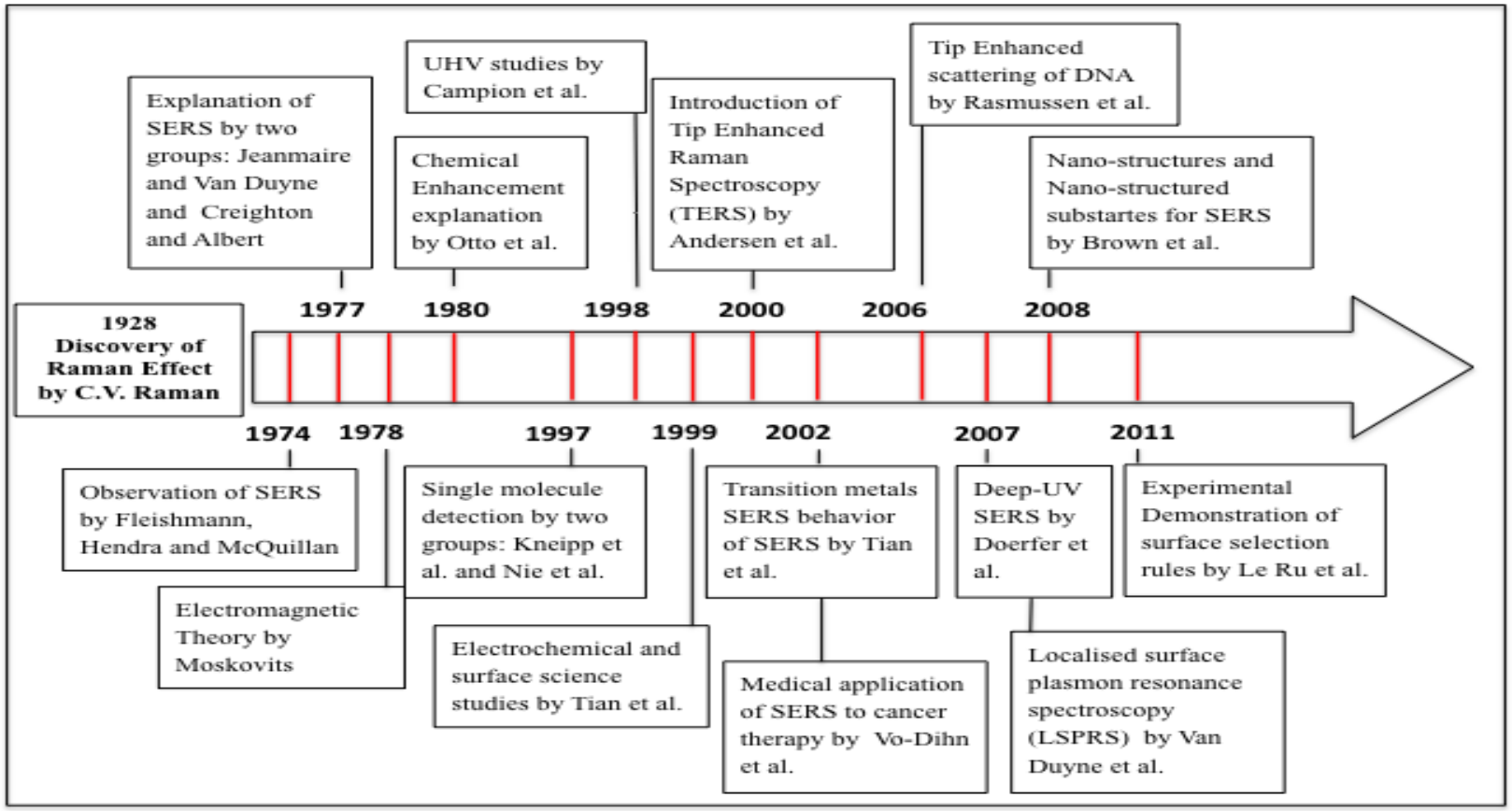

Figure 2.10 : Important steps in the discovery and applications of SERS.

2.2.2 Discovery and a basic description of the SERS effect

Martin Fleishman and co-workers measured the fist surface enhanced Raman spectrum in 1974 at the University of Southampton. This first spectrum belonged to pyridine molecules adsorbed on electrochemically roughened silver electrodes. They performed this experiment while they were working on the development of a chemically specific spectroscopic probe, which could be used to study electrochemical processes in situ. This is why they did not initially recognized the effect as a surface related physical phenomena but assumed the enhancement of the Raman signal was due to the significantly increased surface area of the electrode where a much larger number of molecules was adsorbed.

At first, the Fleischman-Hendra-McQuillan group worked at first on recording the *in situ* Raman spectra on an electrode/electrolyte interface and they did get results for three different systems: Hg/Cl^-, Hg/Br^-, Hg/O^- (Fleischmann et al., 1974). After seeing that it was possible to detect Raman spectra from electrode surfaces they pursued their work with pyridine over silver. They observed Raman count rates of ~500-1000 counts/second from a monolayer of pyridine adsorbed on a roughened silver electrode using 100 mW of 514.5 nm Argon ion laser light. Normal surface Raman intensities expected for a monolayer of adsorbates were typically less than 1 count/second. They interpreted this result as a normal Raman scattering resulting from the increased surface area of the silver electrodes (and thus an increased number of molecules adsorbed to the surface) due to the electrochemical oxidation in Cl^- (or other halide)-containing aqueous solutions. However some key questions remained unanswered in their paper. First of all the reason for such high signals were not clarified thoroughly and no comment was included on the intensities. Secondly they attributed the high Raman signal to the roughness of the electrode and assumed that they were not measuring Raman scattering from a single layer of pyridine molecules on the surface but instead from multiple stacked layers of pyridine molecules (McQuillan, 2009).

After the publication of Fleishmann et al.'s work, Van Duyne from Northwestern University and his graduate student David Jeanmaire repeated the Fleischmann electrochemical roughening procedure and came upon with some new results and conclusions. They suggested that there was either some "*hidden*" resonance Raman

effect, or there was some new type of Raman enhancement mechanism (McQuillan, 2009). Finally they named the new type of Raman enhancement that occurs for molecules adsorbed on a surface as "Surfaced Enhanced Raman" spectroscopy, or SERS (Van Duyne, 1979).

At the same time at 1977, another group, M. G. Albrecht and Professor J. A. Creighton, from the University of Kent, published a short paper with almost identical results to Jeanmaire and Van Duyne's paper (Jeanmaire, 1977).

After its discovery, in early 1980's a lot of work has been done and published in order to understand the nature and origin of the effect.

2.2.3 Definition of SERS enhancement factors

Right after its discovery, the magnitude and origin of SERS enhancement became immediately an intriguing subject for scientists all over the world. As mentioned earlier, the initial interpretation of the enhancement was linked to an increased number of molecules. This postulation revealed quickly to be untrue by subsequent reports that compared the previously obtained results with the signal from pyridine molecules in the absence of the metal. (Albrecht, 1977) (Jeanmaire, 1977). Basically SERS consist of using locally enhanced large electromagnetic fields occurring on metallic surfaces at right conditions to increase Raman signals scattered from molecules adsorbed to these surfaces. Essentially the origin of the enhancement is the excitation of surface plasmons in the metal. In turn this enhanced field results in the magnification of both incident and Raman-scattered fields. This first effect is known as "*electromagnetic enhancement*" (EM) as proposed by Van Duyne and his co-workers in 1977. In addition, an electronic interaction between metal and molecule can interfere with the scattering process producing also an additional increase in the Raman cross-section of molecules. This second effect albeit weaker than the electromagnetic one, since contributing only on the order of an order or two of magnitude is called "*electronic or chemical enhancement*" (Campion, 1998). Albrecht and Creighton proposed this second mechanism at the same time with Van Duyne's paper and they were both right in concept although looking to two different sides of the problem. Figure 2.11 summarizes the two different enhancement mechanisms.

There is however a great ambiguity when one tries to measure, predict and compare enhancement factors. This is mainly why such a big diversity on the value of the EFs (ranging from 10^2 to 10^{14}) exists in the literature. This vagueness on defining the correct EFs comes from several reasons related to both surfaces' structural properties and to adsorbed molecules' intrinsic properties. Nevertheless before defining theoretically and mathematically the EFs, it is extremely important to clarify its meaning, origins and outcomes.

The enhancement factor (EF) is definitely the paramount number for SERS studies and applications. A correct and precise definition of its origins and meticulous calculation of its magnitude is equally important for practical applications (where the EF value may be the sole concern) and for theoretical calculations.

To evaluate the EFs some critical guidelines that must be taken into account in the definition process are;

1. The probe molecules' non-SERS properties such as its Raman cross-section,
2. The distinction between particular experimental conditions and more intrinsic properties of the substrate itself,
3. The separation of average EFs from single-molecule EFs.

Following this guidelines, Le Ru et al. states that EFs can be defined from three different points of view (Le Ru, 2008). First there is the single molecule EF, obtained from a given molecule at a specific point. Second there is the substrate related definition, which will further be explained in detail. Last of all there is the analytical chemistry point of view, which compares the intensity differences between normal Raman spectra and SERS under specific experimental conditions (i.e. concentration of the adsorbate, laser wavelength, etc.).

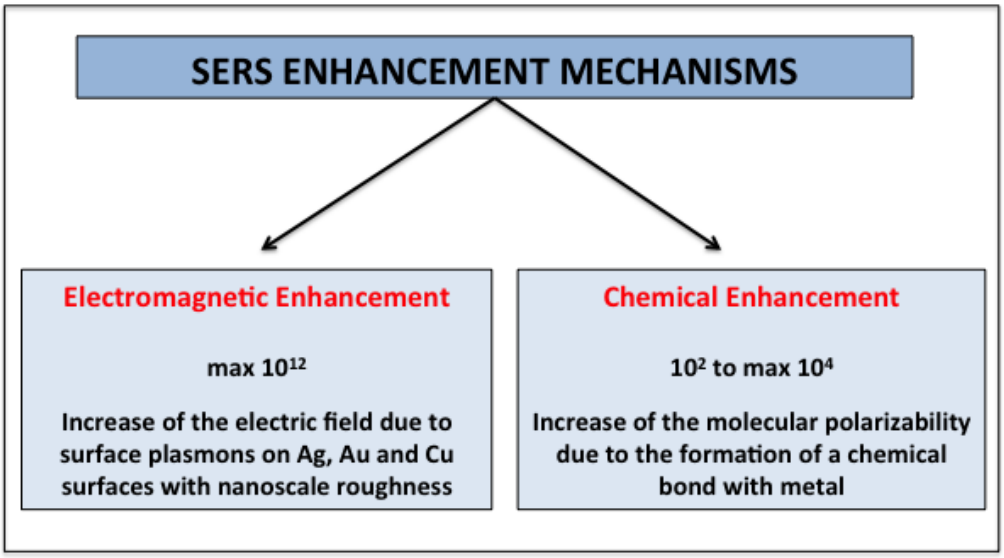

Figure 2.11 : SERS Enhancement Mechanisms related to enhancement type (adapted from Miranda et al., 2012).

It is also equally important to primarily state the factors influencing SERS enhancement together with substrate properties in order to understand correctly the origins of the EFs. SERS process depends on several variables such as:

1. Laser excitation wavelength and polarization,
2. Scattering configuration (90° or 180°),
3. Substrate material choice,
4. Analyte properties, in particular its Raman polarizability,
5. Analyte adsorption properties such as efficiency, concentration, surface coverage, etc.

All SERS enhancements will be defined in this thesis with respect to non-SERS properties of the same molecule in the same environment as the SERS experiment. This is the analytical chemistry point of view of EF calculation. However it is very difficult, if not impossible, to take into account all the variables, as some of them will inevitably remain unknown. So defining an enhancement factor which is independent of as many variables as possible, which can be measured or estimated theoretically and gives a solid proof of the merits of the substrate will be the main concern in this dissertation.

2.2.4 Enhancement Mechanisms

There are two main enhancement mechanisms that define all SERS experiments. The first one, electromagnetic mechanism is based on the nanometre size structure of the substrate and the nature of its reaction once illuminated with an external light source. The second mechanism, altghoutgh more speculative and still discussed among scientists, is based on the interaction of molecules with the substrate.

Electromagnetic enhancement (EM) mechanism:

The electromagnetic enhancement mechanism is overwhelmingly related to the plasmonic origins of the substrate material and to the distance between the substrate and analyte molecule. The mechanism was described by Moskovits for the first time in 1978. The excitation of a metallic particle Plasmon resonance constitutes the theoretical basis and the absolute prerequisite for the observation of SERS. The simplest description of the effect can be visualized by the small metallic sphere model (Dietzek, 2010). In this section first the Plasmon resonance condition will be explained and this will be followed by stating which metals and geometries are suitable for SERS and why.

The enhancement factor at each molecule can be described by the formula 2.8. E(ω) represents the local electric field with frequency and E(ω') is the electric field with Raman shifted frequency ω'. The total enhancement factor experienced by the molecule can be approximated to $|E(\omega')|^4$ (Schatz et al., 2006).

$$E = |E(\omega)|^2 |E(\omega')|^2 \approx |E(\omega)|^4 \qquad \textbf{(2.8)}$$

The field at the surface of a metallic sphere illuminated by a laser is:

$$E_R = E_0 cos\theta + g\left(\frac{a^3}{r^3}\right) E_0 \, cos\theta \qquad \textbf{(2.9)}$$

Where E_R is the total electric field at a distance r from the sphere, θ is the angle relative to the direction of the electric field, a is the sphere's radius and g is the constant related to the dielectric constants of the surrounding media and the metallic particle. For metallic particles with dimensions smaller than the wavelength of the light the extinction and scattering processes are explained by Mie theory and found to be proportional to the g constant with the following relation;

$$g = \frac{\varepsilon(\omega) - \varepsilon_m}{\varepsilon(\omega) + 2\varepsilon_m} \quad \textbf{(2.10)}$$

ε_m is the dielectric constant of the medium which is usually equal to 1 and $\varepsilon(\omega)$ is the dielectric function of the metal as a function of exciting frequency ω. Thus for g to be maximum (and as a result E_R to be highest) the denominator of g should be minimum. This condition is fulfilled when $\varepsilon(\omega) = 2\varepsilon_m$. This specific condition is called the *Plasmon resonance condition*.

Moreover the key properties of electromagnetic enhancement can be deduced from those two equations:

If we substitute equation 2.10 in 2.9 we can see that the electric field is greater when it is perpendicular to the surface than when it is parallel to it. Hence the enhancement is greater for a molecule adsorbed to the surface when polarized perpendicularly.

The electromagnetic enhancement is a near field effect. It is easily seen from the equation **2.9** that the field is inversely proportional to r^3. As a result electromagnetic enhancement will decrease very rapidly with distance from the surface. Thus it can be said that SERS is a truly surface related phenomenon.

The second critical constituent of the electromagnetic enhancement is the metallic material choice since the material's dielectric constant is a key factor in the enhancement formula. Theoretically all metals can support Plasmon resonance conditions. However as mentioned above this condition is dependent on the laser frequency. So only metals showing Plasmon resonances on available laser frequencies will be appropriate as SERS substrates. Electromagnetic enhancement in SERS is observed almost exclusively for Ag, Au and Cu although metals such as palladium, platinum and aluminium are also used. (Dietzek, 2010, Schatz et al., 2006).

Those metals (mainly Au and Ag) have different optical properties than standard dielectrics. The physical origin of these properties lies in the presence of free conduction electrons. The free electrons in a bulk metal are fixed to a positive ion core and form by definition the *plasma* (called sometimes as solid state plasma or free electron plasma) (Schatz et al., 2006). The optical properties of a metal are therefore dictated by the optical response of the free electron plasma and it is defined

by the dielectric function, ε, according to Drude Model. To clarify why only these three metals supports the electromagnetic enhancement their optical response under an electromagnetic field will be examined briefly.

First we assume that the dielectric response is spatially local and frequency dependent. The contribution of the free conduction electrons to optical response is the sum of their individual polarizabilities since they are distributed randomly throughout the metal. When excited under long wavelengths the optical response of the positive ion in the crystal contribute to a constant background real dielectric function $\varepsilon_\infty \geq 1$. Hence the dielectric function of a metal under a specific ω frequency in the Drude model can be written as:

$$\varepsilon(\omega) = \varepsilon_\infty \left(1 - \frac{\omega_p^2}{\omega^2 + i\gamma_0\omega}\right) \qquad \textbf{(2.11)}$$

Where γ_0 is the damping term resulting from the collision of the free electrons with the crystal and impurities and ω_p is the natural oscillation frequency of the free electron plasma charge density or the *plasma frequency*. If the real and imaginary parts of this equation are solved separately the plasma frequency can be obtained from the condition $\mathrm{Re}(\varepsilon(\omega)) \approx 0$. This condition is only fulfilled in the region where $\omega < \omega_p$ (hence for wavelengths longer than the plasma wavelength defined as $\lambda_p = \frac{2\pi c}{\omega_p}$)). It is this condition; $\mathrm{Re}(\varepsilon(\omega)) < 0$ (and Im ($\varepsilon(\omega)$)) which makes Plasmon resonances possible.

On the other hand, in real metals optical processes are likely to contribute to the optical response via intra or inter-band transitions. The Drude model, as represented in the above equation represents the intra band transitions since the excited electrons remain in the same electronic band. When the electrons are optically excited to a higher energy band the Drude model becomes:

$$\varepsilon(\omega) = \varepsilon_b(\omega) - \varepsilon_\infty \left(1 - \frac{\omega_p^2}{\omega^2 + i\gamma_0\omega}\right) \qquad \textbf{(2.12)}$$

$\varepsilon_b(\omega)$ represent the inter-band transitions. Most of the time those transitions occur at energies in the UV range. However for some metals, i.e. gold they are close or below the plasma frequency. In this case they have to be added to the free-electron response as in eq. 2.11. In summary the plasmonic response of metals such as Au and Ag is

frequency dependent and inter-band transitions are a simultaneous part of this response.

A Plasmon is described as a quasi particle representing the elementary excitation or modes of the charge density oscillation in a plasma. A simplified expression is the collective oscillation of free conduction electrons in a metal in the presence of an exciting light source. There are two conditions to be fulfilled for a metal to be considered as suitable for plasmonic applications:

- Re(ε)<0 in the wavelength of interest
- Im(ε) should be small

The optical properties of some metals are seen in Figure 2.12. According to these two rules a great majority of metals are not suitable for plasmonic applications since they do not have any plasmonic properties in the wavelength of interest.

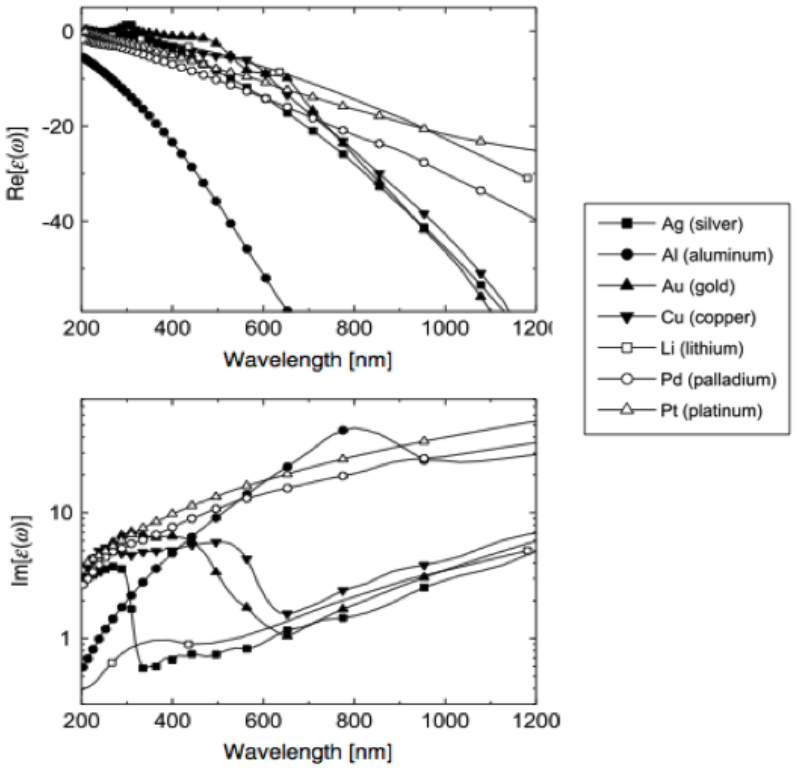

Figure 2.12 : Optical properties of some metals. Real and imaginary parts of the dielectric function are plotted against the wavelength (Dietzek, 2010).

Aluminium is only suitable for plasmonic applications in the UV part of the spectrum. Silver is the most suitable metal for applications below 600 nm and Gold

and Copper are suitable in the near infrared and red zone. This is the main reason why SERS effect can almost only be observed on silver and gold (Dietzek, 2010).

In addition to their intrinsic material properties, optical resonance conditions of small metallic objects are also strongly linked to the geometry. This means that a metallic sphere with smaller dimensions than the wavelength of the illuminating light will present oscillating surface Plasmon multipoles. Those surface plasmons are provoked by the time dependent electric field vector of the light. If the incident light's frequency is resonant with the dipolar Plasmon frequency of the metal then the metal particle will present the light characteristics of dipolar radiation (Moskovits, 2005). When the metallic particle is small enough only dipolar Plasmon resonances are taken into account while others can be ignored. Hence every time that there is a resonant interaction between the optical fields and surface plasmons of the metal, a strong field enhancement is created in the vicinity of the metallic nanoclusters. When averaged over the metallic particle's entire surface the magnitude of the scattered field, E_s, can be written as;

$$E_s = g.E_0 \qquad \textbf{(2.13)}$$

The field enhancement averaged over the particle is represented by g and E_o is the magnitude of the incident field. When a molecule is adsorbed on the metallic nanoclusters surface, or when it is in close proximity of it, the average field strength of the Raman scattered light produced by the molecule is;

$$E_R \ \alpha \ \alpha_R E_s \ \alpha \ \alpha_R g E_0 \qquad \textbf{(2.14)}$$

α_R is the combination of Raman tensors. Since the incident field was enhanced by the Plasmon resonance of the metallic particle the Raman scattered field can also be enhanced by the same manner. As a result the scattered light will have a slightly different wavelength than the incident field. This Raman shifted wavelength will be enhanced by g' so equation 2.13 becomes;

$$E_{SERS} \ \alpha \ gg'\alpha_R E_0 \qquad \textbf{(2.15)}$$

For low wavenumber bands g is almost equal to g'. So the local incident near field enhancement is;

$$|E_L|^4 = |g|^4 \quad \textbf{(2.16)}$$

In summary four important points should be driven from these explanations.

1. Scattering by the metallic particle is the main contribution to the enhancement. The molecule's Raman spectrum is only reflected in the SERS spectrum of the light scattered by the metal.
2. As seen in equation 2.16 SERS intensity varies with the fourth power of the local field however the effect is a linear optical effect depending on the first power on excitation intensity.
3. The polarizability term reflects in fact not only the polarizability of the molecule but the polarizability of the total system composed of the scatterer and the molecule. This constitutes the basis for the so-called chemical or charge transfer enhancement mechanism.
4. As mentioned earlier SERS is a near field effect and the intensity decay very rapidly with increasing distance from the scatterer (Moskovits, 2005).

A final point about the enhancement should be mentioned about the SERS intensity-metallic feature's size relationship. Since the metallic feature's size should be smaller than the wavelength of the exciting light, SERS is one of the few phenomena that can be described truly as nanoscience. The metallic feature's upper and lower dimensional boundaries are determined by the wavelength of the light and by the size of the average molecule respectively. If the features are bigger than the wavelength of the light than in addition to dipolar Plasmon modes multipolar modes will be excited too. These modes are not efficient in Raman excitations (since they are not radiative). On the other hand if the size of the feature is too small then the object should be considered as a quantum object and quantum size effects will dominate the process. To sum up, in order to observe SERS the metallic particle's size should be greater than the mean free path of conduction electrons but smaller than the wavelength of the exciting light (Jain et al., 2007).

Charge transfer (CT) mechanism:

The electromagnetic enhancement mechanism is not the only enhancement contributor to the increase on the Raman signal in SERS. A second mechanism rising from the adsorbate-surface bonding properties was also discovered while performing

electrochemical SERS experiments (Otto, 1984). The observation was based on the change in electrode potential, which resulted in an increase (or decrease) of the enhanced Raman signal. This second mechanism, either called chemical enhancement or "charge-transfer mechanism" may add an additional 10 to 1000-fold increase to the scattering intensity. Despite the small contribution of the chemical enhancement compared to the electromagnetic mechanism it can have a multiplicative effect when combined with the electromagnetic enhancement.

There are also some chemical effects arising from molecule adsorption or orientation that can affect SERS intensity (Le Ru et al., 2007). However they should not be considered as a real SERS enhancement factor because any modification of the Raman polarizability upon adsorption may either result in quenching or enhancement.

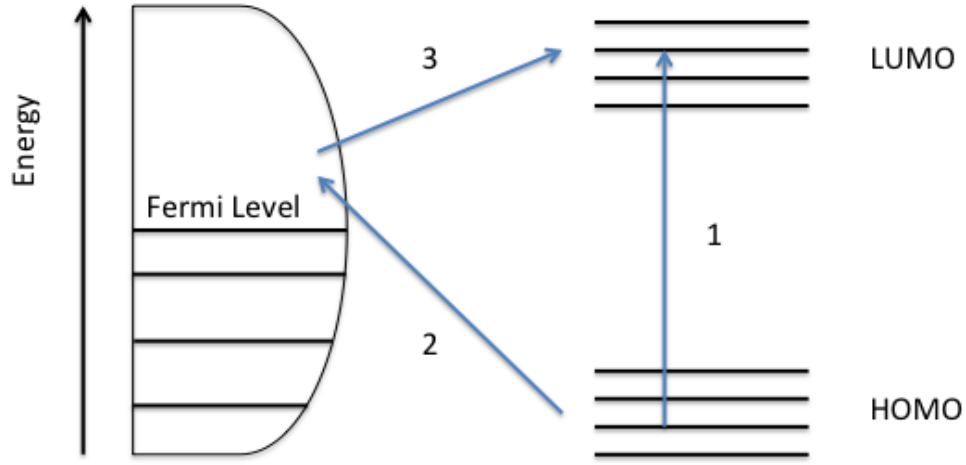

Figure 2.13 : Schematic representation of the three different possible chemical enhancement processes.

There are three kind of different chemical enhancement processes represented in Figure 2.13 likely to occur depending on special circumstances. First an electronic transition in the molecule may happen without any covalent bonding between molecule and metal. The metal simply causes a perturbation on the molecular electronic state and this perturbation result in a change in polarizability. Second, when there is a covalent bond between molecules and metal they form a "surface complex" altering again the total polarizability. The surface complex creates a new electronic state in the molecule, which in turn causes the molecular orbitals to overlap, and modifies the polarizability. And finally the third process may involve a photon-driven charge transfer between the metal and the molecule. This is more

likely to happen when Fermi energy level of the metal and HOMO-LUMO energies of the molecule are matched (Morton and Jensen, 2008).

2.3 SERS Substrates

Obviously the origins of SERS rise from the intrinsic properties of the substrate itself. Since the understanding of this special condition, many different kinds of SERS substrates both in terms of material and production methods have been prepared and rigorously studied. Before reviewing the most important classes of those substrates first what is expected and meant by a good SERS substrate should be clearly defined.

A SERS substrate is by definition supports electromagnetic enhancement conditions in the appropriate excitation wavelengths. Figure 2.14 shows the usage limits of the three main plasmonic SERS substrates.

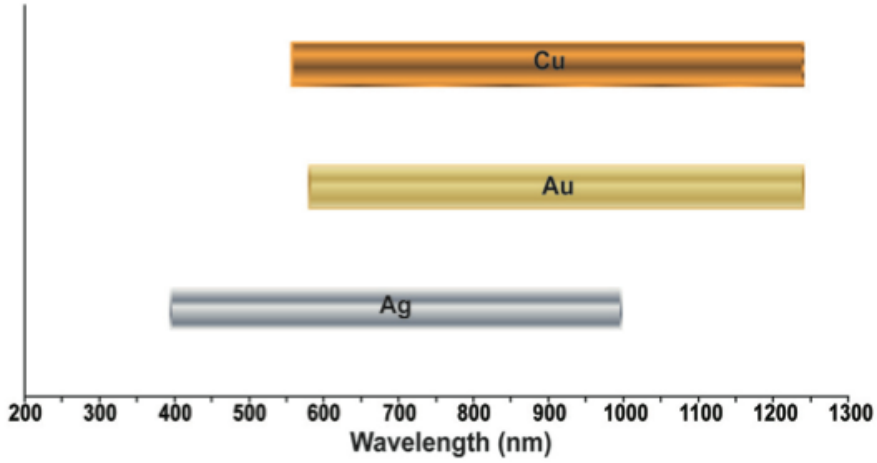

Figure 2.14 : Plasmon resonance wavelength ranges for SERS supporting three principal metals (Van Duyne et.al., 2012).

In addition to that, Natan defines some key points of a good substrate as;

. The substrate must be well defined and characterized in order to be able to calculate and understand enhancement factors. Single particles or even spaced arrays of nanostructures are good candidates for proper enhancement factor estimations. However colloidal particles or aggregates are not fit to this definition properly due to the difficulty of controlling aggregation and inhomogeneous shape and size distributions.

. The reproducibility is another issue to be considered. There are two kinds of reproducibility concerns, namely reproducibility on the various locations of the same substrate and substrate-to-substrate reproducibility.
. The stability of the substrate both on short term and long-term scales is another consideration since stability is crucial for the correct interpretation of scientific and practical
. The substrates are expected to be versatile. The substrate must be usable for various SERS probes (analytes) and still give good and consistent results.
. Finally the cost of production and ease of fabrication must be balanced with optimum results (Natan, 2006).

Another point that should be clarified when talking about SERS substrates is the very much-debated presence of "hot-spots" areas. Hot spots are specific parts of a substrate, which present an unusually higher signal enhancement (Moskovits, 2002). The physical reason behind this phenomenon is the interaction of surface plasmons of two particles separated within a very small but finite distance. The analyte molecule residing in the gap between those two particles will benefit from a large electric field resulting from the opposite charges of both particles. However the "SERS uncertainty principle", which according to Natan can be described as, "the greater the enhancement, the less it is possible to know about the atomic level detail of the substructures involved" brings that it may not be possible to control atomic scale properties of the substrate and the enhancement factor at the same time (Natan, 2006). This concept is thoroughly explained in the concluding remarks of Natan (Natan, 2006). Thus it is very unlikely to prepare deliberately substrates composed of a very large number of hot spots. Although their presence is no longer debated, they are just the random outcome of special situations occurring along the substrates.

Since the discovery of SERS over four decades ago and the clarification of is origins substrates also have had a remarkable evolution. The three main classes of SERS substrates are suspended metallic particles in solution (colloids), planar metallic substrates (arrays of nanostructures) and metallic electrodes (Lin et al., 2009).

Metallic electrodes have played a particular role on the discovery and historical development of SERS and are still used for electrochemical SERS experiments (Ko et al., 2008). They are produced via electrochemical oxidation and reduction steps. They are mostly non-uniform structures therefore the spectra obtained may not be

consistently enhanced over the entire surface area hence the reproducibility of the results is usually poor (Munro et al., 1995). Silver and copper electrodes are prepared more easily this way then Au electrodes (Lin et al. 2009).

Colloids of Au and Ag on the other hand are by far the most predominantly used SERS systems in the literature, especially in the early years of SERS research. However they will also only be briefly reviewed in this dissertation. The emphasis will be mostly made on planar arrays of nanostructures and their main production methods.

Up to now, a vast variety of colloidal substrates have been used for SERS measurements (Freeman et al., 1995, Kenipp et al., 1998) and they have proven to give good Raman signal enhancement results. Among colloidal metallic solutions the two ubiquitously used metallic colloids for SERS are Au and Ag colloids. Generally, they are produced by a chemical reduction reaction where a metal salt is reduced to a metallic nanoparticle in a solution in the presence of a reducing agent. In order to prevent the aggregation and the uncontrolled growth of the particles a stabilizing agent is also used. The most common type of colloidal particle production method is the sodium-citrate reduction method (also called the Lee-Meisel colloids) in which the stabilizing and reducing agent is the same chemical compound. The size and shape of the particles is controlled by many factors such as concentration, temperature and pH and they are strongly related to their performance as SERS substrates. In addition to spherical particles with sizes varying between 1-100 nm, nanoparticles with different shapes such as nanocubes, nano-mushroom arrays (Naya et.al. 2008) or polyhedral particles (Fang et.al., 2011) and particles encapsulated with various coatings such as SiO_2 (Wustholz et.al. 2010) have been successively used.

However the major concern when using colloidal particles is the occurrence of uncontrolled aggregation once the analyte molecule is added. The aggregation of particles causes poor signal enhancement and threatens the reproducibility of the results. Moreover the solutions may become unstable with time that and may give rise to concerns on the reliability of the results. This problem can be solved by assembling colloidal nanoparticles on planar surfaces (Freeman et.al., 1995, Li et.al. 2004). Planar substrates or arrays of nanoparticles, nanowires or nanorods constitute a fairly recent family of SERS substrates compared to colloids and roughened electrode surfaces.

The main production methods for these kinds of substrates are self-assembly, nanolithography, nano imprint and template synthesis methods.

Top down production methods such as nanolithography and nanoimprint technique gives highly ordered arrays of nanostructures. Generally, the methods are performed by using a polymeric photoresist film coated on a substrate such as silicon or glass and patterned as desired with a mold cured with UV light, electron beam or focused ion beam. After forming the pattern, a SERS active metal is deposited on it by vacuum deposition techniques. Despite the advantages of the method to yield in a highly ordered and precisely controlled in terms of shape and size substrate it is still challenging to obtain interparticle spacings smaller than 10 nm. Moreover the focused ion beam and e-beam techniques require expensive laboratory equipment and time consuming experimental procedures.

Self-assembly methods uses a bifunctional molecule to modify solid substrates (Si, glass, Au films, indium tin oxide, etc.) An ordered layer of nanoparticle film is formed through the assembly of particles on solid substrates by chemical or electrostatic interactions. The choice of the bifunctional molecule is very critical for the method since its properties such as size, concentration and surface charge determine the surface coverage and the uniformity of the final substrate. With the usage of appropriate functionalization agents the technique yield to highly efficient, stable and reproducible SERS results (Freeman et.al., 1995). Nevertheless there are two major issue which limits the self-assembly method. First it is quite difficult to obtain by this way a large surface area without any defect and second the interference of functionalization molecules to the Raman signal is inevitable thus making the interpretation of the obtained spectra very complicated.

Another self-assembly technique is the very well known Langmuir-Blodgett (LB) method. This method allows producing a large area film of amphiphilic molecules on solid substrates. Again the molecules have to be functionalized by some chemical agents. The system briefly consist of a through filled with water and the desired molecules are dissolved in a solvent such as chloroform and transferred on top of the water. Two movable barriers then compress them until a uniform monolayer film on the surface is formed. The monolayer is then transferred on the substrate by dipping and/or puling the substrate through the monolayer film formed on the surface. By adjusting the monolayer properties the density of the film can be controlled thus the

interparticle spacing is tuned as desired. The technique has been successively used by many groups mainly Tao et al. to produce various shapes and dimensions of nanoparticle arrays. However just as in chemical self-assembly method the nanoparticles have to be functionalized so the interference of functionalization chemicals to SERS spectra is still unavoidable.

Another alternative to produce highly ordered SERS substrate is to use a template-based method. At this point anodic aluminium oxide (AAO) templates are highly promising and have been used very frequently. AAO templates are produced by the anodic oxidation of aluminium in an acidic electrolyte. The template consists of hexagonal arrays of porous nanostructures. The pore size and interpore distance of the template can be easily controlled and manipulated by adjusting system parameters such as electrolyte concentration, pH, temperature and applied potential. Once the template is obtained it can either be used as it is or it can be detached from the base aluminium metal and serve as a mask for the production of metallic nanoparticle arrays on technically relevant substrates. The use and production methods of the AAO templates will be thoroughly detailed in the following chapters.

One last word should be mentioned about the advantages of choosing among nanoparticles with different shapes, i.e. nanorods or nanowires in plasmonic SERS studies. Nanoparticles with various shapes are certainly the most used SERS substrates since they can be produced both in colloidal solutions and onto planar substrates. If we take into consideration spherical nanoparticles, they have only one local surface Plasmon (LSP) absorption band. Nanorods and nanowires show two LSP bands, one transverse and one longitudinal due to their geometric asymmetry. The transverse mode is seen in the short-wavelength region of the spectrum whereas the longitudinal mode occurs at long-wavelength part. The longitudinal mode shows also a stronger absorption than the transverse mode. Increasing the aspect ratio from rod to wires will result in a red shift and an increase in the intensity of the longitudinal mode (Link et al., 1999).

2.4 Applications of SERS

SERS, with its ability of giving strong chemical and structural information, has been immediately became very popular both in theoretical and practical research areas. Very successful practical applications of SERS have been accomplished in materials

science, life sciences, medicine, forensic science, arts and archaeology and electrochemistry. SERS is today one of the most sensitive techniques available to surface science. In addition to be able to give specific chemical identification by itself SERS can also be coupled with other devices such as AFM and provide myriad application areas by this way. As a result there have been thousands of SERS papers published in the last decade and so it is almost impossible to review all of them. Instead I will only discuss some key examples to emphasize the importance and uniqueness of the technique.

Single Molecule Detection Applications

Since the first reports on single molecule SERS (SM-SERS) by Kneipp in 1995 there has been a growing interest in this field. The importance of SM-SERS lies in its ability to show the upper detection and enhancement factor limits (Otto, 2002).

In SM-SERS studies very low concentration of analyte molecules, usually in picomolar range, are generally used in comparison to colloid concentration. This strategy ensures that in a single scattering volume the concentration of the Raman active molecule below a critical concentration will be limited to nearly a unique molecule. Kneipp in her study in 1995 reported SM-SERS with Rhodamine 6G molecules by following this principle (Kneipp et al., 1995). However it was quickly understood that many factors such as colloid concentration, adsorption efficiency of the analyte to colloid, scattering volume size, etc. were critical and had to be taken into consideration. In 1997, Nie and co-workers confirmed the existence of 10^{14} enhancement factors under resonance conditions with rhodamine 6G molecules and they attributed their findings to some "hot particles" (Nie & Emory, 1997). Following those two studies other groups also focused on SM-SERS however the technique still remains controversial in terms of interpretation of the results and inhomogeneity regarding surface properties (i.e. the presentence of hot spots or resonance conditions of molecules when other excitation source than near infra-red are used) (Le Ru et al., 2006; Vlckova et al., 2008).

Biological and Chemical Sensing Applications

Due to the ultrasensitive detection limits, SERS holds a great promise for the identification of very low concentrations of biological and chemical agents.

Especially for the detection of biological molecules the absence of the water signal from the spectra is a great advantage.

Van Duyne et al. pioneered glucose detection studies on roughened Ag surfaces and they showed the accurate quantification of the molecule in the ranges required by biomedical devices (Shafer-Peltier, 2003). Vo-Dinh and co-workers have used SERS for genomic analysis such as DNA mapping and sequencing applications (Vo-Dinh et al., 1999). In another study the same group used implemented Raman labels instead of traditionally used radioactive markers to identify breast cancer genes (BRCA1) (Allain & Vo-Dinh, 2002).

In another study Tao et al. produced aligned silver nanowire substrates via Langmuir-Blodgett technique and they used the substrate for the detection of a chemical (2,4-dinitrotoluene) commonly used in landmines (Tao et al., 2003).

Kneipp group showed that by using common Raman labels such as Crystal Blue and Rose Bengal on gold nanoparticles the molecular environment of living cells can be imaged (Kneipp et al., 2002). The images constructed upon the SERS signal of C-H deformation/bending modes were successful to probe the cellular structure in its nano-environements.

The versatility of SERS technique is highly promising for many biological and biomedical applications to be developed in future.

Surface Science Applications

Since SERS has been used very extensively in surface science a brief review of this field is very challenging. The main research areas involve oxide film formation, catalytic activities and electrochemical studies.

Chan et al studied oxide film formation on copper in aqueous environments at different pH values. Potential dependent metal-oxide lattice vibrations have been detected at specific wavenumbers accurately. The results of the study have showed that the technique results in a monolayer sensitive in situ vibrational probe. The same group worked also on the high-pressure oxidation of Ruthenium (Chan et. al. 1997). Luo et al., worked on the effect of water vapour on the temperature-dependent surface oxidation of Pt-group metals in ambient pressure gaseous oxygen environments (Luo et al., 2000).

Since SERS overcomes the limited detection frontiers and long integration times of the conventional Raman spectroscopy it can be expected that many more application areas can be exploited in the future. It should not be forgotten that the applications reported herein are only a small part of the several studies realized since the discovery of SERS.

3. TEMPLATE ASSISTED FABRICATION OF NANOSTRUCTURES

3.1 Introduction

Template synthesis methods are used to prepare micro and nanomaterials based on a previously designed structure and dimension. This strategy reveals to be extremely important in nanosciences where the morphology and material of the nanostructures governs their functionality and therefore should be carefully tailored. Template based synthesis of nanowires is a versatile method suitable for producing various kinds of metallic nanowires with a wide range of structural features. Frequently used template materials for nanowire array fabrication are anodic aluminium oxide, mesoporous silica and track-etched polymeric membranes (Sulka, 2008; Cao & Liu, 2008). In recent years many research groups focused on the production of regularly arranged template materials via diverse methods.

Among these methods, lithography techniques (soft lithography, nanoimprint lithography, scanning probe lithography, electron beam lithography etc.) are vastly used in the production of various nanoparticles, nanowires and nanotubes and the preparation of nanoporous templates used for the subsequent deposition of metals (Xia et al., 1999, Sulka, 2008). Those techniques involve mainly the transfer of a pre-formed pattern from a mask (or stamp) to a resist and then to the surface with ultra high precision and resolution. However this technique has also some important drawbacks. Conventional lithography techniques yield to limited periodicity and aspect ratio, on the other hand more advanced derivations of the techniques can increase the resolution to nanometre scale but they require sophisticated and expensive equipment.

Therefore, in order to overcome such drawbacks a great demand on low-cost, high-throughput fabrication methods have emerged in recent years. Among them, pattern formation by anodic oxidation of aluminium stands still today as an elegant and

straightforward approach. The advantages of AAO are its high surface area, its tunable pore size and pore length, its adjustable characteristic pore arrangement framework and the simple synthesis procedures. Altering the structural parameters of AAO gives control over the morphology of the nanowires and allows tuning their dimensions according to functional requirements.

Anodization or electrochemical oxidation of aluminium dates back to the beginning of 20th century. While earlier purposes of the process was to obtain protective or decorative films, after 1930's applications evolved towards scientific research. It was in 1953, after the invention of electron microscopy, that the structure of hexagonally close packed porous anodic aluminium oxide (AAO) was detailed by Keller and co workers (Keller et al., 1953). In 1968, Diggle et al. predicted the first theoretical models about the structure of the oxide film. Later in 1970, Wood and O'Sullivan presented a new model for self-ordered pore growth, anion incorporation and water content of the porous AAO by using a new technique: transmission electron microscopy (O'Sullivan and Wood, 1970). However the first report on ordered porous AAO would be presented much later in 1995, by Masuda and Fukuda and their work will be the boosting impact on the implication of AAO in nanosicences and nanotechnology.

The two-step replicating anodizing process pioneered by Masuda and Fukuda results in self-ordered porous alumina membranes with precise interpore distances, very narrow size distribution and high aspect ratios (Masuda and Fukuda, 1995). This huge reduction of dimension and meticulous control of the surface geometry has opened countless application areas for AAO films in catalytic, electronic, magnetic, optoelectronic, nanophotonic and sensing research fields (Sulka, 2008).

From now on this chapter is organized as follow: First a brief introduction on aluminium oxide properties will be given and later challenges and techniques on using aluminium oxide as a template material will be presented. This will be followed by experimental details on the implementation and optimization of a previously known method (zincating) to AAO templates and benefits and novelties of this technique for the electrochemical production of metallic nanowires within AAO templates.

3.1.1 Properties of anodic oxide films

Types of anodic oxide films:

There are two types of anodic oxide films, fabricated through electrochemical oxidation of aluminium in an electrolyte solution: barrier type films and porous type films. Although the transition from barrier type film to a porous type structure occurs easily and is influenced by many factors other than the electrolyte type, e.g. anodizing time, it is generally accepted that the type of the anodic film obtained depends mainly on the electrolyte choice. (Sulka, 2008).

If the oxide layer formed on the surface is insoluble in the chosen electrolyte a *barrier-type* film is obtained. Examples of those electrolytes are neutral electrolytes (pH 5-7) such as boric acid, ammonium borate, ammonium tartrate, aqueous phosphate solutions, tetraborate in ethylene glycol, perchloric acid with ethanol, organic electrolytes such as citric, malic, succinic, and glycolic acids (Sulka, 2008).

On the other hand porous type films are obtained in strongly acidic electrolytes such as sulphuric, phosphoric, chromic and oxalic acid where the oxide film is slightly soluble. AAO films can also be obtained in various other electrolytes like mixed solutions of acids, etc.

The oxide film structure in both cases is composed of an inner oxide layer found at the metal/oxide interface and an outer oxide layer at oxide/electrolyte interface (Figure 3.1). The inner layer is formed of high purity alumina (Al_2O_3). The outer layer has incorporated anions such as phosphates or sulphates, coming from the electrolyte solution in its structure. Porous type films have a higher amount of incorporated anions than barrier type films. The ratio of inner oxide to outer oxide layer is determined by the electrolyte type for disordered pore growth conditions but it is constant under self-ordering pore growth (i.e. 0.2) (Choi, 2003).

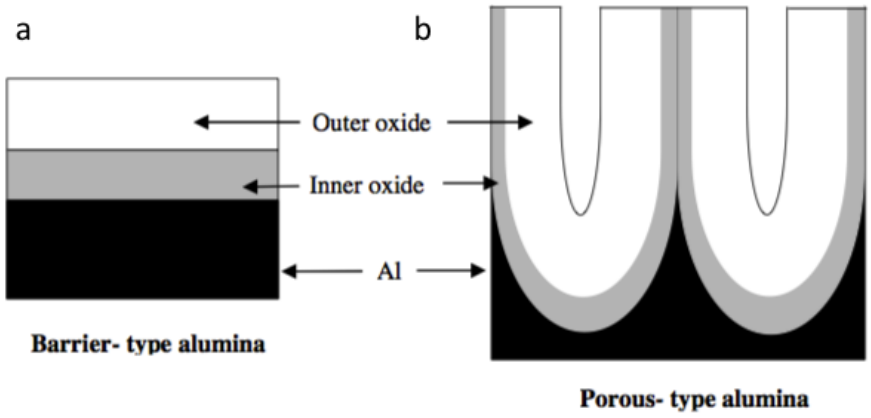

Figure 3.1 : Schematic diagram showing (a) barrier-type film and (b) porous-type film on aluminum with inner and outer oxide sections (Choi, 2003).

The barrier type film has the same structure as the naturally occurring oxide layer on aluminium surfaces. It is an insulating layer and can only allow the passage of the current from its structural faults. The thickness of the barrier layer depend only on the anodizing potential by 1.3 – 1.4 nm/V. On the other hand the thickness of the porous type film is potential (by 1.15 nm/V), time and temperature dependent. Hence, while the thickness of the barrier type films are limited by ionic diffusion, much thicker porous type films can be obtained by increasing anodizing time. On the other hand, since the growth of all porous films also start as barrier type via dissolution of the oxide layer in acidic electrolytes, there is always a thin but compact barrier layer remaining present on the bottom of the pores. This barrier layer's thickness found on the bottom of the pores is solely potential dependent (Sulka, 2008).

Morphology of porous AAO films:

Porous AAO's are characterized by an array of close-packed hexagonal columnar cells. The pores, situated at the centre of each hexagonal cell are almost cylindrical and separated from the base aluminium metal by a thin aluminium oxide barrier layer.

Keller et al. described the formation of hexagonal close packed structure of anodized aluminium oxide in 1953. According to his study, the pores begin to form from the barrier type oxide structure. They generate from a point on the surface under the solvent action of the electrolyte. At this point where the underlying metal is almost exposed to the solution, the current flows to form a new oxide causing a local raise in

temperature. This temperature raise in turn increases the local dissolution of the oxide and a single oxide cell is thus formed. The shape of the cell is cylindrical towards the upfront due to the spherical shape of voltage and current fields and hemispherical towards the bottom because of the finite size of the pores. The process repeats its self at several points along the oxide structure until each oxide cell has six neighbouring cells. At the intersection of every three cells a concave metallic triangular pillar remains. Those pillars are also anodically oxidized and finally a continuous porous oxide layer is formed on the surface giving the hexagonal shape of the structure (Keller et al., 1953).

During the change of the oxide cells from cylindrical to hexagonal form, pore shapes also changes due to current flow and localised heating along the remaining metallic pillars. Since localised metal consumption, current flow and heating are not equally distributed along the pore perimeter; the pore will have six projections directed towards the corners of the hexagons. However it was later confirmed that the central pores were not star shaped as proposed by Keller but mostly cylindrical with a size proportional to the applied potential. The transformation from cylindrical oxide cell shape to hexagonal array of close-packed oxide cells with a central pore is represented in Figure 3.2 (Jessensky et al., 1998).

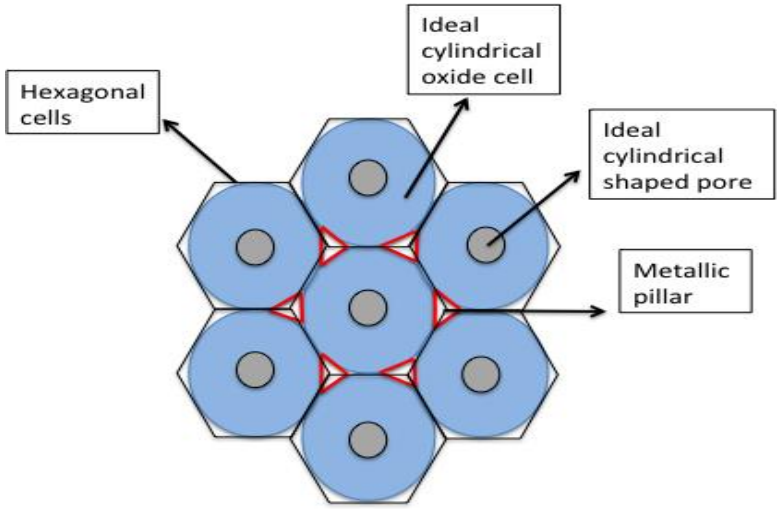

Figure 3.2 : The schematic representation of the transformation of ideal cylindrical cells to hexagonal close packed array (adapted from Keller et al, 1953).

The general structure of porous AAO is shown in Figure 3.3. Almost all of the parameters defining the AAO are directly dependent of the potential. The pore

diameter is linearly proportional to the anodizing potential with a proportionality constant of approximately 1.29 nm/V.

$$D_p = \lambda_p .U \qquad \textbf{(3.1)}$$

D_p is the pore diameter; λ_p the proportionality constant and U is the potential. This potential dependence of the pore diameter is independent of the electrolyte choice.

The interpore distance (D_c) is also linearly proportional to the anodizing potential by a factor of 2.5nm/V.

$$D_c = \lambda_c .U \qquad \textbf{(3.2)}$$

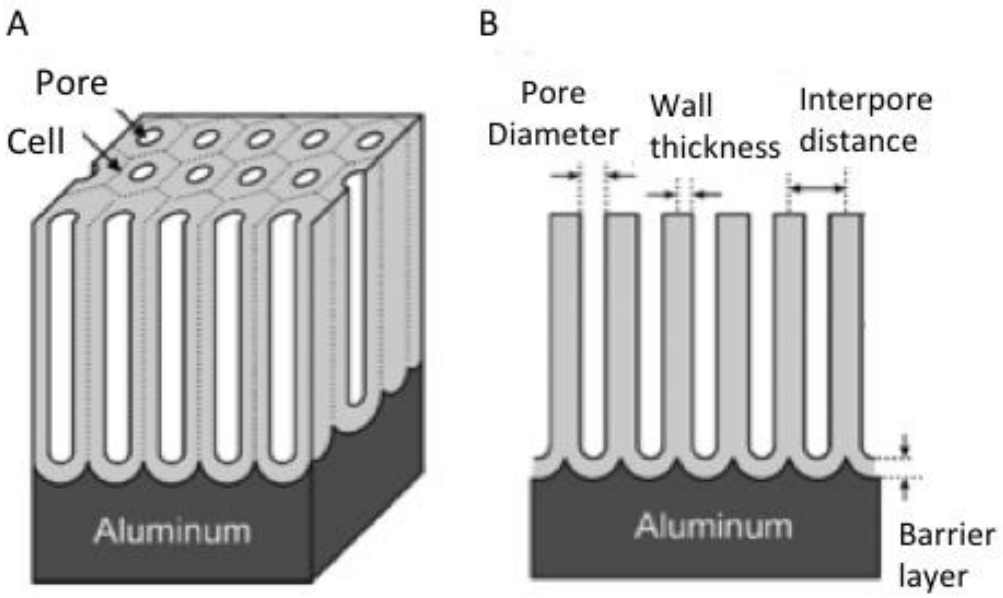

Figure 3.3 : A) Structure of AAO and B)Cross-sectional view of the structure (after Sulka, 2008).

The wall and the barrier layer thicknesses are interrelated and show slight variations according to electrolyte choice and applied potential. For oxalic acid electrolyte it was found that the proportionality constant could go up to 0.89 (Sulka, 2008).

The barrier layer thickness is determined by directly on the potential by 1.15 nm/V for porous AAO films.

Electrochemistry of AAO film formation:

When aluminium metal is made the anode of an electrochemical cell comprising a cathode (i.e. Pt or stainless steel) in an acidic electrolyte, an oxide film grows at its surface once an external potential is applied. The current density behaviour of porous alumina formation under potentiostatic conditions is represented in Figure 3.4.

At the initial stage of anodization when the potential is applied the current density decreases rapidly (Figure 3.4 regime 1). This is the stage where a barrier type oxide forms on aluminium surface. This uniform film grows due to high field ionic conduction under constant field strength. Although barrier layer smoothens the aluminium surface, remaining defects and/or impurities causes some local variations in the field strength (Figure 3.4 regime 2).

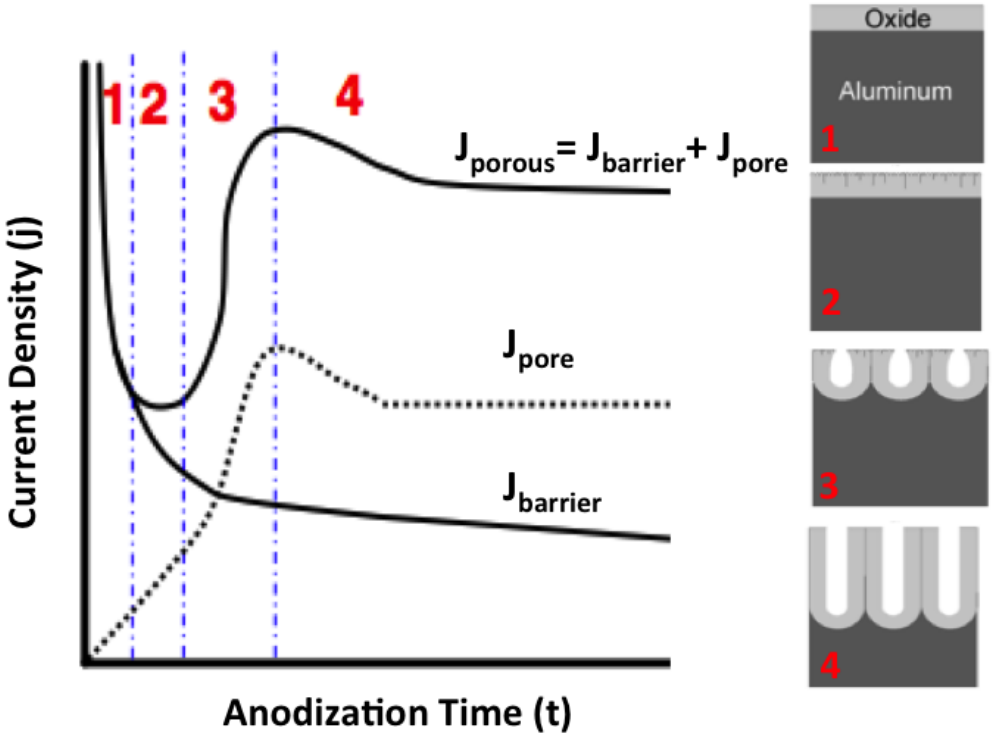

Figure 3.4 : Current density-anodization time behavior transients of porous layer and barrier layer formations and their schematic representations (adapted after Choi, 2003).

This fluctuations in current distribution lead to the enhanced field assisted (and/or enhanced temperature assisted) dissolution of the oxide and consequently to the formation of porous type oxide layer (Figure 3.4, regime 3). The oxide keeps growing preferentially above the flaw sites while barrier layer keeps thickening. This continues to the point where the current is concentrated in the thinner film region, which will become the bottom of the future pore. Finally a steady-state growth of

porous alumina with no change in current density is achieved (Figure 3.4 regime 4). The slight decrease in current at the beginning of stage 4 is due to the competition among the pores as some pores stop growing in order to keep the field strength constant across the barrier layer. During the steady-state growth there is a dynamic equilibrium on the oxide formation at the electrolyte/oxide and dissolution at the oxide/metal interfaces. The pore forming current (j_{porous}) can be considered as the sum of barrier layer forming current (j_b) and the hypothetical pore forming current (j_p). The steady state stage current density can also decrease very slowly along time due to the diffusion limits in the pore channels as they become longer.,

Steady-State growth of porous alumina:

Patermarakis et al. described a kinetic model of AAO growth based on field-assisted dissolution of oxide. Although many other groups speculated alternative approaches such as chemical dissolution due to the increased temperature at the bottom of the pores the model described by Patermarakis remains still as the most probable one and will be discussed here briefly.

There are four main processes involved in the alumina formation in an acidic electrolyte. Those are 1) formation of Al_2O_3, 2) dissolution of Al_2O_3 at the oxide electrolyte interface, 3) diffusion of Al^{3+} cations across the barrier layer and 4) evolution of H_2 (g) at the cathode. Plus, some side reactions occur at the same time such as oxygen evolution at the anode. Yet explaining the process is much more complicated than those four processes and albeit the vast amount of work dedicated to the subject some aspects remains still not fully elucidated. For instance it is not clear which oxygen carrying anion species (of O^{2-} and OH^-) are involved in the anodic reactions. There are several ways from where O^{2-} and OH^- species can generate. OH^- ions are produced by cathodic reduction of water or by water splitting in the electrolyte. On the other hand O^{2-} ions are either formed by oxygen vacancy replacement from adsorbed OH^- ions at electrolyte/oxide interface, water splitting at the interface or by interaction with incorporated anions coming from the electrolyte.

Aluminium oxide film growth as result of anodic polarization of aluminium in an acidic electrolyte can manifest itself according to the overall equation.

$$2Al^{3+} + 3H_2O \rightarrow Al_2O_3 + 6H^+ + 6é \qquad \textbf{(3.3)}$$

At the electrolyte/oxide interface the film growth occurs following:

$$2Al + 6OH^- \rightarrow Al_2O_3 + 3H_2O + 3é \quad \textbf{(3.4)}$$

At the metal/oxide interface the film growth occurs following:

$$2Al + 3O^{2-} \rightarrow Al_2O_3 + 6é \quad \textbf{(3.5)}$$

Yet the main anodic reaction is:

$$Al \rightarrow Al^{3+} + 3é \quad \textbf{(3.6)}$$

The side reactions that causes the evolution of oxygen at the metal/oxide interface can be written as:

$$2H_2O \rightarrow O_2 + 4H^+ + 4é \quad \textbf{(3.7)}$$

$$4OH^- \rightarrow 2H_2O + O_2 + 4é \quad \textbf{(3.8)}$$

$$2O^{2-} \rightarrow O_2 + 4é \quad \textbf{(3.9)}$$

Moreover oxygen bubbles evolution on the anode may be seen and according to Zhu et al., it is an indication to the passage of the film from barrier type to porous type (Zhu et al., 2005).

The field assisted dissolution of anodic aluminium oxide starts by the polarization of Al-O bonds causing ejection of Al^{3+} ions from the oxide. The thermal assistance to the process comes from the Joule heating (or ohmic heating) effect. The growth of the oxide is the result of the thermally assisted, field enhanced dissolution of oxide at the base of pores and new oxide growth occurs at the oxide/metal interface. The oxide growth involves the inner and outer migration of many ionic species through and across the barrier layer.

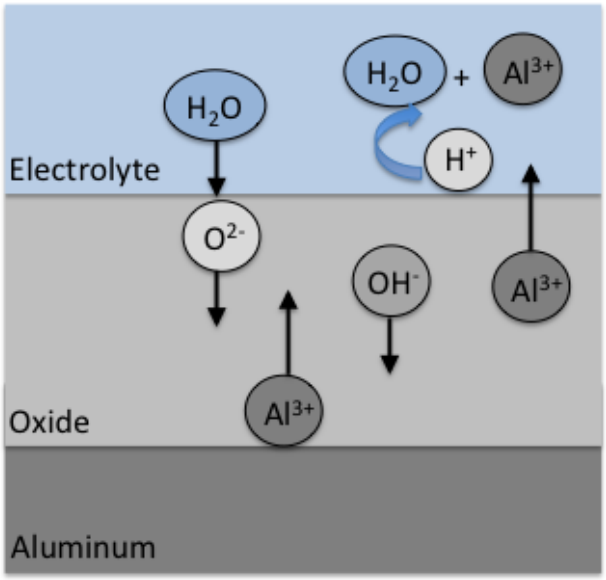

Figure 3.5 : The process of field enhanced dissolution and new oxide formation through ionic movements.

Oxygen containing ions, O^{2-} and OH^- are migrating inward from the electrolyte while Al^{3+} ions are migrating outwards simultaneously. For electrolytes containing phosphates and chromates those migrating Al^{3+} ions are involved in the oxide growth at oxide/electrolyte interface. The same effect is not observed for oxalate electrolytes. At lower field strengths they are usually trapped in the oxide structure. At the same time the electrolyte anions can migrate through the oxide and can be incorporated in its structure (Sulka, 2008).

The decomposition of the water is observed in the double layer due to the positive surface charge of the oxide in acidic electrolytes. Al^{3+} ions are migrating from the metal towards the solution while OH^- ions moves inward from solution to metal. OH^- ions are adsorbed at oxide/electrolyte interface to Al^{3+} ions. This weakens the bond between Al^{3+} and O^{2-} and O^{2-} ions moves to metal/oxide interface leaving more space for OH^- adsorption inside the oxide. The speed of Al^{3+} ions moving to solution side is much lower than OH^- ions entering the oxide lattice thus the process can be repeated several times before Al^{3+} ion reaches the solution. The process is schematically explained in Figure 3.5. The oxide grows only perpendicularly to the surface by the effect of neighbouring pore growth.

As seen clearly throughout this section a barrier type film is unavoidably present at the bottom of each pore. This film interrupts any electrical/chemical contact of the template with the base aluminium metal hence making the AAO unsuitable to be

used as a template directly after fabrication. The next sections will describe the strategies developed in the literature to overcome this obstacle.

3.1.2 Methodologies used for barrier layer opening

The first proposed strategy for the thinning of the barrier layer came from O'sullivan and Wood in 1970. They found that when the anodization potential was decreased, the field-assisted dissolution of the oxide rate would increase and hence the barrier layer thickness would be reduced as a consequence. This finding was a major step towards removing the barrier layer however the pioneering work for the elimination of the barrier layer was realized by Furneaux et al. in 1989 who characterized the parameters affecting the barrier layer thickness and focused on the complete elimination (and/or removal) of it by reducing the anodization potential in a controlled step-wise manner. A similar route has been undertaken later by many other groups who used re-anodization steps to reduce the barrier layer thickness (Jagminas et al., 2006; Santos et al., 2009; Chu et al. 2002; Saedi & Ghorbani, 2005). Decreasing the anodizing potential in a step-by-step way results in the formation of new, smaller pores at the base of previously formed larger pores (Figure 3.6). Penetrating the barrier layer by those smaller pores reduce the overall thickness and allows the tunnelling of electrical current through them.

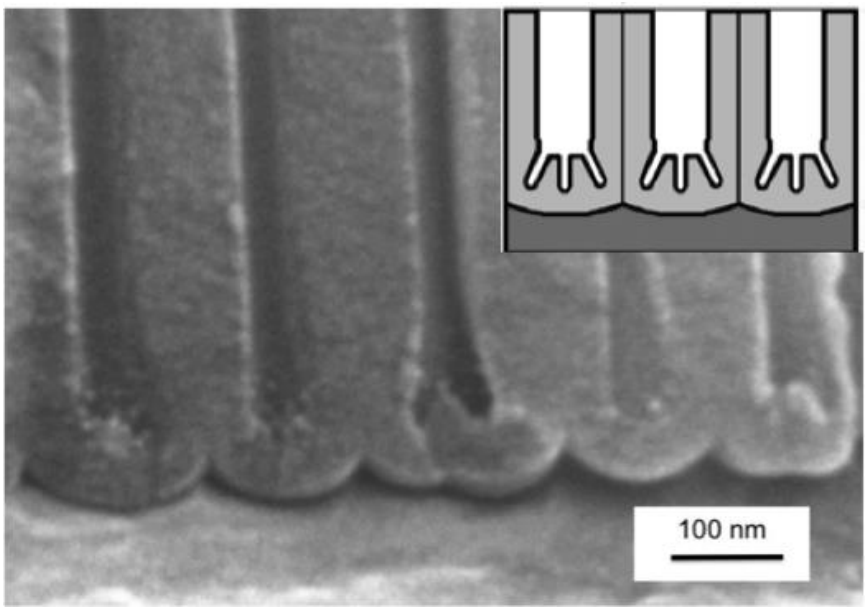

Figure 3.6 : Nucleation of smaller pores after controlled voltage reduction, the nset shows schematic representation of the pore perforation after voltage reduction steps (the inset is adapted from Saedi & Ghorbani, 2005).

Another approach to obtain open hole AAO membranes involves the complete detachment of the AAO structure from the base aluminium metal by various techniques. Some of those methods include etching the aluminium base in saturated $HgCl_2$ (Sui et al., 2002) or $HCl.CuCl_2$ (Xu et al., 2003) solutions followed by the dissolution of the barrier layer in H_3PO_4 solution, voltage pulse detachment (Yuan et al., 2006; Chen et al., 2007), reversing the polarity of the voltage in one step (Tian et al., 2005). However all those methods ends up with an extremely fragile, thin AAO membrane which, should be again fixed onto a metallic base substrate in order to create an electrical contact with the base of the pores. Moreover it is difficult to handle and transfer this brittle AAO membrane onto an appropriate substrate and further pore opening processes result in considerable widening of the pores disturbing the original integrity of the AAO structure.

Another alternative strategy to open the pore bottoms without stripping the AAO from its base involves anodization of the aluminium on a conducting metallic underlayer. In this case the morphology of the barrier layer tends to be different i.e. inverted barrier layers or presence of voids (Rabin et al., 2003; Choi et al., 2003) and the involvement of additional metallic layers compromise the simple strategy of forming AAO templates.

As summarized very briefly, barrier layer of the porous AAO structure constitute an obstacle for using AAO as an electrochemical deposition template. On the other hand it is also very well known that aluminium has high affinity for oxygen thus an oxide film is formed very quickly on the bare aluminium surface. This oxide film disturbs the electrical conductivity and even when removed completely it interferes with the quality of deposition. To overcome those issues a zinc deposition on the alluvium surface via a process known as *zincating* is performed for very long time in the industry (Lashmore, 1980).

As explained in the introduction section of this chapter, this study aims to produce DC electrodepositable AAO templates with the help of the innovative method (zincating) developed in our group (Urgen, 2006, Bayata, 2012)

3.2 Materials and Methods

High purity aluminium of 99.99% purity was used as substrate material for template preparation by anodic oxidation technique. The aluminium samples were cut to dimensions 0.02 x 2 x 10 cm. The anodized surface area was kept limited to 1.5 x 1.5 cm by masking with nail polish.

Structural characterization of anodized alumina templates were realized with a JEOL JSM_7000F field emission gun scanning electron microscope (FEG-SEM) at 30kV. Measurements of nanopore diameters and barrier layer thicknesses were performed using Image J ver 1.45 processing software.

Scanning Auger electron microscopy (SAM, JEOL FEG SAM, 9500F)) with depth profiling capacity is used for the investigation of zincated samples. AES spectra are obtained in an energy range 200-1700 eV using probe beam current of 10 nA and primary acceleration voltage of 10 keV. Sputter depth profiling is conducted via ion gun attached to the SAM. For depth profiling ion gun energy at the beginning for 80 mins of sputtering was kept at 3000 eV (equivalent to a sputter rate of 30 nm/ min for SiO_2) and then the energy is lowered to 1000 eV (equivalent to a sputter rate of 3 nm/ min for SiO_2) for a more controlled sputtering while reaching the oxide metal interface. For over coming the common problem of sintering resulting in deformation of porous structure observed during sputter depth profiling of non conductive nano structures (porous titanium and anodized aluminium) electron bombardment of the surface is used. For supplying electrons to the surface and electron source with tunable energy was used. During evaluation of the acquired spectrum the energies was corrected with respect to reference of C KLL (270.958 eV) when needed. The chamber pressure during analysis was 1-1.5 $x10^{-8}$ Pa.

3.3 Experimental

This section presents the experimental procedures of the template preparation and the optimization of the templates for electrodeposition of metallic nanowires. First, the surface preparation and the anodization conditions of high purity aluminium will be described. The barrier layer opening optimization of the as-prepared templates will follow this in order to make the templates suitable for the electrodeposition of metallic nanowires without applying any additional procedures. And finally the

production of three nanowire array, nickel, gold and silver will be shown. The process is illustrated in Figure 3.7.

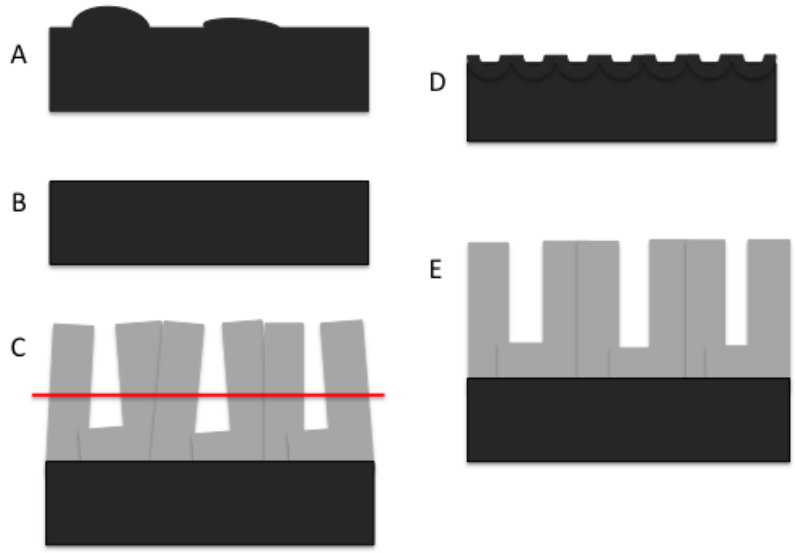

Figure 3.7 : Fabrication steps of porous AAO template. A) Annealing, B) Electropolishing, C) 1st step anodization, D) Chemical etching and D) 2nd step anodization.

Preparation of AAO templates:

The aluminium samples are first subjected to a series of pre-treatment procedures. Aluminium specimens' surface and structural quality have major influences on the final anodized nanoporous architecture. During anodizing, pores start to nucleate randomly at surface faults, grain boundaries and scratches (Zhao et al., 2006). Therefore controlling the properties of the starting material affects greatly the self-organization of pores later during anodizing.

The pre-treatment procedures define the nature of the oxide film forming on aluminium surface prior to anodizing (Oh et al., 2006). An appropriate pre-treatment starts with annealing in order to remove any internal mechanical stress to promote a homogeneous pore growth over the whole surface area. The specimens were annealed below melting point at 400°C for 4 h. Following annealing the surface of the specimens were degreased in acetone and in ethanol respectively. Then they were immersed in 10% NaOH solution at 60°C for 5 to 10 seconds to remove the naturally forming oxide layer and neutralized in 5% HNO_3 solution to obtain a homogeneous oxide film on the surface prior to electropolishing.

Polishing of the surface for smoothing any remaining surface roughness is certainly the most crucial step before anodizing. The electropolishing of the specimens were realized in a commercial polishing solution at 55°C at 15 A/dm^2 current density for 5 to 7 minutes. The electropolished surfaces are free of stress and occlusions and have a highly reflective mirror-like appearance.

Anodizing of electropolished aluminium specimens was realized in 0,3 M oxalic acid ($H_2C_2O_4$) under mild potentiostatic anodization conditions. For oxalic acid electrolyte the potential working window without burning or breaking-down the oxide film is between 30-100 V (Lee et al., 2006). It is established by Masuda and Fukuda that the best results for self-ordering are obtained via two-step anodization so the anodization process was realized in two different steps that are separated by an oxide removal intermediate step. The first step of anodization take 1 h under 40 V anodization potential at 15°C. After the end of the first step samples were chemically etched in a mixed solution of H_3PO_4 (6 wt%) and H_2CrO_4 (1.8 wt%) at 60°C for 1 h. The chemical etching time depend on the oxide thickness, which is it self a function of potential, and electrolyte type. After the removal of the oxide layer aluminium surface is left with a hexagonally pre-patterned structure. This structure ensures the self-ordered homogeneous growth of the final porous oxide array. The second step was realized at 70V cell potential at 5°C for 5 min. During all anodization steps the electrolyte was stirred vigorously with a magnetic stirrer. Effective stirring is important in order to limit the temperature raise and to prevent the concentration change at the bottom of the pores that both may cause breakdown of the oxide film.

The adaptation and the optimization of the zincating treatment were realized on two differently prepared anodized aluminium template structure in order to allow direct electrodeposition of metallic nanowires inside the nanoporous AAO. The first AAO template was prepared by a regular two-step anodization method as described in section 3.2.1. The second template was subjected to a barrier thinning process in order to limit and control the pore enlargement during zincating after the end of the second anodization step. The second set of anodization with barrier layer thinning procedure was performed on the samples to reduce the pore widening by shortening the zincate treatment time. The thinning process was made in the same electrolyte after the end of the second anodization step. The anodization voltage was reduced in

a stepwise manner with decrements of 0.1 V per second until it reaches 15 V. The samples were anodized at that potential for 30 min.

Barrier layer removal via zincating:

Following anodization the zincating process was realized in a zincate solution containing 120 g/l NaOH (to maintain the pH), 20 g/l ZnO, 50 g/l C_4H_4KNa, 2 g/l $FeCl_3$ (improves the adhesion of the deposits together with tartarate ions) and 0-1 g/l $NaNO_3$ (limits the thickness/amount of the deposits). For the optimization of zincating parameters temperature and agitation mode were selected as variables. In the first set of experiments a zincate bath temperature of 30 ± 1 °C was used, and the samples were immersed in zincate bath both with and without ultrasonication for different time durations. The second set of experiments was executed at 22 °C again with and without ultrasonication using immersion time as a variable. Ultrasonication is realized in a commercial ultrasound bath. After zincating process the samples were immediately immersed in deionized water to stop the etching effects and rinsed thoroughly for several minutes.

Nanowire array fabrication by DC electrodeposition:

Furthermore the applicability of the technique was demonstrated by direct electodeposition of nickel into zincate treated regular AAO templates. Electrodeposition of nickel nanowires into the pores of zincated aluminium was conducted by using Watts nickel plating solution ($NiSO_4.6H_2O$ 240-300 g/l, $NiCl_2.6H_2O$ 30-90 g/l, H_3BO_4 30-45 g/l), in a 250 ml cell at 60 $^{\circ}$C. The cathode current density was maintained between 4-6 A/dm^2. The primary cathodic polarization is 4v. And the pH of the solution was kept between 3-4.5. The anode was high purity nickel. During electroplating the solution was agitated in order to limit the hydrogen evolution from the cathode's surface. After the electrodeposition AAO template and base aluminium metal were dissolved in 10% NaOH solution at 60 $^{\circ}$C until the end of the visible reaction.

3.4 Results and discussions

The results will be presented in three sections. The first section will show the AAO template morphology after the two step regular anodization procedure. The second section will discuss the barrier layer removal procedure by zincating method and will

follow on the optimization of zincating parameters for two different AAO templates. The last part will show the effectiveness of the zincating method by fabricating large area arrays of nanowires of various metals.

3.4.1 Template morphology of AAO films

Figure 3.8 shows the morphology of anodized AAO templates after the first step. The mean pore diameter is 17±2 nm and the interpore distance 94 ± 9 nm. After the chemical etching the hexagonal pattern (Figure 3.9) remaining at the aluminium surface constitute the base for the second anodization process.

The second anodization step brings the pore diameter to 26 ± 3 nm and the interpore distance 180 ± 10 nm (Figure 3.10).

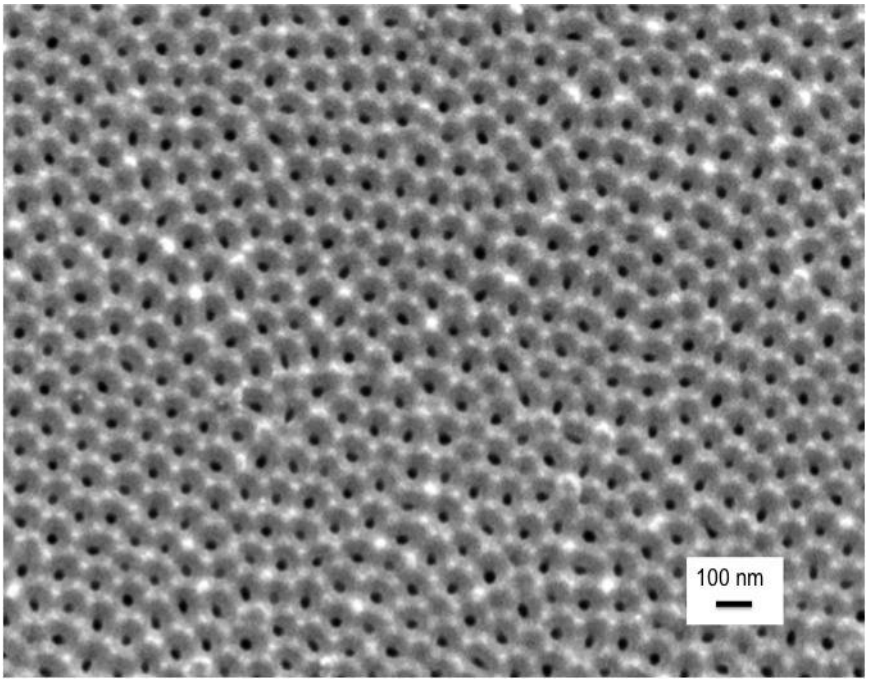

Figure 3.8 : AAO template morphology after the first step anodization.

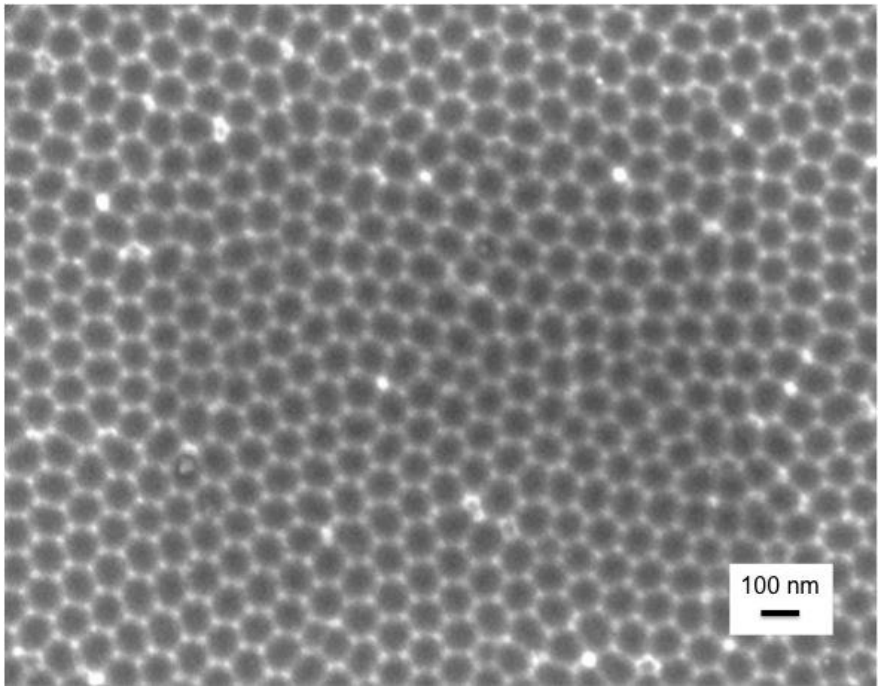

Figure 3.9 : The formed pattern on the base of the AAO template after the chemical etching.

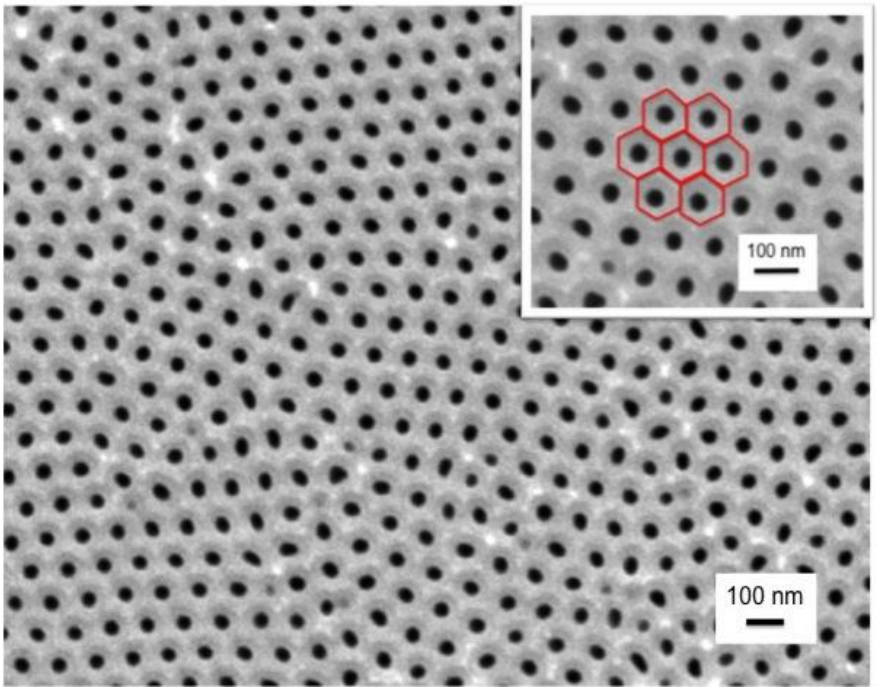

Figure 3.10 : AAO template morphology after the second step anodization with distinct hexagonal pore arrays.

Prepared AAO structures, with their controlled pore dimensions and porosity is ideal templates for subsequent direct electrodeposition of metallic nanowires. By this way a large area of metallic nanowire array can be obtained easily once after the AAO template is removed at the end of the deposition process. However for

electrodeposition to be possible, the AAO template should be either electrically conductive itself or should be fixed on a conductive metallic layer. Obviously to use the templates directly without complicated procedures to make them conductive should be the primary point of interest for simplifying further applications.

As mentioned earlier in this chapter, during anodic oxidation of aluminium first a barrier type oxide film is formed on the surface (Figure 3.11). Subsequently this film may evolve into porous structure under right conditions as explained in the previous section. Even when the porous structure is formed the thickness of this first formed barrier layer on the pore bottoms will remain constant because of the simultaneous oxidation at metal/oxide interface and field assisted dissolution at oxide/electrolyte interface As a result the barrier layer sits at the bottom of the pores as a thin, compact dielectric layer and will only allow the passage of the current inhomogenously due to its structural faults. This thickness is only a function of forming potential, thus independent of electrolyte choice and anodization conditions such as pH and temperature. Under optimum conditions, leading to self-ordering of the AAO structure, the barrier layer thickness reaches usually half of the interpore distance (Sulka, 2008). Hence if the electrochemical deposition of metals into the AAO template is desired the barrier layer must either be removed completely or thinned down to a few nanometres in order to establish an electrically conductive path between the AAO film and the base aluminium metal. So far, many research groups have tried to achieve this goal by following various strategies. The most important ones of those strategies will be briefly relieved in the following section.

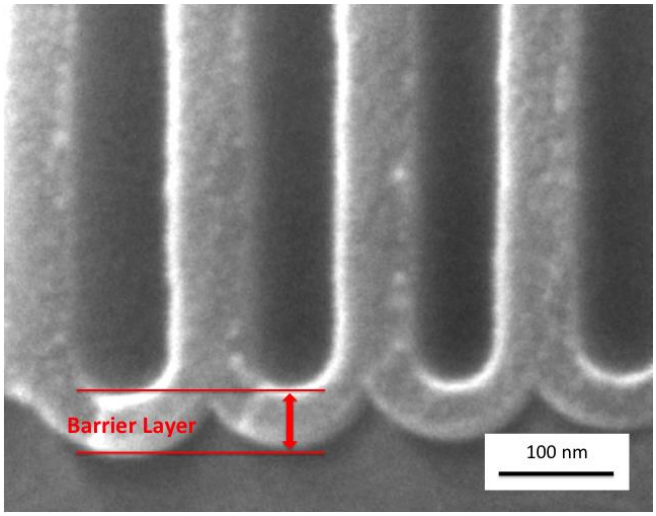

Figure 3.11 : Pore bottom morphology of a porous anodic aluminium oxide template.

3.4.2 Barrier layer opening and optimization

Zincating is a surface treatment method whereby aluminium is immersed in an alkaline zincate solution. The main principle of the method is the formation of zinc deposits via immersion by displacement from an alkaline zincate solution. During zincate treatment process an electrochemical exchange reaction takes place between the aluminium metal and the zinc complex in the solution. While the more electronegative aluminium metal is etched away (dissolved) in the alkaline zincate bath, the more electropositive zinc metal is deposited to its surface by a displacement reaction. The reaction stops spontaneously by the whole coverage of the bare metallic aluminium surface available with zinc metal. The reaction rate depends on the composition of the zincate bath.

The anodic reaction can be expressed as

$$Al + 3OH^- \rightarrow Al(OH)_3 + 3é \qquad (3.10)$$

the cathodic reactions are;

$$Zn(OH)_4^{2-} \rightarrow Zn^{2+} + 4OH^- \qquad (3.11)$$

$$Zn^{2+} + 2é \rightarrow Zn \qquad (3.12)$$

Hence the overall reaction is

$$2Al + 6OH^- + 3Zn^{2+} \rightarrow 3Zn + 2Al(OH)_3 \qquad (3.13)$$

In our group we adapted the same technique to nanoporous AAO membrane for the first time to open the pore bottoms by dissolving the barrier layer due to high alkalinity of the solution and depositing a thin zinc layer to inhibit further reoxidation. Via zincating alumina templates become suitable for direct electrodeposition through a straightforward and easy one step technique. The resulting AAO template still holds on firmly to the base aluminium metal, which is now coated with a very thin layer of zinc. The templates obtained by this way are easy to handle, robust and suitable as it is directly for DC electrodeposition. Moreover by adjusting correctly the time and temperature of the zincate solution it is possible to remove effectively the barrier layer without significant dissolution of pore

walls. By this method direct DC electrodeposition of metallic nanowires on the AAO templates become possible and by dissolving the AAO template after electrodeposition free-standing arrays of metallic nanowires can be obtained. A schematic representation of the process is given in Figure 3.12.

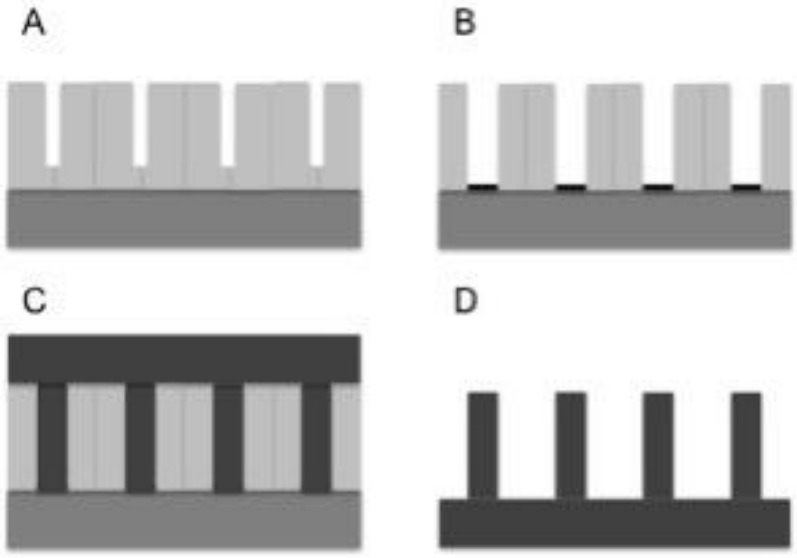

Figure 3.12 : A) Formation of AAO template through anodization, B) Zincating of the pore bottoms, C) DC electrodeposition of metallic nanowires on the zincate treated AAO template and D) Freestanding metallic nanowire arrays after the dissolution of AAO and metallic aluminum in an alkaline solution.

Figure 3.13 shows the typical surface and cross sectional view of the aluminium sheets after the two-step anodization procedure. The film structure is characterized by a close packed hexagonal array of columnar cells tightly connected to the metal oxide interface by a compact barrier type oxide layer. The first step of the anodization process acts, after etching, as the initial sites of pore growth resulting in a more ordered pore structure after the second anodization.

Under the specified anodization conditions, the average pore diameter of the hexagonal array is 25 ± 3 nm. In order to study the barrier layer thickness cross sections of anodized aluminium sheets are observed without detaching the AAO template from the base aluminium metal. The SEM micrographs show that the barrier layer thickness is approximately 85 nm (Figure 3.13) and homogeneous throughout the whole porous structure

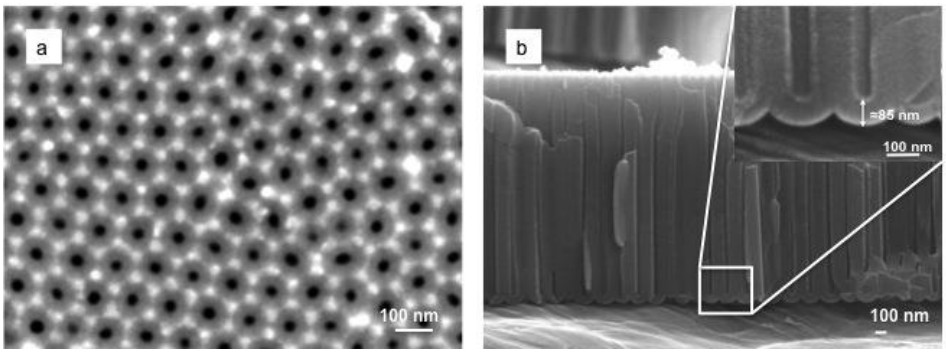

Figure 3.13 : The surface (a) and cross-sectional (b) micrographs of nanoporous anodic aluminum oxide film after the two-step anodization procedure.

Following anodization the specimens were treated with the zincate solution at two different temperatures, 22 ± 1 °C and 30 ± 1 °C, in both cases with and without ultrasonic agitation.

In the experiments conducted under stagnant conditions it was observed that the pore structure of the AAO broke down completely after 40 sec of zincate treatment at 30°C (Figure 3.14). At this point, albeit considerably thinner, the barrier layer was still not entirely removed and could be noticed in the base of many pores.

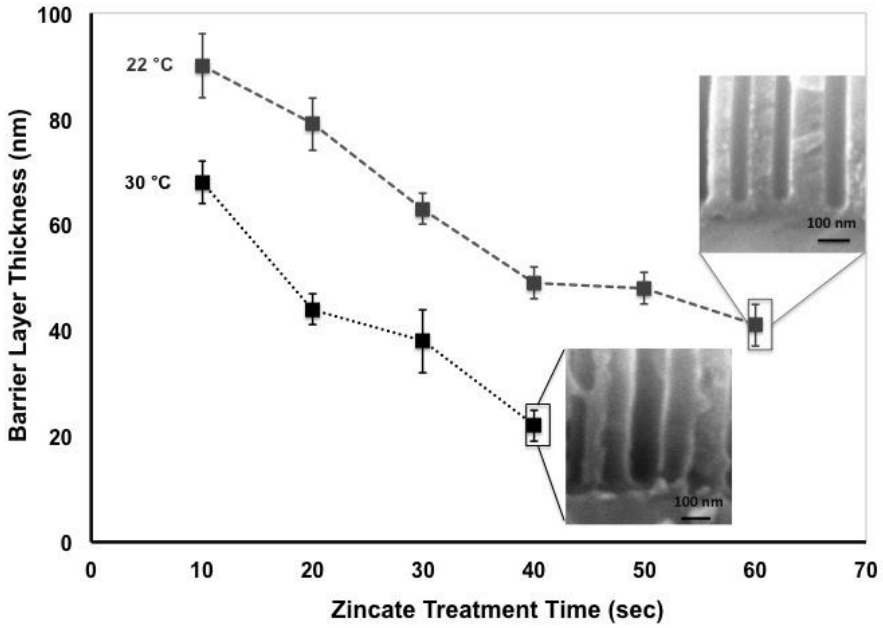

Figure 3.14 : Effect of zincate treatment on barrier layer thickness at stagnant conditions at A) 22 °C and B)30 °C. The SEM micrographs shows the barrier layer thikness after 60s sec for A and 40 sec for B.

On the other hand at 22 °C, even after 40 second of zincate treatment, the barrier layer was almost intact and had a thickness of approximately 49 ± 3 nm.When the

barrier layer removal was performed under ultrasonication a dramatic change in the dissolution behaviour of barrier layer was observed immediately. As the Figure 3.14 reveals, at 30 °C after 40 sec of zincate treatment the barrier layer vas totally removed and the pore bottoms were exposed. The columnar porous structure was unharmed and pore walls were not dissolved as it was under stagnant conditions after the same zincate treatment time. However at 22 °C even after 60 sec of zincate treatment the barrier layer, even thought significantly thinner, could still be noticed at the bottom of the pores.

The total exchange process can be treated as an electrochemical corrosion process. Zn^{2+} ions exist in the alkaline zincate solution in $Zn(OH)_4$ form. Considering the whole system the total reaction is; $3Na_2Zn(OH)_4 + 2Al = 2NaAlO_4 + 3Zn + 4NaOH + 4H_2O$. The reaction is under chemical control mechanism at ZnO concentration higher than 0.1M. But without any agitation a concentration change on the metallic surface inside the small pore bottoms occurs in the first few seconds of the reaction due to the depletion of dissolved active species in the vicinity of the surface. The concentration change cause a concentration polarization effect, shifting the reaction mechanism to diffusion controlled. In this situation the cathodic reaction is fairly limited while the anodic reaction, aluminium dissolution, keeps going on. This explains why under stagnant conditions porous structure is more seriously and quickly destroyed without the barrier layer dissolution. This condition also explains why the porous structure at the top of the alumina is almost completely broken down whereas the columnar structure at the bottom is not. On the other hand ultrasonication, by helping the replenishment of the solution inside the porous structure is obviously more effective for precise opening of the pore bottoms and simultaneous zincate deposition. The results show that by using the zincate treatment in ultrasonic environment neither the columnar structure nor the pore walls are visibly damaged (Figure 3.15).

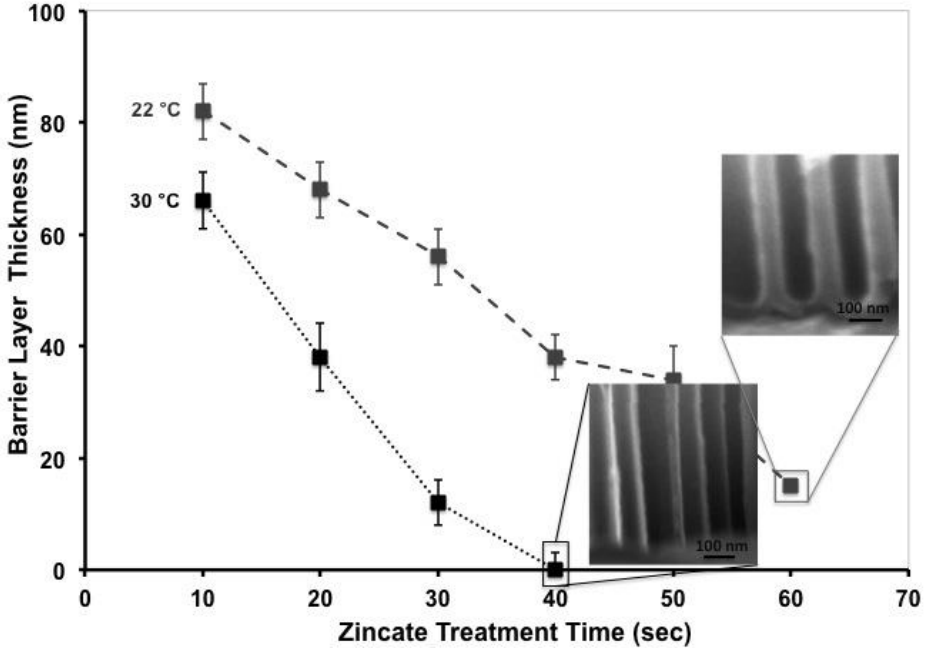

Figure 3.15 : Effect of zincate treatment on barrier layer thickness with ultrasonication at 22 °C and 30 °C zincate bath temperatures.

However while the zincate treatment removes the barrier layer from the pore bottoms it should also be mentioned that the enlargement of the pore diameters during the process is unavoidable to a certain extent. Figure 3.16 displays how the pore diameters were affected in specific zincate treatment conditions, which gave the best barrier layer removal results at two different temperatures under ultrasonic conditions. On the other hand, uncontrolled widening of the pores must be avoided if homogenous pore filling and obtaining ordered arrays of nanowires are the main objectives. In this case, to limit pore diameter enlargement as much as possible, it is a good strategy to combine existing barrier layer removal methods with the zincate treatment. To realize this, perforation of the barrier layer by reducing step by step the anodization voltage at the end of the end of second anodization was selected.

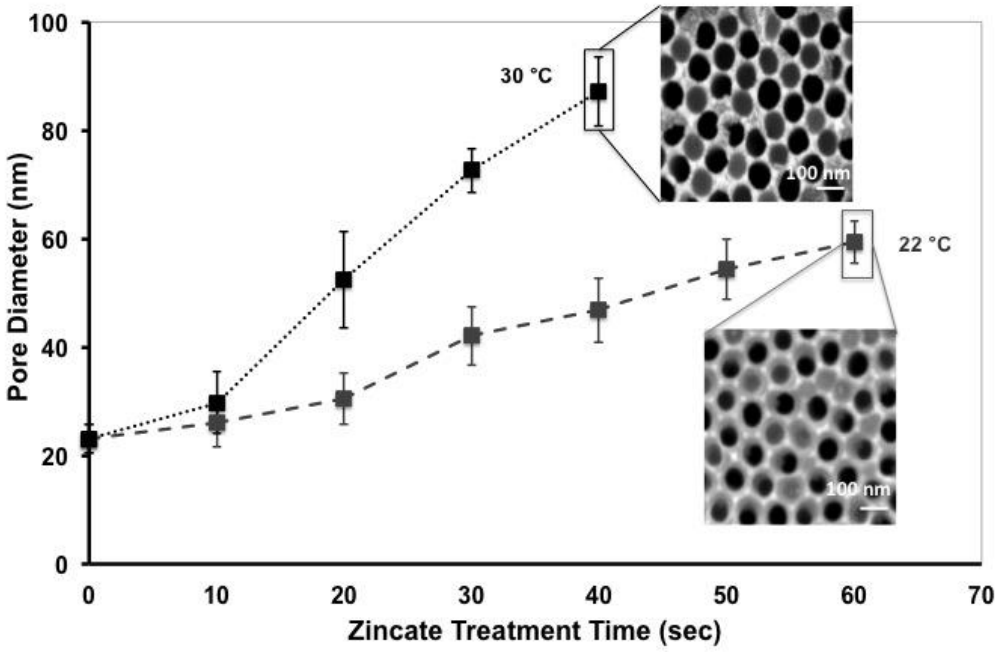

Figure 3.16 : Pore diameter enlargement with zincate treatment time both for 30 °C and 22 °C under ultrasonic conditions.

The principle behind this strategy can be explained as follows. In steady state anodization, aluminium cation dissolution from the metal/oxide interface is equal to the Al_2O_3 formation. When the potential is reduced the Al^{3+} supply is dropped resulting in a decrease in oxide formation rate while the oxide dissolution rate at the oxide/electrolyte interface remains constant. Pore branching occurs at this stage because the voltage is reduced again before the formation and growth of the new pores takes place (Saedi & Ghorbani, 2005). When this method is applied prior to zincating, the minimum immersion time required to remove the barrier layer in the ultrasonic zincate bath at 30 °C can be reduced to 25-30 sec instead of 40 sec for complete barrier layer removal. The process therefore resulted in significantly less enlarged pore diameters. Figure 3.17 displays the surface and the cross section of an anodized aluminium sample, which went through a barrier layer perforation step via voltage drop. The barrier layer thickness is reduced by several nanometres as compared to the regular AAO barrier layer thickness. However the thinned template is still not entirely suitable for DC electrodeposition of metallic nanowires mainly because the thinning process leaves small fluctuations among the thickness of the barrier layer. At this point DC electrodeposition is highly unstable and it is highly unlikely to achieve uniform filling of the pores by DC deposition. The

inhomogeneities of barrier layer thicknesses, albeit very small, will lead to large current fluctuations and hence will result in the irregular deposition of nanowires into the pores. When the voltage reduction method is applied a branched small pore with decreased overall barrier layer thickness in the bottom of each major pore is generated. This type of structure can be easily removed with a short zincate treatment resulting on the complete removal of barrier layer with less pore enlargement.

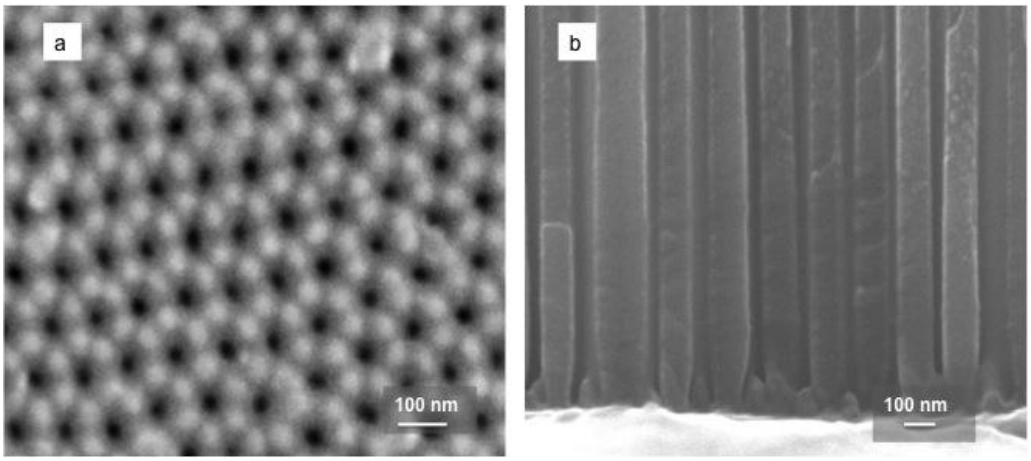

Figure 3.17 : The surface (A) and cross-sectional (B) micrographs of barrier layer thinned nanoporous anodic aluminum oxide film after the two-step anodization procedure.

Figure 3.18 shows the change in barrier layer thickness with different zincate immersion times following the thinning process. After 30 sec of immersion treatment with zincate solution, the pore diameter of barrier layer thinned alumina is 56 ± 3 nm while after the same treatment time the regular alumina had a pore diameter of 77 ± 5 nm.

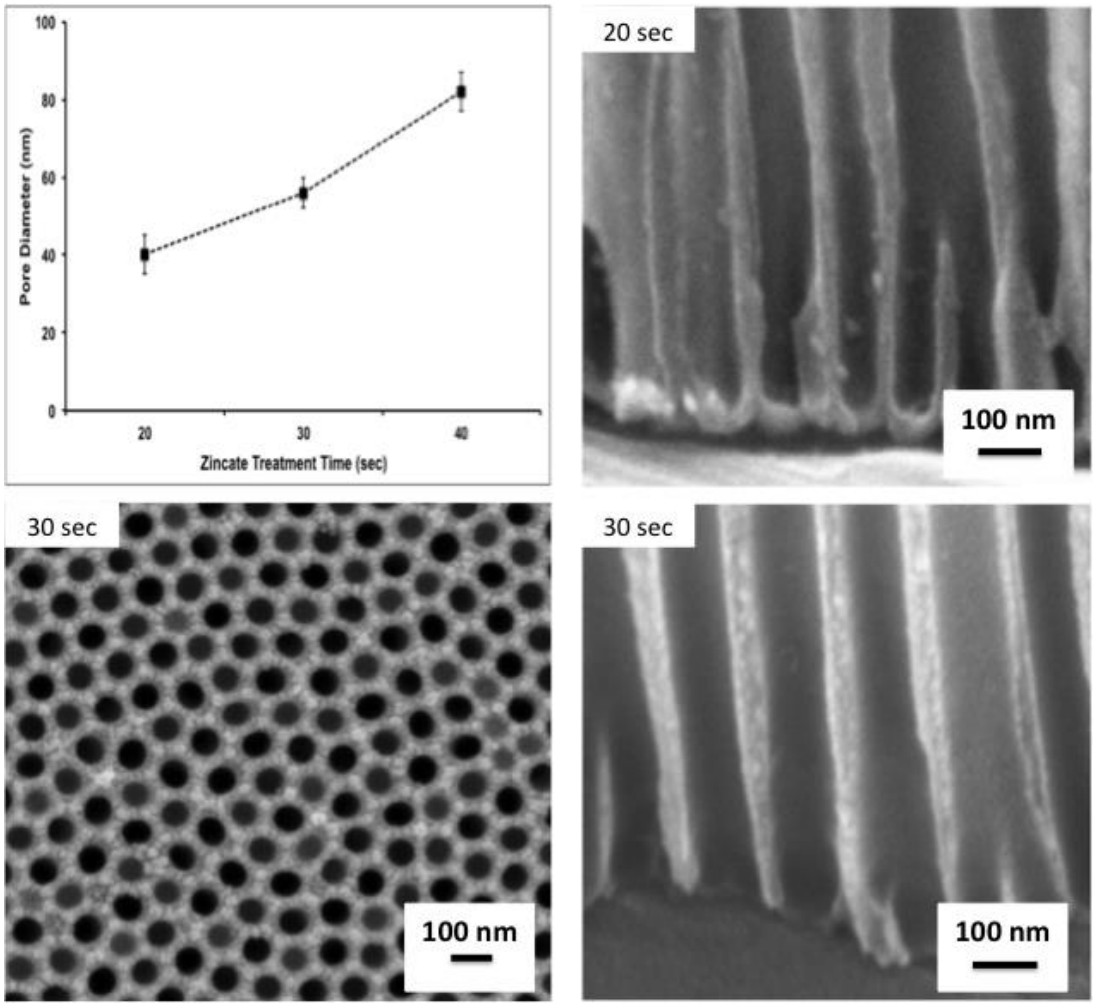

Figure 3.18 : Zincate treatment time effect on barrier layer thickness 20 sec and 30 sec respectively and pore diameter change versus zincate treatment time in barrier layer thinned AAO at 30°C.

The presence of the very thin zincate layer cannot be seen in scanning electron microscopy pictures or via energy dispersive x-ray spectroscopy. Although it will be presented in the next section that without zincating, DC electrodeposition of nanowires is not possible and that the sole removal of the barrier layer only via wet chemical etching methods is not sufficient to obtain regular and robust nanowires. Yet to demonstrate the presence of the thin zinc layer on pore bottoms of AAO templates, Auger electron spectroscopy (AES) has been used. Since the zinc layer is only present at the pore bottoms, the columnar AAO structure has to be removed step by step from the top towards the bottom. To realize this, the AAO templates' surfaces have been sputtered by Ar^+ ion flux. While sputtering, the integrity of surface structure has been verified by SEM images throughout the whole process (Figure 3.19). During sputtering, electrons supplied to the surface simultaneously

avoided the positive charging problems induced by the charged Ar^+ ions used for sputtering.. Figure 3.20 shows the presence of the zinc layer after 140 minutes of intermittent sputtering of the surface.

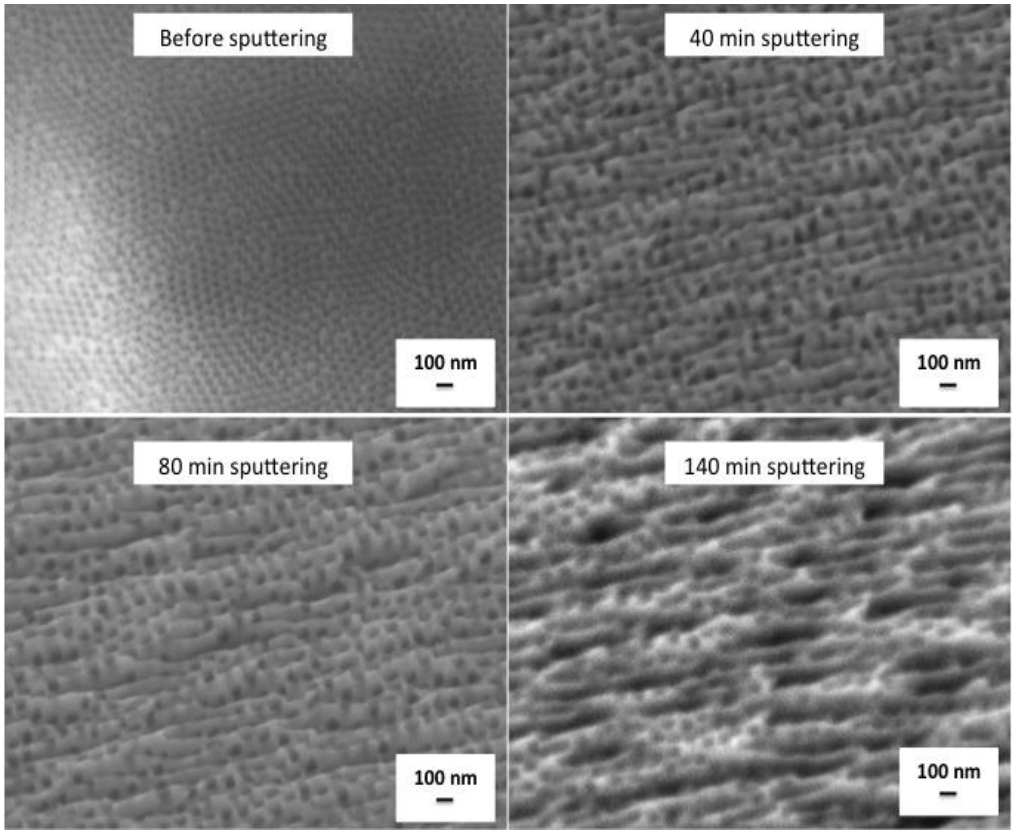

Figure 3.19 : Scanning electron microscopy images of the AAO surface during sputtering process recorded at regular intervals between the beginning of the sputtering and the end of the sputtering (while Zn layer is first observed in the AES spectrum). The etch direction can be noticed from the images.

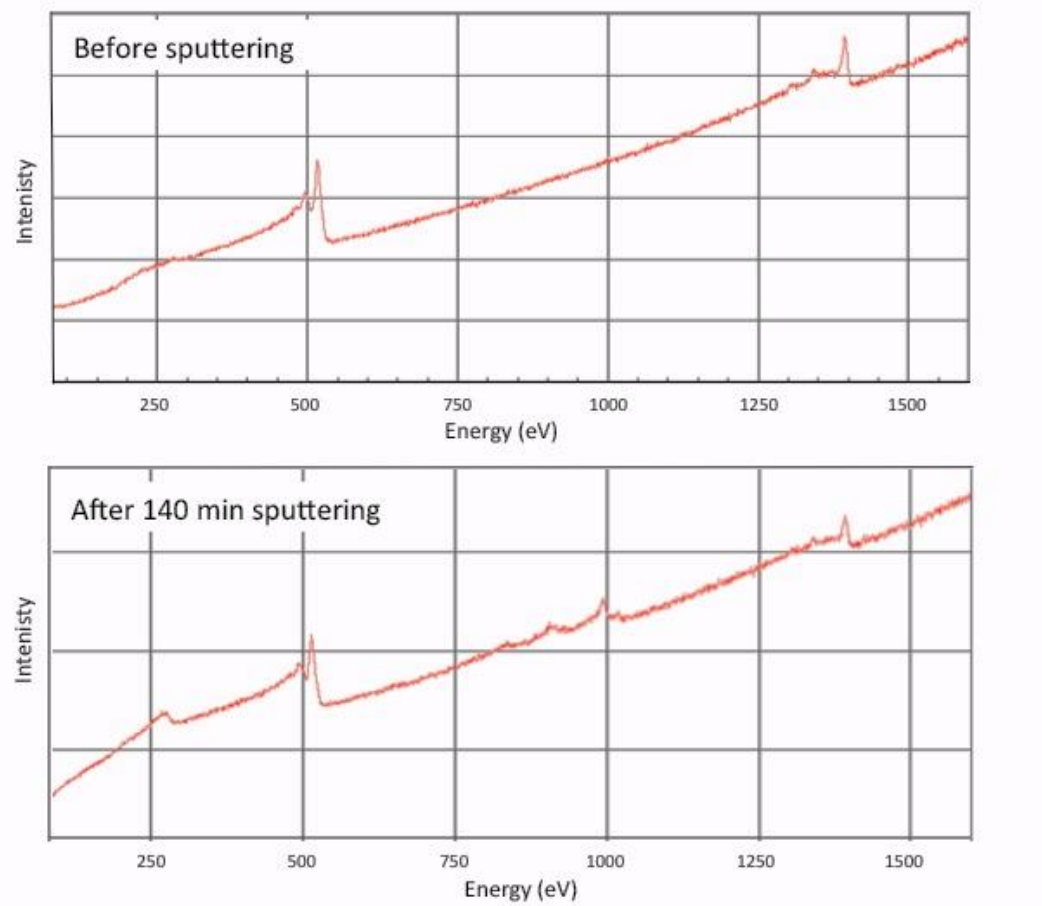

Figure 3.20 : Auger scanning electron microscopy results of a zincate treated (45 sec) AAO membrane before sputtering and after 140 min of sputtering. After this period Zn LMM peak became visible around 900 eV.

3.4.3 DC electrodeposition of metallic nanowires

As mentioned in previous sections electrodeposition is one of the most versatile and inexpensive techniques, which allows the filling of AAO templates by various metallic materials. Up to now, DC electrodeposition of metallic nanowires into porous AAO templates have only been possible by completely separating AAO structure from aluminium substrate, removing the barrier layer via wet chemical etching method and finally sputtering a thin metallic connection on one side of the membrane (Brumlik and Martin, 1991). Albeit the method has been successful for preparing various metallic nanowire arrays the process itself is troublesome and time consuming. Other methods, as mentioned in the previous section, strategizing the removal and/or thinning of the barrier layer are generally very laborious and they do not always yield to highly controlled structures. Therefore without separation of the barrier layer from the AAO template the only possible ways to electrodeposit metals

into AAO templates are by using either AC or pulse current electrodeposition processes. Alternative methods such as AC and pulse electrodeposition have only been possible because of the rectifying properties of the barrier layer (Wu et al., 2012; Gerein & Haber, 2005). Due to valve metal properties of aluminium when alternating current is used AAO conducts the current preferentially in the cathodic direction. The barrier layer acts as a rectifier and while at cathodic half cycles ions are reduced, at anodic cycles they are not reoxidized. When pulsed current electrodeposition is used in addition to the rectifying properties of the barrier layer there is a recovery time for metallic ion concentrations at the bottom of the pores which allows to fabricate slightly more homogeneous nanowires by avoiding high cathodic potentials that can interfere with the deposition process (Nielsch et al., 2000). However AC and pulse depositions do not result in a pore filling structure nearly as regular with a controlled morphology and compact structure as DC deposition (Wu et al., 2012).

By using zincating method to remove the barrier layer of the AAO templates and to make the pore bottoms conductive it becomes possible to use DC electrodeposition and to obtain homogeneous arrays of freestanding metallic nanowires. The freestanding nanowire arrays produced via this method are nickel, gold and silver nanowires.

Nickel Nanowires:

To illustrate the applicability of the zincating technique for DC electroplating of metals, electrodeposition of nickel nanowires on the zincate treated AAO templates was realized. The electrodeposition was done by using a homemade Watts electroplating bath. (30-45gr H_3BO_4, 30-90gr $NiCl_2.6H_2O$, 240-300gr $NiSO_4.6H_2O$). The pH of the solution was kept between 3 and 4.5. The current density was kept between 2-10 A/dm^2. The temperature of the nickel bath was constant at 50 ±5 °C. The working electrode composed of nanoporous AAO with microscopic zinc layer on pore bottoms and aluminium metal on the base was cathodically polarized prior to the immersion into the electroplating bath. The anode was a pure nickel sheet. The electroplating duration was 1 h. After the electroplating process, the substrates were immersed in 10% NaOH bath at 60°C to dissolve completely the aluminium and the anodic aluminium oxide.

Figure 3.20 shows the surface of the freestanding nickel nanowire arrays after the dissolution of AAO templates. The average nanowire diameter was calculated by using image J software as 135 nm. The surface of the array was highly homogeneous with more than 75% of the nanowires having a diameter distribution between 100 and 150 nm range as seen in the inset of Figure 3.20.

Figure 3.21 shows the cross-sectional image of the freestanding nickel nanowire array. The average length of the nanowires is about 1 μm. It is clearly seen from the cross-sectional view that the array is homogeneous in length and the nanowires stands without collapsing or bundling on the nickel base.

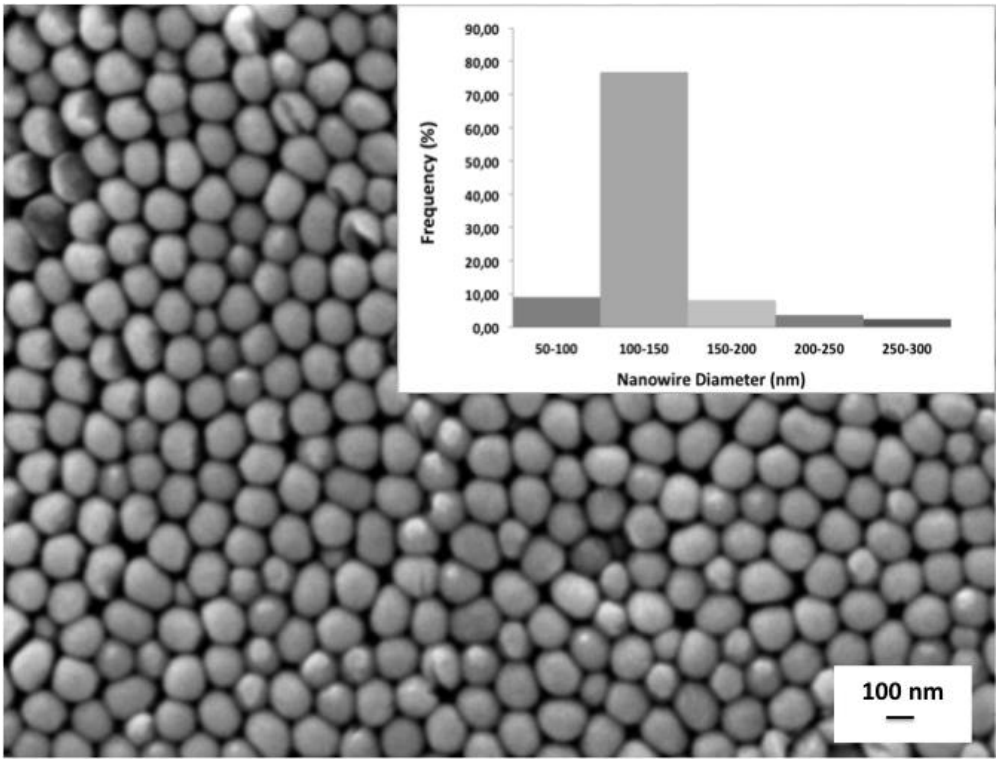

Figure 3.21 : Surface image of electrodeposited nickel nanowire arrays. The inset in the figure shows diameter distribution percentage of the nanowires.

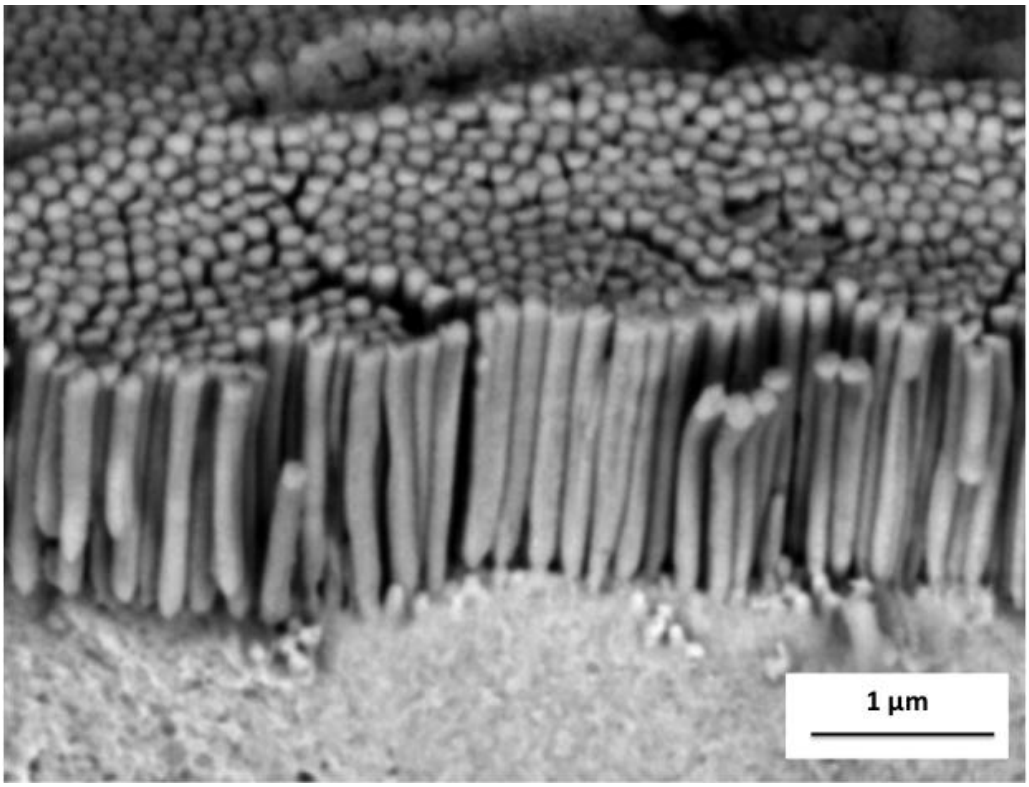

Figure 3.22 : Cross sectional image of the free-standing nickel nanowire array.

In addition, to show the effectiveness and the necessity of the zincate treatment technique AAO templates were treated with only highly alkaline NaOH solution (which did not contain any zinc compound). The alkaline NaOH solution dissolved the oxide. When those templates were used for nickel nanowire deposition the resulting structures came out totally different than the ones previously treated with the zincate solution (Figure 3.22). As illustrated in Figure 3.22 nickel coating was clustered on the surface and not grown as regular, homogeneous wires. The main reason why the process is not working without zincating is because aluminium is a very active element and it oxidizes easily hence causing the total loss of adhesion, or resulting on poor adhesion of plated films due to this natural oxide layer (Robertson & Ritchie, 1997). Hence the zinc layer provides a suitable surface for the electrodeposition of metals and removing solely the barrier layer does not make AAO templates adequate for DC electrodeposition. The thin zinc layer coating the aluminium metal is crucial to obtain regular, robust and freestanding nanowire arrays.

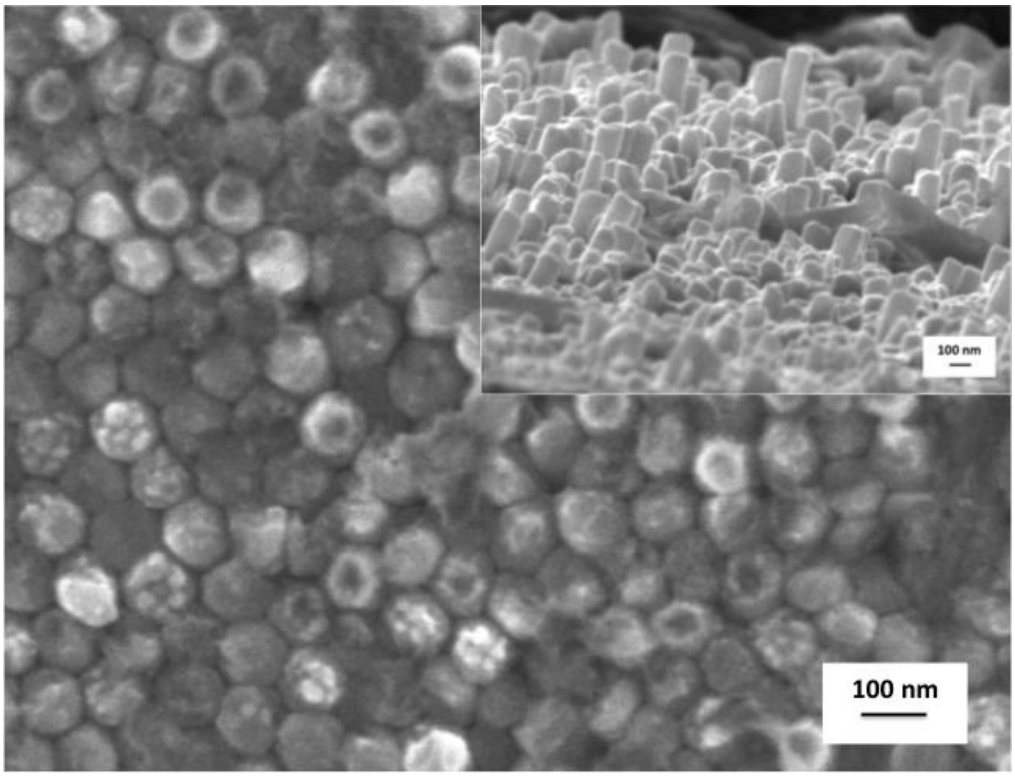

Figure 3.23 : Surface and cross-section images of electrodeposited nickel nanowire arrays on a NaOH treated AAO template.

Gold Nanowires:

Electrodeposition of gold was done in a typical two-electrode cell with 50 ml volume. The surface area of AAO templates was reduced to 1,5 x 1,5 cm^2 by masking with nail polish. The AAO templates were treated with the zincate solution prior to electrodeposition and washed several times with deionized water. A platinized titanium mesh was used as the counter electrode. A commercial gold electroplating solution (Auruna 311) was used. The solution has a gold content of 2-4 gr/l and a deposition rate up to 0.15 μm per minute. The pH of the solution is 0.6 and the maximum working temperature is 40°C. The working current density was 4 A/dm^2.

Figure 3.24 shows the surface of the as fabricated Au nanowire arrays. The average nanowire diameter is 133 nm. The surface of the array is again highly homogeneous with more than 77 % of the nanowires having a diameter distribution between 100 and 150 nm range as seen in the inset of Figure 3.24. Figure 3.25 shows the energy dispersive x-ray spectra of the gold nanowire array after the dissolution of the aluminium template.

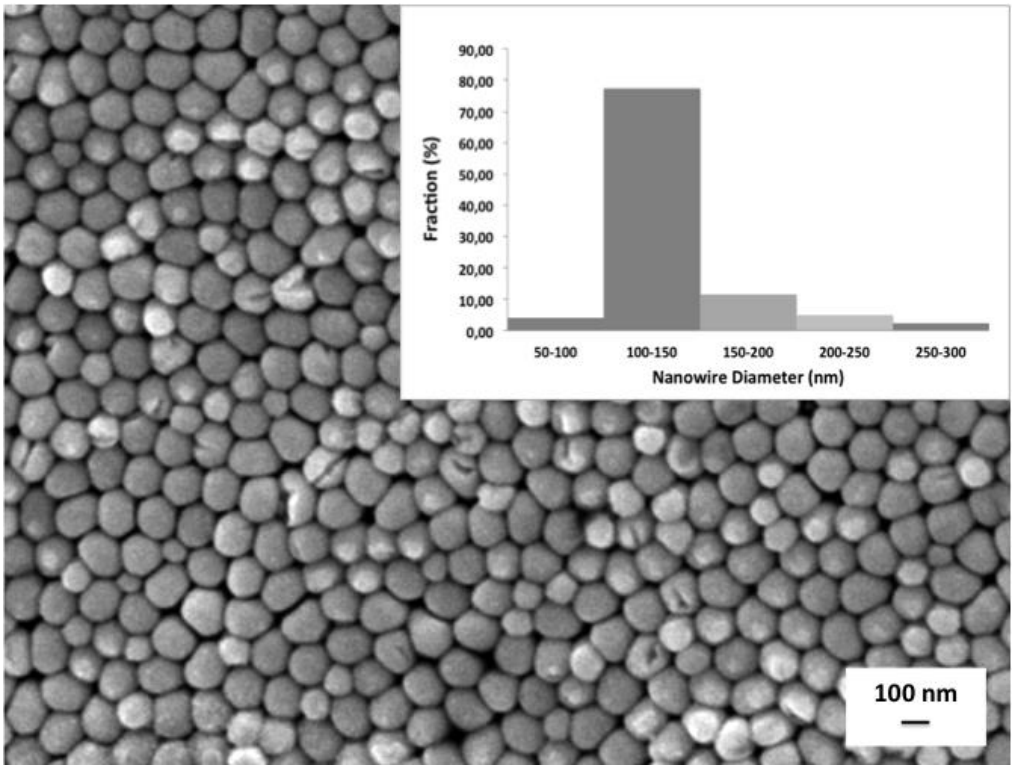

Figure 3.24 : Surface image of electrodeposited gold nanowire arrays. The inset in the figure shows diameter distribution percentage of the nanowires.

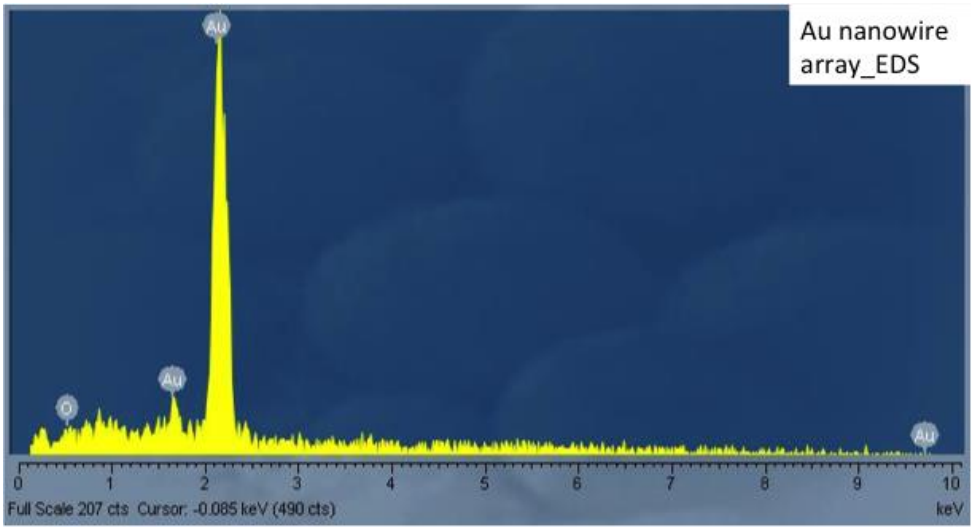

Figure 3.25 : Energy dispersive x-ray spectra of the gold nanowire array.

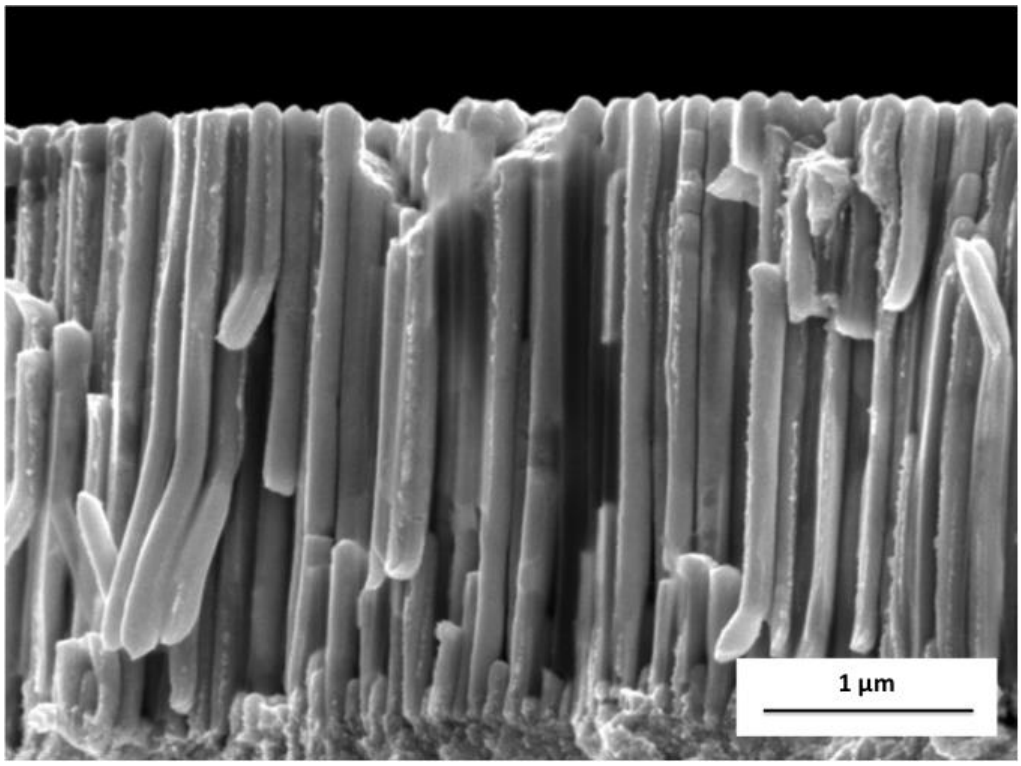

Figure 3.26 : Cross sectional image of the free-standing gold nanowire array.

Gold nanowire arrays with different aspect ratios have been fabricated in order to show the tunability of the template based synthesis technique. They will be presented in the following chapter.

Silver nanowires:

Electrodeposition of silver was realized in a typical two-electrode cell with 50 ml volume. The surface area of AAO templates was reduced to 1,5 x 1,5 cm^2 by masking with nail polish. The AAO templates were treated with the zincate solution prior to electrodeposition and washed twice with deionized water. A platinized titanium mesh was used as the counter electrode. A homemade silver cyanide solution was used. The current density was 2 A/dm^2.

Figure 3.27 represents the surface of the as fabricated Ag nanowire arrays. The inset in figure 3.28 shows that the average nanowire diameter is 121 nm. The surface of the array is again highly homogeneous with more than 66 % of the nanowires having a diameter distribution between 100 and 150 nm range as seen in the inset of figure 3 27. On the other hand as seen in the figure 3.29 the height of silver nanowires is between 700-800 nm.

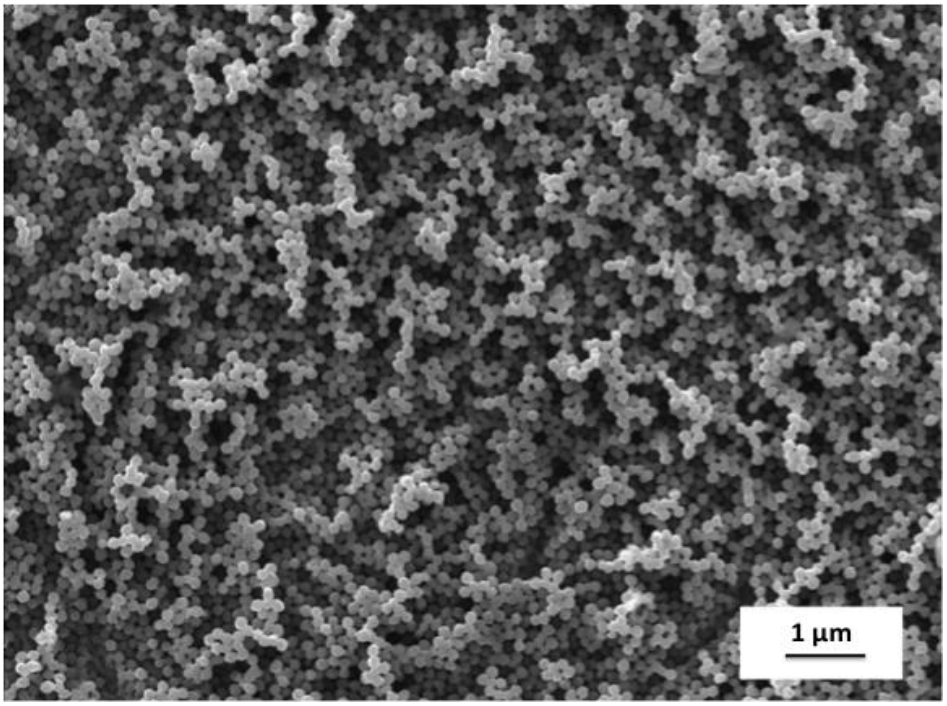

Figure 3.27 : General surface view of the free-standing silver nanowire array.

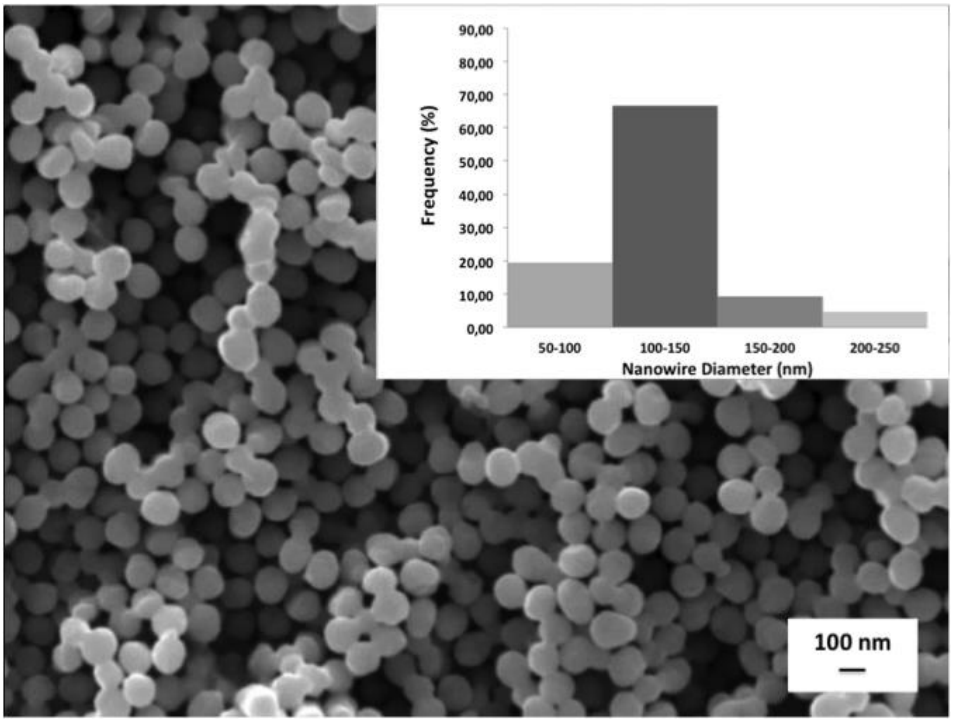

Figure 3.28 : Surface view and nanowire diameter size distribution of the silver nanowire array.

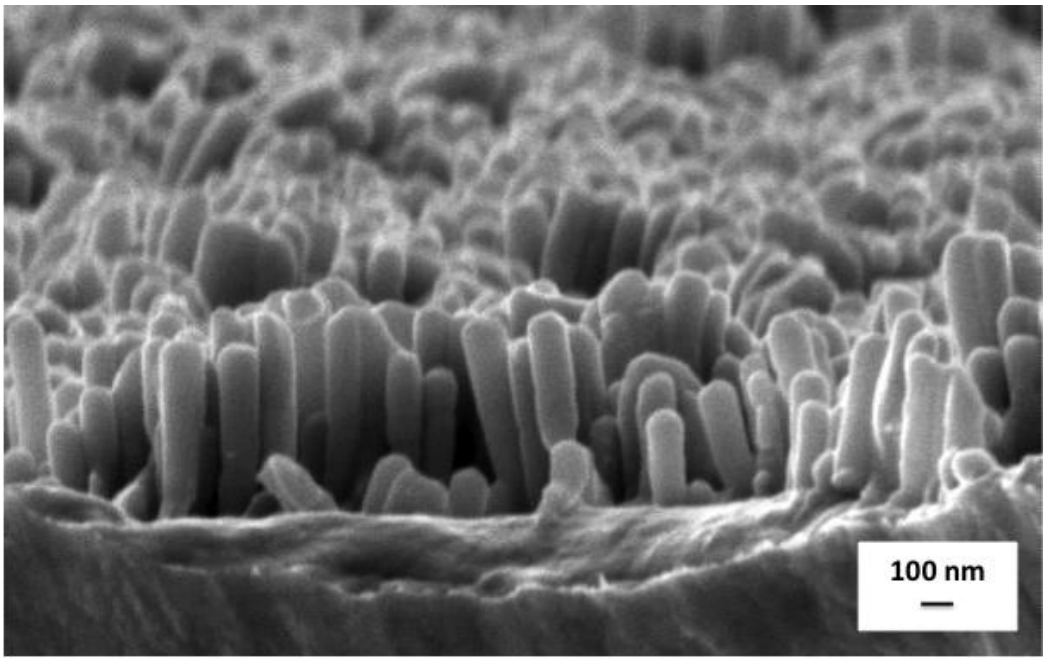

Figure 3.29 : Cross sectional image of the free-standing silver nanowire array.

3.5 Conclusions

The adaptation and optimization of the zincating technique for the DC electrodeposition of metallic compound on porous AAO templates have been done for the first time. Zincate treatment method for the activation of the pore bottoms has been optimized depending on immersion time and solution temperature. Moreover a second AAO template which has been subjected to a pre-barrier thinning method via voltage drop technique has also been analysed about the outcomes of the zincating method. Our results show that when the barrier thinning is applied before zincating treatment times can be reduced by 10 to 15 sec and the pore enlargement is 20 nm less than the AAO templates without barrier thinning. However the barrier thinning resulted in inhomogeneous pore bottom shapes, which may affect the shape of nanowires that will be subsequently deposited into the templates. Therefore it is not advised to use barrier thinning if the homogeneous arrays of nanowires are desired.

Zincating of AAO templates has proven to be an effective way to open pore bottoms and make the templates suitable for DC electrodeposition without any further treatment. It has been shown that zincate treated AAO is an ideal template for the fabrication of various metallic nanowire arrays. The technique is illustrated by fabricating nickel, gold and silver nanowire arrays. All of the three nanowire arrays

are freely standing on their base metal after the dissolution of the AAO template. They are all homogeneous in terms of length and pore diameter distribution (with approximately 70 % of all diameters for three different metals being between 100 - 150 nm)

In summary, zincate treatment for the removal of the insulating barrier layer has successfully been adapted to AAO templates. The optimization of zincate treatment time and temperature has been done to control critical AAO properties such as pore diameter. Moreover, the possibility to control AAO features such as pore diameter, interpore distance and pore length allows to tune the nanowire array characteristics as desired by further application requirements. This tuning of the final template features can easily be achieved by adjusting anodization parameters.

In the following chapter gold nanowire arrays produced via zincate treated AAO templates will be optimized and used as surface enhanced Raman spectroscopy substrates.

4. EVALUATION OF GOLD AND SILVER NANOWIRE ARRAYS AS SERS SUBSTRATES

4.1 Introduction

As mentioned in the first chapter for SERS to be possible two mechanisms, namely electromagnetic enhancement and chemical enhancement mechanisms have to be involved. Between those two, electromagnetic enhancement is the major contributing part to the total enhancement amount (Moskovits, 2005). Hence a good SERS substrate shall first of all cover the requirements necessary for EM enhancement to occur. As seen previously, the capital condition to support electromagnetic enhancement is to generate Plasmon resonances on the substrate's surface. Plasmon resonance circumstances depend on the choice of metal, its size and on the excitation wavelength. So it is safe to say that SERS enhancement is governed by template properties, such as particle size, interparticle spacing, and long-range order in addition to the excitation source's properties, which should be appropriate for the specific substrate.

Despite the extensive amount of work on SERS substrates in recent years, fabricating a substrate that combines high performance, reproducibility (both in terms of substrate properties and SERS results), tuning of the surface Plasmon resonance wavelength conditions according to the used excitation wavelength and ease of fabrication remains still a major challenge.

Conventional substrates (e.g. metal colloids, roughened electrode surfaces, etc.) may provide high enhancement however they almost all fail when it comes to reproducibility of the exact experimental conditions. Moreover, the random organization of these structures limits both tuning of the surface Plasmon wavelength and homogeneous distribution of results since for colloidal substrates uncontrolled aggregation remains a constant obstacle.

More sophisticated approaches to the reproducible and controlled substrate fabrication has been undertaken by many other groups. Techniques such as electron beam lithography (EBL) (Alexander & Wickenden, 2004) or focused ion beam lithography (FIB) (Sivashanmugan et al., 2013) have been successfully used in defining shape, size and pattern of the substrates. However those techniques are short off fabricating sub-10 nm gaps (which is crucial since SERS is a near field phenomenon hence the analyte molecules has to be in real proximity e.g. 1 to 5 nm of the nanostructure providing surface plasmons in order to be able to benefit from the enhancing mutual effect of the incident and scattered radiation fields) (Fusina et al., 2008). Moreover as mentioned again in the first chapter those techniques are extremely elaborate and time consuming especially if it is tried to obtain large areas of metal nanostructures.

4.2 Materials and Methods

For SERS studies Rhodamine 6G molecule was used as the probe molecule to evaluate the substrates. Rhodamine 6G is a chemical dye used as a tracer in various applications. It is highly photostable. The optical absorption spectrum and the molecular structure of the molecule are shown in Figure 4.1. The molecule's resonance excitation wavelength is between 520-550 cm^{-1}. The molecule has been studied extensively in many SERS studies and possesses well-characterized Raman bands (Pristinski et al., 2006).

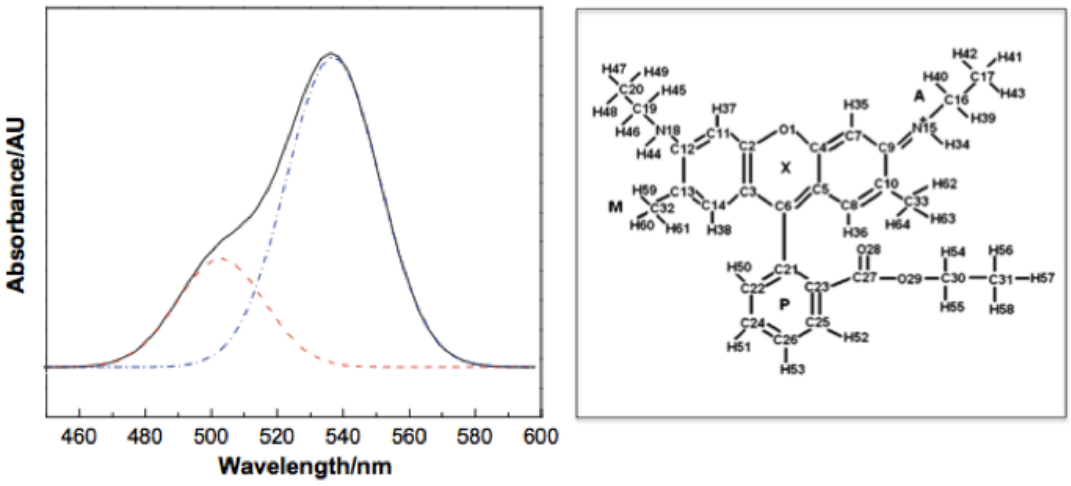

Figure 4.1 : Absorbance spectra and the molecular structure of Rhodamine 6G molecule (Saini et al., 2009).

The normal Raman and SERS spectra were recorded using two different Raman systems. The first setup is a micro Raman (Horiba Yvon Jobin, LABRAM HR) equipped with a He–Ne laser operating at 632.8 nm. The laser power on the sample was measured between 0.3 and 1 mW. An automatic *X*-*Y* stage was installed to move the samples. A holographic grating of 1800 g/mm was employed and 200 μm slit opening was chosen, resulting on a spectral resolution of approximately 1.2 cm^{-1}. Raman scattering was collected with a 180° backscattering geometry ensuring the same entrance and exit paths for both exciting and scattered light and hence reproducibility and high efficiency from the collected signal. A thermo-electric cooled multi-channel CCD camera (Andor iDus 420 series) with 26 x 26 μm pixel size was used to interpret the Raman signal. The second system was an inVia Renishaw Raman spectroscope attached to a Leica upright microscope equipped with 10X, 20X, 50X and 100X objectives. The system comprises 514 nm green and 632.8 nm visible lasers and high sensitivity ultra-low noise RenCam CCD detector. Raman scattering was collected again with a 180° backscattering geometry.

The ultraviolet-visible spectroscopy is used to measure the absorbance (and reflectance) spectra of the nanowire array between the ultraviolet and visible regions of the spectrum. The system measures first the reflectance of a reference material (a mirror) and then compares this to the reflectance of the sample.

4.3 Experimental

Au nanowire arrays are fabricated by using template based electrochemical method as described in chapter 3. To evaluate the effect of nanowire diameter size to the SERS results nanowires with different diameters and lengths are fabricated. In the second part nanowires with different aspect ratios are fabricated by modifying the AAO template formation parameters.

Electrodeposition of gold was done in a typical two-electrode cell with 50 ml volume. The surface area of AAO templates was reduced to 1,5 x 1,5 cm^2 by masking with nail polish. The AAO templates were treated with the zincate solution prior to electrodeposition and washed twice with deionized water. A platinized titanium mesh was used as the counter electrode. A commercial gold electroplating solution (Auruna 311) was used. The solution has a gold content of 2-4 gr/l and a

deposition rate up to 0.15 μm per minute. The pH of the solution is 0.6 and the maximum working temperature is 40°C. The working current density was 4 A/dm^2.

For determining the influence of the aspect ratio and the optimum free standing gold nanowire array characteristic, AAO templates are prepared under different conditions. The first step of anodization was the same for all experiments: 40 V anodization potential at 15°C during 1 hour. However the second step is slightly modified to obtain templates with different morphologies.

4.4 Results and discussion

The enhancement factor of SERS depends on the local surface Plasmon resonance conditions. This dependence is strongly linked to the geometry of the nanostructures in terms of excitation of surface plasmons. As explained in the previous chapters, metallic nanoparticles, limited by geometrical boundaries, can support localized surface Plasmon oscillations as opposed to flat surfaces, which sustain only propagating surface Plasmon polaritons (Aizpurura & Hillenbrand, 2012).

When Maxwell equations are solved for metallic nanoparticles with dimensions much smaller than the wavelength of the light, excited by an electromagnetic wave a strong absorption peak is immediately observed. This strong absorption is the result of dipolar Plasmon resonances occurring in the small spherical nanoparticle as the result of the in-phase movement of the conduction electrons in a limited geometry. This charge distribution across the particle causes a restoring force under a certain (resonance) frequency (Maiera & Atwater, 2005). Under this dipole resonance conditions, noble metallic nanoparticles show one strong absorption band (Figure 4.2) as an optical response.

This LSP resonance band is situated always in the visible region of the spectrum for noble metals. The Plasmon resonance frequency of metallic nanostructures is defined by their electric field distribution and it is differs according to the shape and size (Figure 4.3) (Wang & Shen, 2006).

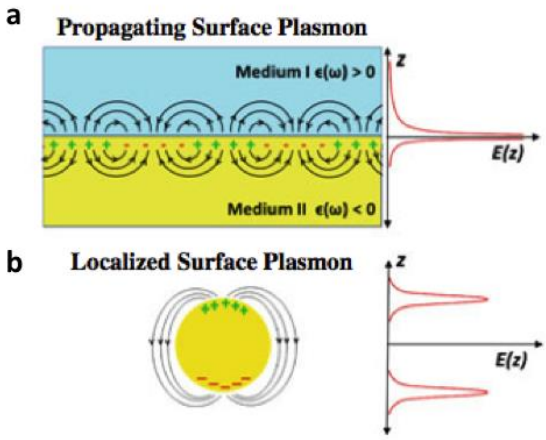

Figure 4.2 : Schematically explanation of a) propagating surface plasmons on a flat surface and b) localized dipolar surface plasmons on a noble metallic nanoparticle (Aizpurua, 2013).

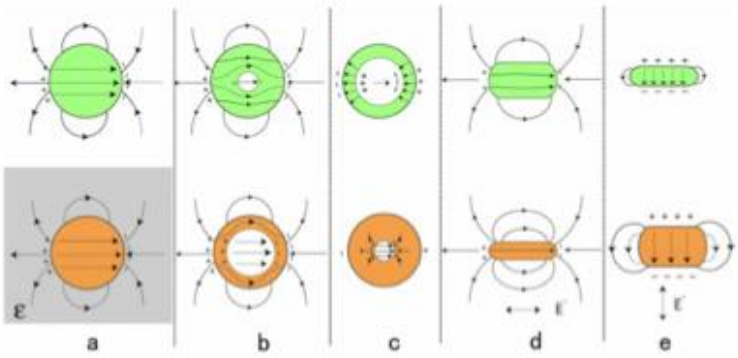

Figure 4.3 : Various nanostructure shapes with different the field distribution patterns, (a) metal sphere in a different medium, (b) metal nanoshell, (c) metal nanoshell presenting an asymmetric Plasmon mode, (d) metal nanorod under polarization parallel to rod axis (e) metal nanorod under polarization perpendicular to rod axis (Wang & Shen, 2006).

However the situation is different for elongated nanostructures such as nanorods and nanowires. The structural factors of nanowires or nanorods, such as longer and shorter axis lengths changes the Plasmon absorption behaviour completely and they should be carefully taken into consideration to determine the absorption wavelength of the surface plasmons (Jain et al., 2006).

When exited with incident light elongated nanostructures show two different local surface Plasmon resonance (LSPR) bands. This dual nature of LSPR band is due to the two different axis lengths of nanowires or nanorods. The first one is a short wavelength band called the *transverse band* and it is excited with the light is polarized along the short axis of the nanowire. The longer wavelength band is called

the *longitudinal Plasmon absorption band* and it is excited with electron oscillations occurring along the longer axis of the nanowires. The positions of the bands depend mainly on two geometrical factors being the aspect ratio and the particle size (El-Brolossy et al., 2008).

Under quasistatic limit (where the system is smaller than the wavelength of the electromagnetic field) the longitudinal band is red-shifted with increasing aspect ratio (Bryant et al., 2008). This red-shifting of the longitudinal LSPR band is due to retardation effects and radiation damping resulting from the involvement of higher order Plasmon modes taking place when the aspect ratio gets bigger. The transverse band shows also a slight red shift with increasing aspect ratio (El-Brolossy et al., 2008). On the other hand increased size (diameter) of nanowires cause the sharpness of the absorption peaks to be reduced due to the ununiform behaviour of the field across the larger particle. The broadening of the peaks is also a sign for multipolar excitations, which may take place due to retardation effects (Newhouse & Zhang, 2012).

To sum up, according to the literature, Raman enhancement results from dipolar order or multipolar order Plasmon resonances depending on the polarization direction of the exciting light and nanostructure geometry (Laurent et al., 2005). If the light is polarized perpendicularly to the nanowire axis only the dipolar Plasmon excitation is observed. But when the exciting light is polarised parallel to the wire axis several multipolar Plasmon bands can be also seen and the order of this multipolar Plasmon excitation depend on nanowire diameter size (Laurent et al., 2005). Hence by carefully tailoring design factors such as aspect ratio and nanowire diameter the nature of LSPR peaks and positions can be controlled and tuned according to the desired conditions.

4.4.1 UV-vis Absorbance characteristics of gold nanowire arrays

Figure 4.4 show the absorbance spectra of free standing gold nanowire arrays fabricated as described in the experimental section. The array consists of nanowires with 142 ± 11 nm diameters and 1100 nm length. The short wavelength LSPR band (transverse band) has an absorption maxima at approximately 450 nm whereas the longitudinal LSPR absorption maximum is placed slightly below 650 nm as expected. The broadening of the peaks is caused by radiation losses due to large

nanowire diameter size. The exact place of the longitudinal mode is strongly dependent on the aspect ratio and can be tuned according to the desired conditions.

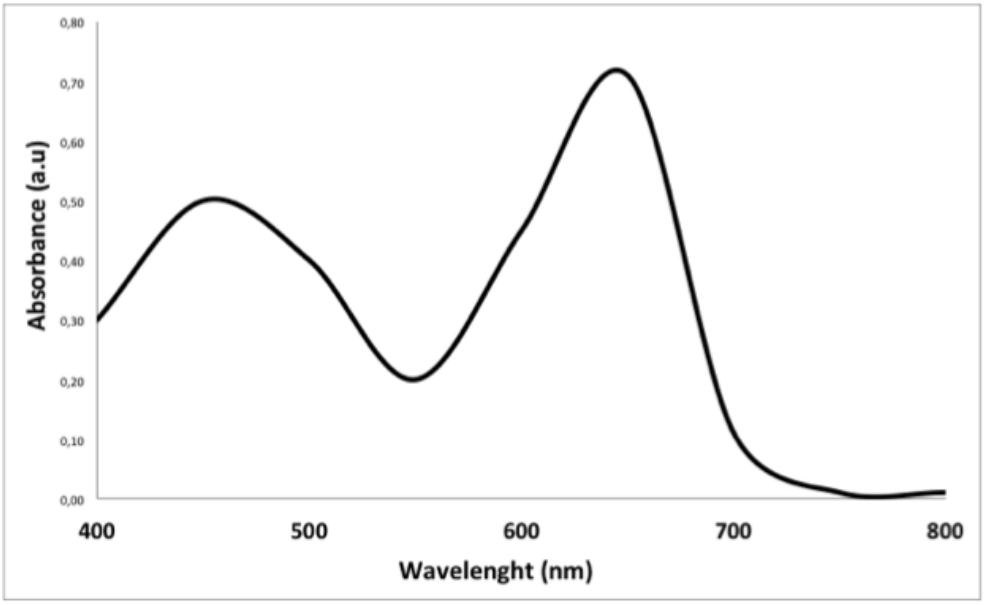

Figure 4.4 : UV-Vis spectrum of freestanding gold nanowire array.

Another important property that affects SERS response of the substrate is the interparticle distance. The interaction of the surface charge densities of two adjacent nanowires at the gap formed between them is very strong. This interaction results in a localised symmetric surface Plasmon mode formed by the hybridization of the single dipolar surface Plasmon resonances of each wire. As a result strong enhancements of the field are observed at these gap areas also called “hot-spots” in SERS literature. The hot-spot contribution to SERS being either very strong (in case of single molecule studies the enhancement can go up to 10^{14} fold) or moderate is very important and it is experimentally seen that arrays without gap structures does not give good SERS results even though the aspect ratio is in the desired range for Plasmon resonance (Moskovits, 2005).

One last point to take into consideration when talking about the LSPR of elongated nanostructures is the so-called optical nanoantenna effect or the lightening rod effect. The optical response of wire-like structures presents a strong anisotropy. The field is localised at the end of the wire and the response is tuned according to the aspect ratio.

In addition to being a function of nanowire length for different widths (radius), the optical antenna resonance (and hence the plasmonic response of a metallic nanowire) is also strongly dependent on the polarization axis of the incident light (Zhou et al., 2005, Tao et al., 2011, Etchegoin et al., 2006). To clarify this dependence two different polarization direction, namely longitudinal (s) and transverse (p) polarizations were monitored on freestanding gold nanowire array substrate (Figure 4.5). Characteristic R6G bands were observed for both polarization conditions. However it is clearly seen that when the electric field of the exciting light is perpendicular to the wire axis (which is the case of s polarization) the recorded spectrum is ~5 times stronger compared to the p polarization direction. Results are compared by curve fitting the 1360 cm^{-1} band and calculating its area.

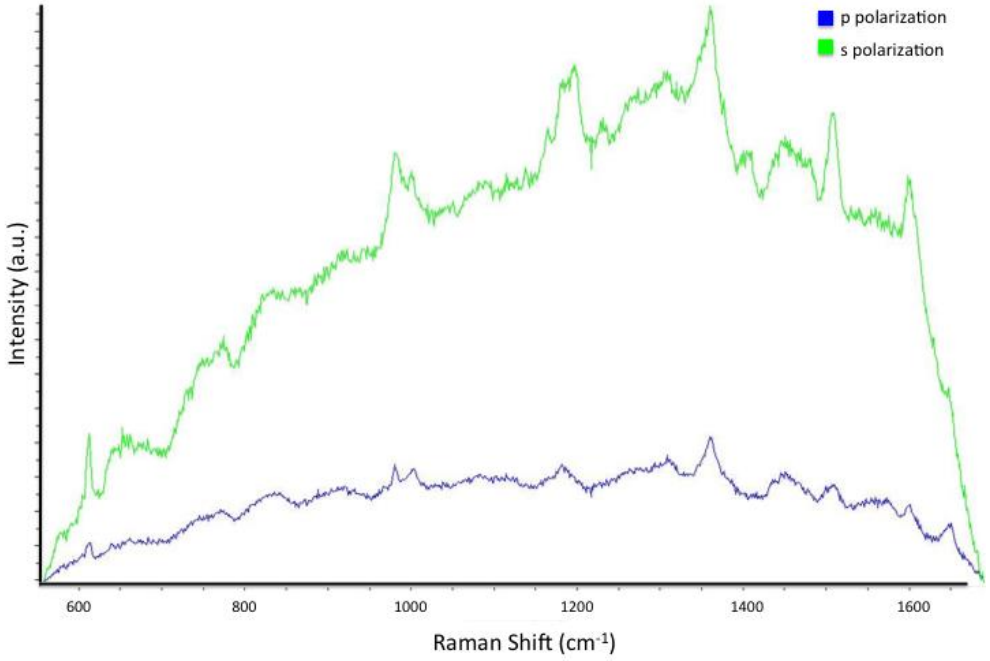

Figure 4.5 : Polarization dependence of the SERS spectrum of 10^{-4}M R6G.

4.4.2 Evaluation of the effect of the aspect ratio to the SERS properties

To observe the effect of the aspect ratio on the enhancement of the Raman signal, nanowire arrays with different aspect ratios are fabricated by modifying the template morphology through anodization parameters. The template morphology change also result in different inter-wire gap distances. The change in gap distances has a strong effect on the number and quality of the hot-spot forming areas.

The anodization conditions leading to various aspect ratios and inter-wire gap sizes are given in table 4.1.

Table 4.1 : Aspect ratio and interwire gap size variation according to anodization conditions.

Anodization Conditions		**Nanowire Array Properties**			
Potential	**Time (min)**	**Diameter (nm)**	**Length (nm)**	**Aspect Ratio**	**Gap Size (nm)**
70 V	2	133 ± 13	430	3.23	14 ± 3
70 V	5	142 ± 11	1100	7.74	15 ± 3
70 V	7	134 ± 9	1480	11	48 ± 11
60 V	5	116 ± 7	1008	8.68	38 ± 9
80 V	5	166 ± 13	1450	8.1	NA

The resulting aspect ratios range between 3 and 11. The gap size can be reduced down to 10 nm approximately and the maximum gap size is around 60 nm.

The wire diameter is only affected by the anodization potential. On the other hand the wire length is dominated by the anodization time. As a result slight modifications of potential and time lead to a wide range of aspect ratios on nanowire arrays. Figure 4.6 shows the surface and cross-section views of the nanowire arrays with different aspect ratios.

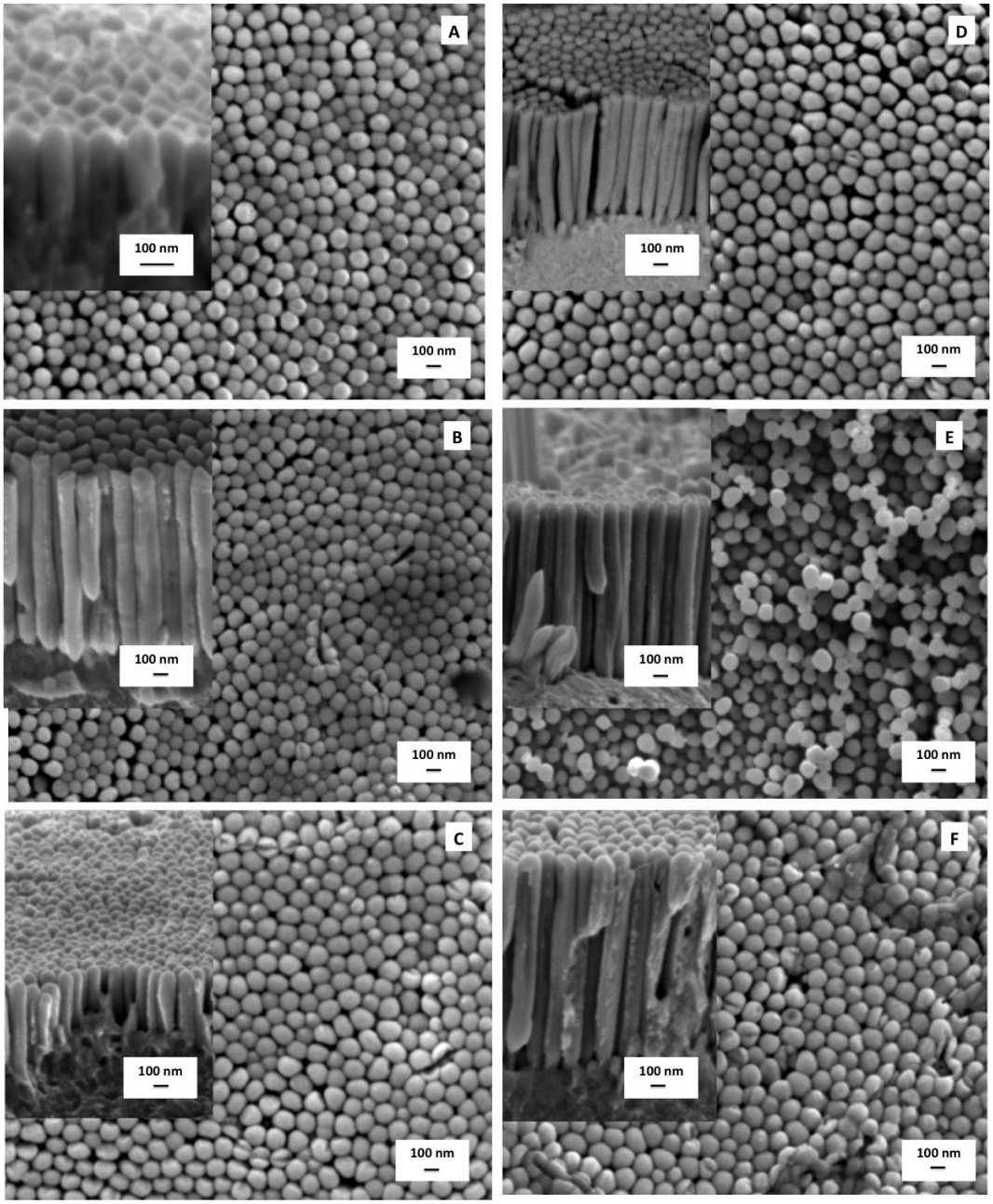

Figure 4.6 : Nanowire arrays fabricated through modification of AAO template preparation parameters. A) Array anodized at 60V for 2 min at the second anodization, B) Array anodized at 60V for 5 min at the second anodization, C) Array anodized at 70V for 2 min at the second anodization, D) Array anodized at 70V for 5 min at the second anodization, E) Array anodized at 70V for 7 min at the second anodization and F) Array anodized at 80V for 5 min at the second anodization.

The SERS measurements were performed by using Rhodamine 6G (R6G) as probe molecule. The main Raman and SERS peak positions of the R6G are given in table 4.2.

Table 4.2 : Raman and SERS positions of the main R6G peaks and their assignments according to the literature (Baia et al., 2005; Saini et al., 2009).

R6G Raman (cm^{-1})	R6G SERS (cm^{-1})
1655	1648
1605	1601
1584	1571
1448	1507
1403	1406
1337	1359
1288	1310
1206	1214
1173	1186
1031	1036
1002	981
851	
827	826
612	611

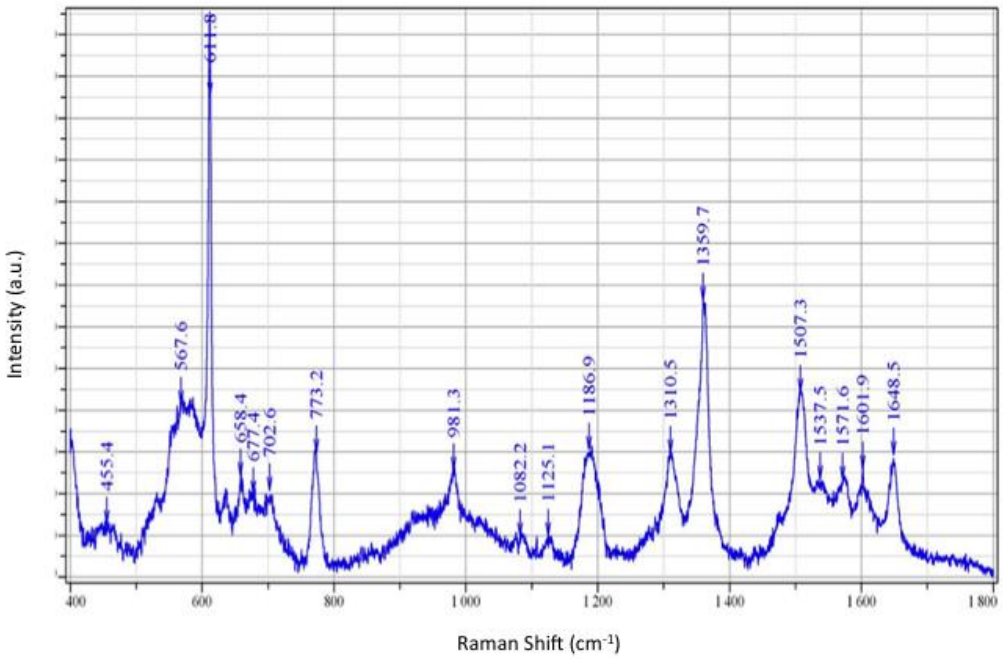

Figure 4.7 : SERS spectrum of 10^{-5}M R6G on gold nanowire array.

Rhodamine 6G displays its major bands in the 1200-1600 cm^{-1} region. The SERS intensity at 1507 cm^{-1} was compared among the nanowire arrays by recording the SERS spectrum of R6G on three different places on each substrate. The results are seen in Figure 4.8.

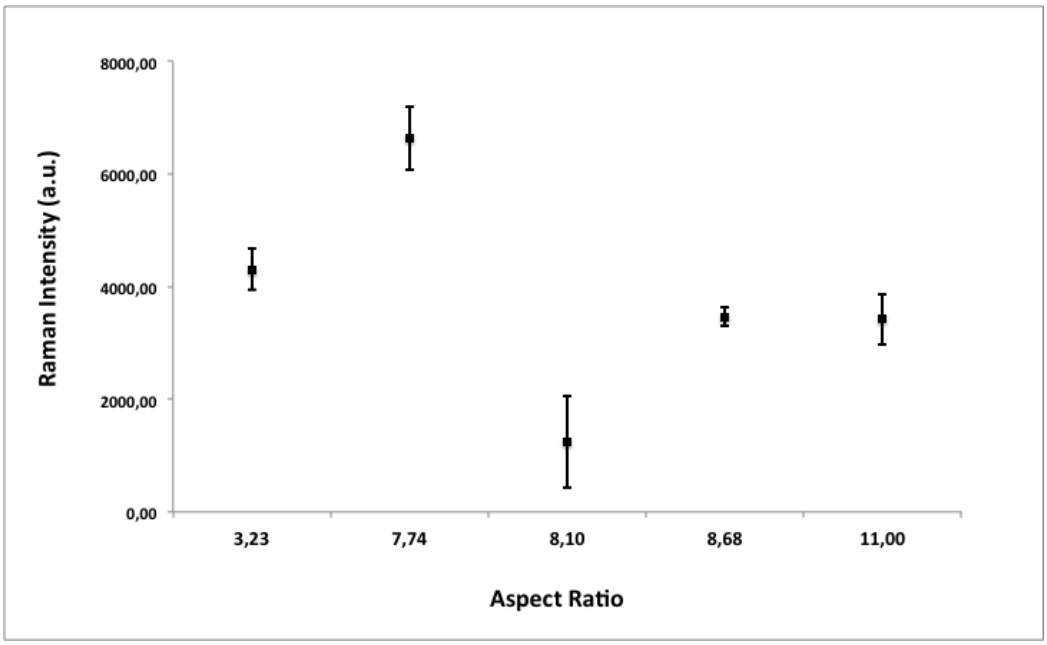

Figure 4.8 : Aspect ratio and Raman intensity relationship at 1505 cm^{-1}. Results averaged after 3-consequetive accumulations from different locations over the substrate.

As previously pointed out the strength of the SERS signal is influenced by two parameters (when all the others such as material choice, excitation signal, analyte molecule kind and concentration) are kept constant. Those are the aspect ratio and the gap size between two neighbouring nanowires. Figure 4.9 shows the unmodified SERS spectrum of R6G on all of the substrates. The relative intensities are obtained by curve fitting of the 1507 cm^{-1}. The intensity comparison is done by calculating the area of the 1507 cm^{-1} peak for all substrates.

When Figure 4.8 is closely inspected it is seen that the nanowire array with 7.74 aspect ratio (resulting from 70 V anodization for 5 min) gives the strongest Raman enhancement while the 8.1 (corresponding to 80 V anodization potential for 5 min) aspect ratio gives the weakest. It is also seen from table 3.1 that the gap size variation for 8.1 aspect ratio array is too irregular over the entire surface area hence an average inter-wire gap could not be determined. This situation is clearly causing a strong reduction of hot-spot forming occasions hence the resulting weakest SERS signal. On the other hand the average 15 ± 3 nm gap size of 7.74 aspect ratio array constitute an ideal distance for hot-spot formation. The quite similar gap size (14 ± 3 nm) of 3.23 aspect ratio array (corresponding to 70 V anodization potential for 2 min) also gives strong SERS signals however the reduced aspect ratio when compared to the strongest array is definitely causes it not being as strong as the best performing array.

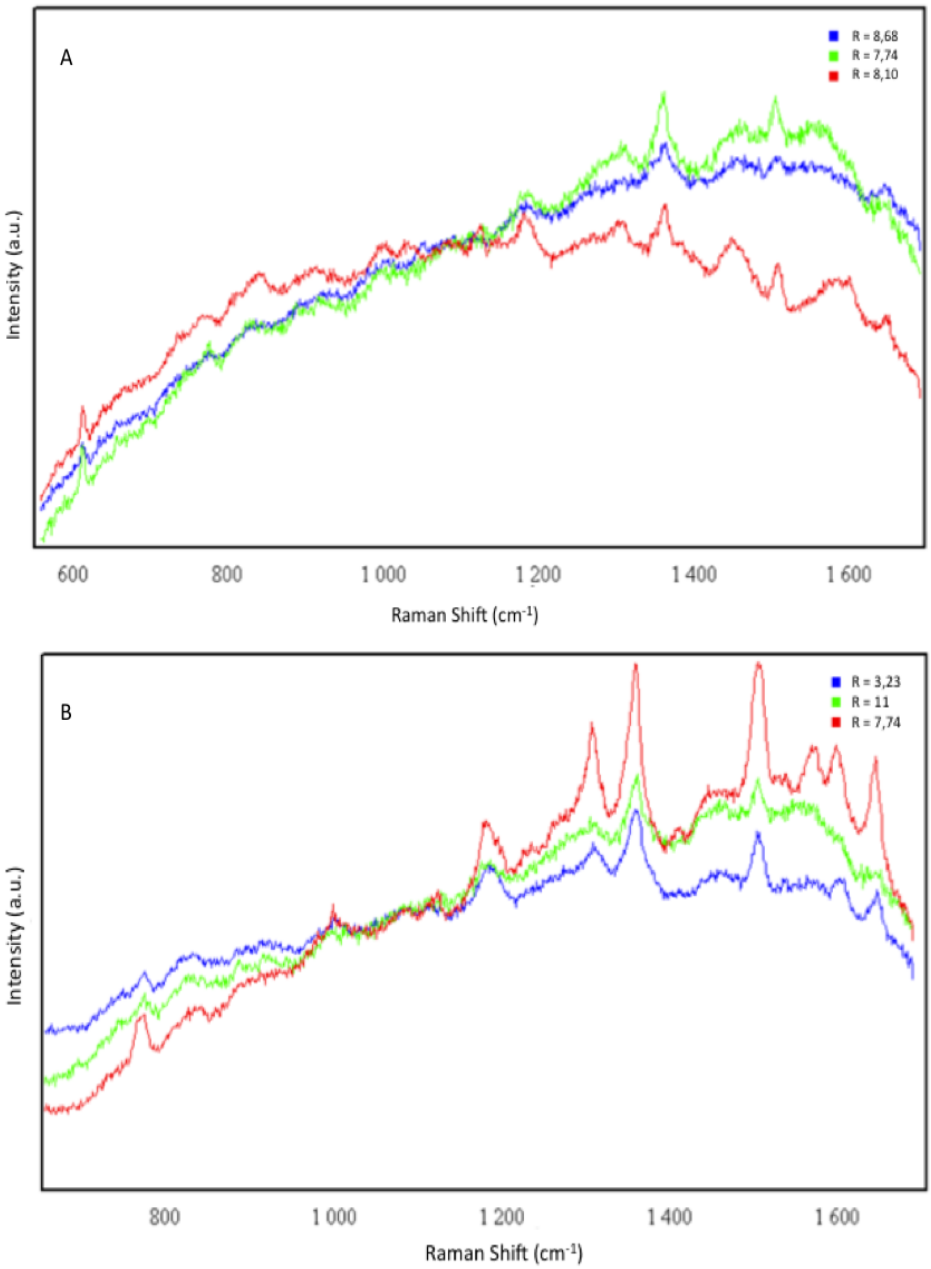

Figure 4.9 : SERS spectra of R6G on all substrates with different aspect ratios.

4.4.3 Evaluation of the reusability and the reproducibility of the Au nanowire substrates

The evaluation of one substrate to be reusable several times has been realized by using the same substrate three consecutive times after ethanol cleaning. The same concentration of Rhodamine 6G molecule has been used all three times. The results are given in the figure 4.10.

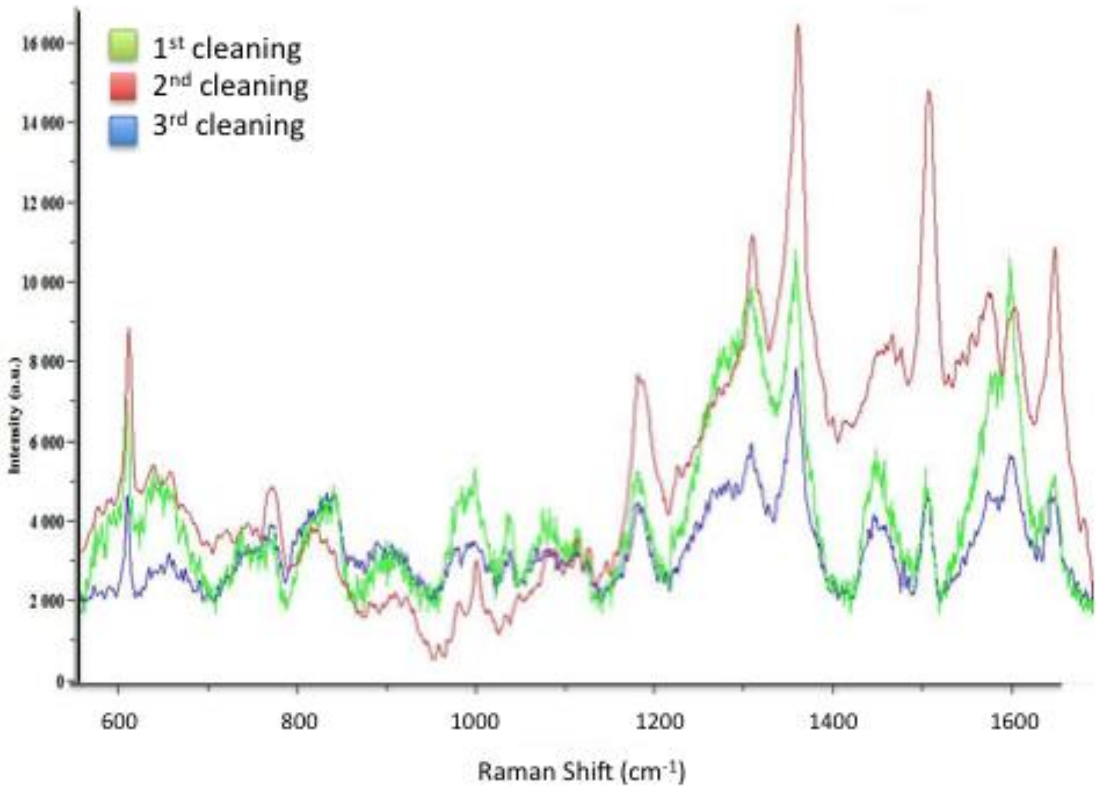

Figure 4.10 : Evaluation of the reusability of the substrates after three consecutive cleanings.

The reproducibility of the substrates have been measured by recording the SERS spectrum of 10^{-6} M R6G from both from three random points of the same substrate and by recording the spectrum on several different substrates produced under the same conditions. The substrate give each time the same spectrum, which was required to assess the reproducibity of the production technique. The results are shown in figure 4.11.

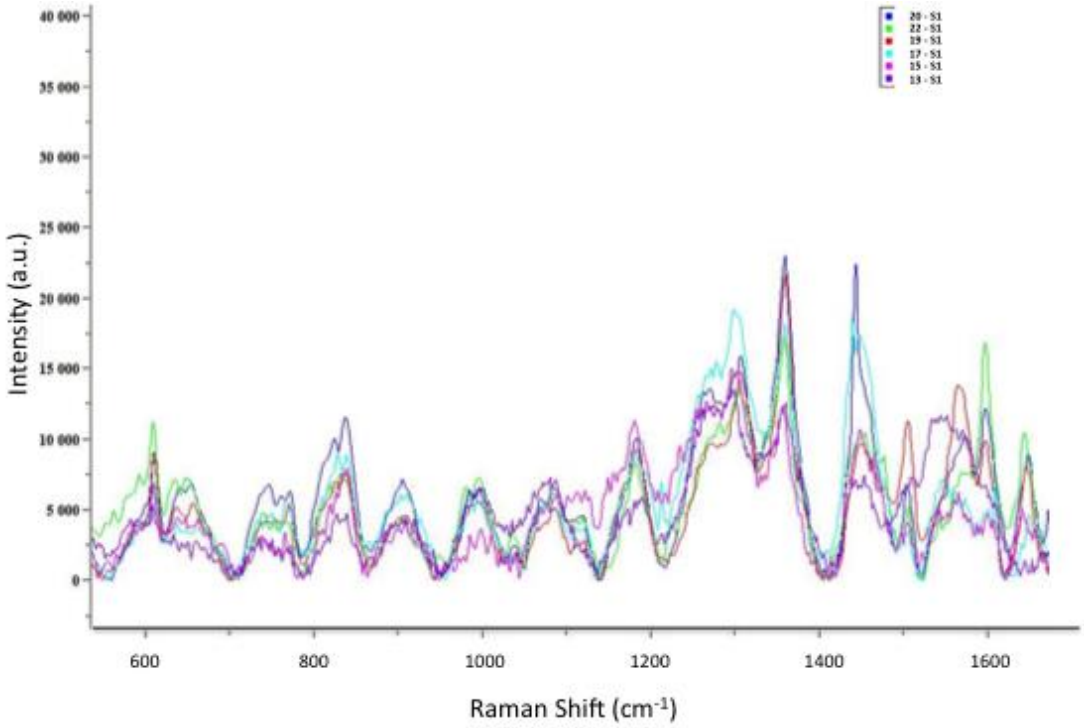

Figure 4.11 : Evaluation of the reproducibility of the results among different substrates produced under the same conditions.

4.4.4 SERS mapping of Au nanowire substrates

Raman mapping is done for the visualization of the enhancement distribution over the substrate. The strong enhancement of the Raman signal is seen throughout the bright red areas of the image. The darker parts show areas with weak signal intensity. Two of the highest intensity bands of the R6G spectrum (611 cm^{-1} and 1340 cm^{-1}) were selected for the mapping experiments. The mapped areas were chosen randomly over the substrate. Figure 4.12 shows the mapping for the 611 cm^{-1} band and 4.13 for the 1340 cm^{-1} band. It is seen from the mapping images that the enhancement distribution is almost homogeneous over the chosen areas of the substrate.

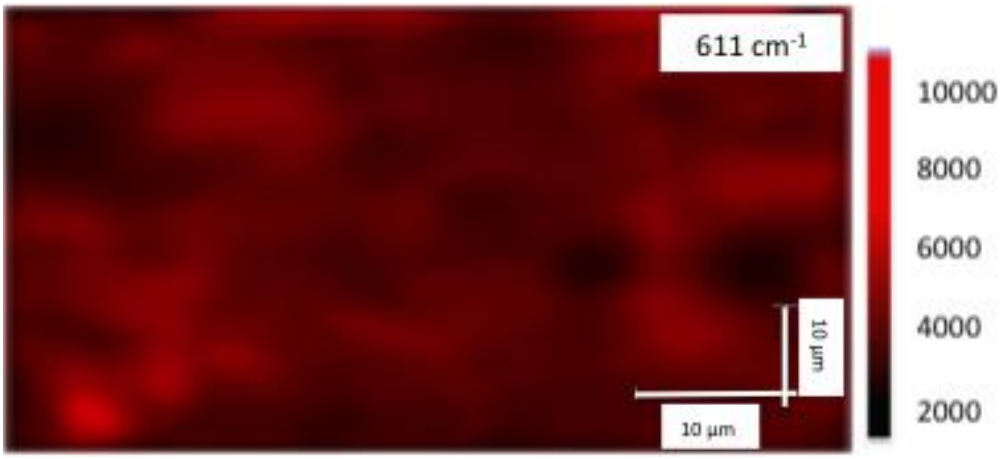

Figure 4.12 : Mapping image for the 611 cm^{-1} band of R6G.

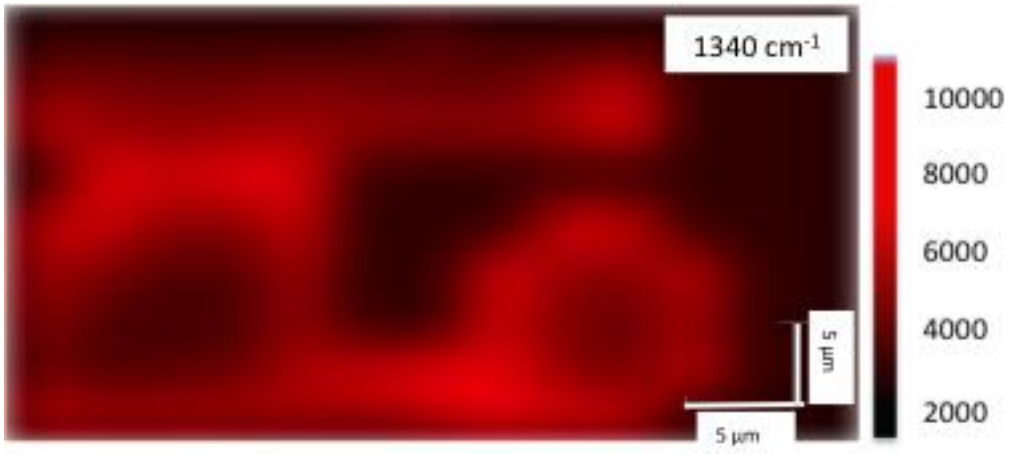

Figure 4.13 : Mapping image of the same region as in figure 4.10 for the 1340 cm^{-1} band of R6G.

4.5 Conclusions

In this chapter the SERS activity / efficiency of gold nanowire arrays are investigated with respect to their aspect ratio. The enhancement sensitivity of the freestanding gold nanowire arrays are optimized with respect to their aspect ratio by using rhodamine 6G as the probe molecule. The best performing aspect ratio was found to be 7.74 (with 140 nm pore nanowire diameter and 1100 nm length). The anodization conditions leading to this result was 40 V for 1 h at the first anodization step and 70 V for 5 min at the second anodization step. The results are also in agreement with experimentally obtained absorbance spectra, giving its transverse LSPR band around 650 nm. Therefore the nanowire aspect ratio (and diameter size and length) is in optimum ranges for an excitation wavelength of 632.5 nm. Moreover under these

conditions the small distance between two nanowires (15 ± 3 nm average gap size) are highly suitable for forming hot spots where Plasmon coupling between the nanowires occur.

In addition we have performed the Raman mapping studies of the best performing gold nanowire array and the results proved a highly homogeneous distribution of the enhancement capabilities for both 611 cm^{-1} and 1340 cm^{-1} bands of the R6G molecule.

Determining the anodization conditions leading to the optimum aspect ratio and inter-wire distance parameters in order to maximize the SERS signal may allow to tune the array properties according to the preferred excitation source wavelength in the future. This means that fabricating SERS substrates by the proposed technique results in large area, solid tunable and effective SERS substrates which are reusable several times. Moreover the substrate properties are homogeneous over the whole area, making the measurements much more reliable.

5. PROBING THE PROTEIN ORIENTATION ON FREE-STANDING GOLD NANOWIRE ARRAYS BY SERS

5.1 Introduction

This chapter will show the potential of our substrates as an ideal candidate for the SERS investigation of biological molecules (herein only proteins are used). The chapter is organized as follow: First a general introduction will be given on biological molecules and SERS studies. Then the substrate will be tested with a relatively large protein molecule: Bovine serum albumin (BSA). The adsorption of BSA to gold nanowire array and its stability will be investigated.

5.1.1 SERS and Biological Molecules

Despite the fast growing area of Nano biotechnology, understanding how biological building blocks such as proteins or even smaller molecules interact with technologically relevant substrates such as gold or silver remains still challenging. Especially revealing the mechanism of adsorption processes and characteristics of proteins to solid surfaces is of critical importance for designing and optimizing fast and effective nanobio-devices. There are several reasons for the lack of this knowledge. In most cases, observing protein interactions with solid surfaces is a hard task because proteins undergo structural changes upon adsorption causing them also to lose their functionality. Moreover traditional detection methods usually require a series of painful procedures of protein separation and purification and the use of sophisticated techniques such as x-ray crystallography and NMR spectroscopy. Those procedures are time-consuming and need relatively large amounts of samples but they yield to poor results making in turn them quite inefficient.

Over the last decade, once its main working principles were understood SERS became a popular tool for biomedical research communities. Particularly for protein studies, both in terms of characterization and orientation/functionality, SERS has

proven to be a valuable technique with its high sensitivity and selectivity. There are two aspects in which to say that SERS is one of the most promising tools for protein adsorption studies is not overstated. The first aspect comes from the nature of SERS process itself. Since the enhancement contribution to SERS by surface plasmons is a near-field effect the vibrational information of proteins can only come from the first few monolayers adsorbed on the surface. This eventually gives a strong opinion about the attachment mechanism of proteins to solid surfaces. The second aspect comes from the nature of SERS substrates. Albeit typical substrates in form of colloids or roughened metal surfaces of gold and silver are prone to agglomeration issues and local inhomogeneity, those noble metal substrates that have controlled geometry and stability are extremely good candidates for biosensing applications. Moreover the noble metals used for SERS, especially gold, is very attractive for biomedical applications of SERS due to its bio-chemical stability, biocompatibility and optical properties allowing limiting the fluorescence and minimizing the sample damage by choosing an appropriate illumination wavelength.

5.1.2 Background Information on BSA and on relevant SERS studies of proteins

Proteins are biological molecules composed of amino acids, which are formed, by a carboxyl group, amino group and a side chain. They have various functions within an organism and they form half of the dry mass of the cells (Stewart & Fredericks, 1999). Two or more amino acids may form peptide bonds, between the carboxyl group of one peptide and the amino group on another one, to form a polypeptide chain. Proteins are composed of polypeptide chains containing 50 or more peptides linked to each other by covalent peptide bonds to generate a proper and unique biological function. Proteins are referred by four distinct structures. The first one is called the primary structure and refers to the amino acid sequence only. The secondary structure is composed by a repetitive regular sequence referred by alpha helix and beta sheet turns. The tertiary structure is composed by the three dimensional conformation stabilized by salt bridges, hydrogen bonds and disulphide bonds. The quaternary structure is a polypeptide chain formed by several proteins that works as a protein complex.

To date a great amount of work has been undertaken by several groups to study protein structure and adsorption mechanisms on solid surfaces also by SERS. The

main SERS active substrates for protein studies involve colloidal solutions of gold and silver, protein mediated sandwich metallic films and metal island films generated by vacuum evaporation with an electron beam, although lithographically patterned nanostructures are also used (Han et al., 2009). The work on SERS of proteins typically fall into two major categories: 1) investigation of large proteins, containing either a labelling dye molecule or not and 2) investigation of individual amino acids or small peptide, dipeptide or polypeptide assemblies in order to characterize their spectra.

Stewart and Fredericks were one of the pioneers of peptide and protein SERS research. They obtained SERS spectra for a variety of small peptides and proteins and showed that they were adsorbed onto silver by the carboxyl terminus. They also presented that for small dipeptides the major bands on the spectra came from the side chains close to the carboxyl terminus (Stewart & Fredericks, 1999).

Natan group used cytochrome-c protein-colloidal gold and silver nanoparticle conjugates to study the stability and control of the protein orientation (Keating et al., 1998). Au nanoparticles were used to control the stability of the protein. The complex was subsequently adsorbed to citrate reduced Ag nanoparticles for better SERS efficiency.

Another widely studied example for large proteins by SERS include the investigation of hemoproteins such as hemoglobin, myoglobin (Tom et al., 2007, Etchegoin et al., 2003) and cytochrome *c* (Delfino et al., 2005). Those proteins are usually detected by using a resonant dye molecule covalently linked to the probes due to the complex and repetitive nature of the molecules. In this case, the obtained spectra reflect the spectrum of the dye molecule rather than the biomolecule itself, nevertheless proving the presence of the targeted biomolecule at the surface of the metallic SERS substrate (Pavel et al, 2008). For instance Delfino and co-workers studied cytochrome *c* in single molecule detection limits by SERS by immobilizing the protein on a glass slide and using a resonant excitation line. Although labelling or resonant excitation results in high sensitivity and selectivity, the process is rather complex and applications for high efficiency and rapid detecting are limited.

Podstawka et al. evaluated in 2005 the molecular structure and adsorption mechanisms of phosphonodipeptides by SERS, Raman and IR spectroscopy

techniques. Hereby, SERS is used to clarify the interaction mechanism and type of the peptides with silver colloidal solution under different conditions (Podstawka et al., 2005).

Label-free SERS detection of proteins has also been studied by several groups via different strategies. Han et al. (2008) demonstrated the label-free multi protein detection technique by using a technique based on protein electrophoresis named as "Western SERS". The technique combined protein separation with SERS for effective multi protein detection and used a silver staining method where colloidal silver was *stained* by using a nitrocellulose membrane containing the proteins to be analysed. The same group also showed later a different method consisting of a "protein-mediated sandwich strategy" consisting of placing the protein molecule between two different noble metallic layers (gold-protein-gold or gold-protein-silver) fabricated by layer-by-layer deposition and metal staining methods (Han et al., 2009). Pavel et al. worked on the label free detection of two small mutant proteins modified for acting as bifunctional linkers for silver nanoparticles (Pavel et al, 2008). By this way nanoparticles were brought closer via the linker protein to form hot-spots. The protein structure was detected from the gap formed between the aggregates forming the hot-spots at very low concentrations ($5x10^{-5}$M) under visible excitation line. Kahraman et al. followed the same strategy by using self-assembled protein-silver nanoparticle conjugates to detect proteins such as BSA, catalase, pepsin, cytochrome-c and lysozyme. However they took the SERS spectra from the Ag nanoparticle/protein assembled films on surfaces as thin films (Kahraman et al., 2010).

Small peptides and short proteins are much more easier to study with SERS whereas larger proteins have differential affinity and irregular adsorption problems. However one of the most extensively studied proteins in biomedical and bionanotechnology research is certainly bovine serum albumin (BSA) (Figure 5.1). Albumins are the most abundant plasma proteins in the circulatory system, responsible mainly to regulate the blood ph. BSA is a serum albumin protein purified from bovine blood with numerous applications. Its structure is globular with dimensions 4 nm x 4 nm x 14 nm and has 583 amino acids. The molecular weight is 66,5 kDa. The structure of BSA is extensively studied and very well known (Benjamin & Teale, 1978, Brahma et al., 2005, Michnik et al., 2005). Its native structure is a single polypeptide chain.

The tertiary structure is composed of three homologous domains, rich in alpha helix structure. Each homologous domain (I, II and III) is composed of 6 helices, cross-linked by 17 disulphide bonds and one free thiol at pH 5-7 (Iosin, et al. 2011; Han et al., 2008). The conformation is repeated in a series of nine loop-like structures positioned on the centre of eight cys-cys pairs (Ignat et al, 2010). The presence of two tryptophan residues gives BSA strong fluorescence properties (Iosin et al., 2009).

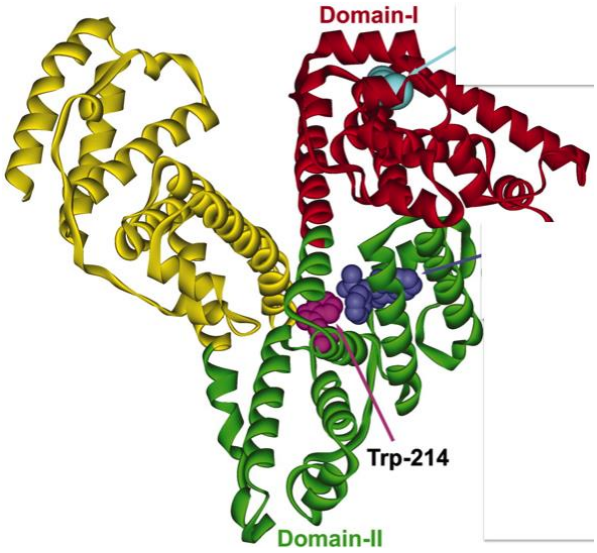

Figure 5.1 : Crystal structure of BSA showing three different domains and the main tryptophan residue (url-2).

Nakamura and co-workers investigated the conformational changes occurring on the disulphide bridges of the BSA after acid-induced isomerization by Raman spectroscopy (Nakamura et al., 1997). The principal work on SERS studies of BSA has been undertaken by Iosin group in two separate articles. The first one discusses the study of protein and various shapes of gold nanoparticle conjugates by fluorescence and surface enhanced Raman spectroscopy. The protein-gold conjugation has been verified by recording the modification of LSPR band positions in the absorbance spectra of gold nanoparticles. In this case SERS provided the information about the molecular groups responsible about the molecular groups forming the adsorption on gold structures (Iosin et al., 2009). The second study investigated the pH and thermally induced conformational changes of BSA once adsorbed to gold nanoparticles. The adsorption process and the structural changes occurring at different pH values are monitored by the shifts in SERS spectra. The results show that BSA undergoes structural changes in its secondary and tertiary

structure at different pH values and it is possible to follow these changes via SERS technique (Iosin et al., 2011).

So far almost all of the SERS studies involving protein structure characterization has been made in aqueous colloidal solutions of noble metallic nanoparticles via different strategies. Although they may give some good outcomes, reproducibility of the results and controlling the stability of the proteins remains still as considerable challenges. Moreover random adsorption of proteins to metallic particles and denaturation upon adsorption are major problems yet to be considered. This chapter explores this issue by two ways. First by showing that a solid SERS substrate can be successfully used in protein studies via employing a big robust protein (BSA) without labelling. The advantage of using a solid substrate with well-tailored properties overcomes the reproducibility issues. And second by discussing the binding mechanism and configuration of a small genetically engineered polypeptide (gold binding protein, (GBP)) on freestanding gold nanowire SERS substrate. Since the peptide is selectively binded to gold and its binding kinetics and properties are well studied (Donatan et al., 2012), random adsorption is no longer a problem and the adsorption sites at different pH values can ben speculated by SERS.

5.2 Materials and Methods

Free-standing gold nanowire arrays were prepared as described in the second chapter. Anodization parameters were kept constant for all experiments. The surface area of all substrates were 1 cm x 1cm.

Gold electrodeposition was realized from a commercial gold solution (Auruna 311). Electrodeposition parameters were the same as given in chapter 3.

The BSA solution was prepared by dissolving crystallized BSA (Sigma-Aldrich) in ultrapure water. The concentration of the stock solution was adjusted to 1 mg/ml and the pH 6, which corresponds to the native form of the protein.

Raman experiments were carried out on Renishaw InVia Raman spectroscope attached to a Leica DMLM upright microscope. A 50X objective was used to focus the laser on the nanohole array and to collect the scattered light from the sample surface. A 785 nm near- infrared laser line was used to irradiate the surface.

5.3 Experimental

Protein solutions were manually deposited using micropipettes on SERS substrates by 5 µl volume for each experiment. BSA solutions were analysed by using "drop coating deposition Raman" (DCDR) method (Ortiz et al., 2006). Raman spectra are recorded from the protein ring formed after deposition and evaporation. The depositions form circular spots of 1 to 5 mm diameter. The diameter of the formed spots depends on the concentration of protein solutions (Zhang e al., 2003).

Raman Spectra was acquired from two or more positions across the protein ring to check for evidence of impurities present in the deposits and accuracy and reproducibility of the results. Signal accumulation times of 30 to 120 seconds were used for all experiments.

5.4 Results and discussions

The DCDR method consists of dropping a protein solution onto the substrate directly and recording the Raman spectra after evaporation of the solution from the solid protein ring formed on the substrate. This method has proven to yield to a high quality Raman spectra even from ultra low concentrations of protein solutions (Zhang et al.,2006, Pinzaru et al., 2007). It has several benefits, which may be summarized as follow:

- The method is used to see protein structure changes and binding
- Proteins may undergo thermal damage under laser illumination, however the method avoids all sorts of thermal or photo damage
- It can be used in a wide concentration range, it is affected neither by the volume not the concentration of the protein solution.

Figure 5.2 shows the free-standing gold nanowire template morphology. The average nanowire diameter is calculated by using image J software (version 1.45) and found as 92 nm ± 9 nm (Figure 5.3). Visual investigations of the substrates upon protein solution deposition reveal that they are of hydrophilic nature. Although hydrophobic substrates are stated to give better results with the DCDR method they also causes denaturation of the proteins (Pinzaru et al., 2007). Since the purpose of SERS study of proteins is to understand the mechanisms involved in binding, denaturation must

be avoided. Therefore it is preferable to use a hydrophilic substrate. After deposition of the protein solution, an optimum concentration should be found to adjust the visibility of the ring structure. For BSA solutions two concentrations (1 mg/ml and 0.5 mg/ml) have been analysed by SERS. Figure 5.3 shows the Raman analysis of solid BSA and the corresponding band major assignments are given in table 5.1. The spectrum region (400-1700 cm^{-1}) is chosen because all of the fundamental information on protein and peptide structure falls into this interval (Thomas, 1999). Moreover the protein spectrum is recorded under nonresonant (off-resonance) excitation condition with 785 nm near infrared laser.

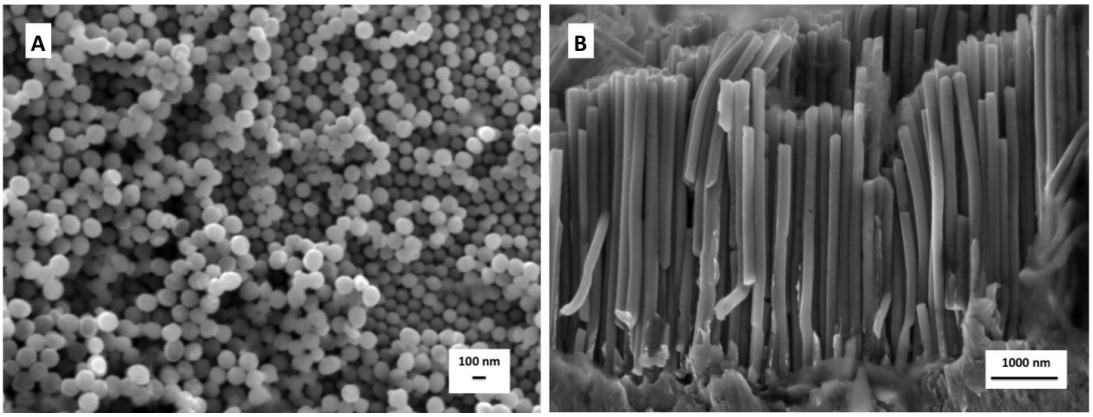

Figure 5.2 : Free-standing gold nanowire SERS substrate. A) The surface view, B) Cross-section view.

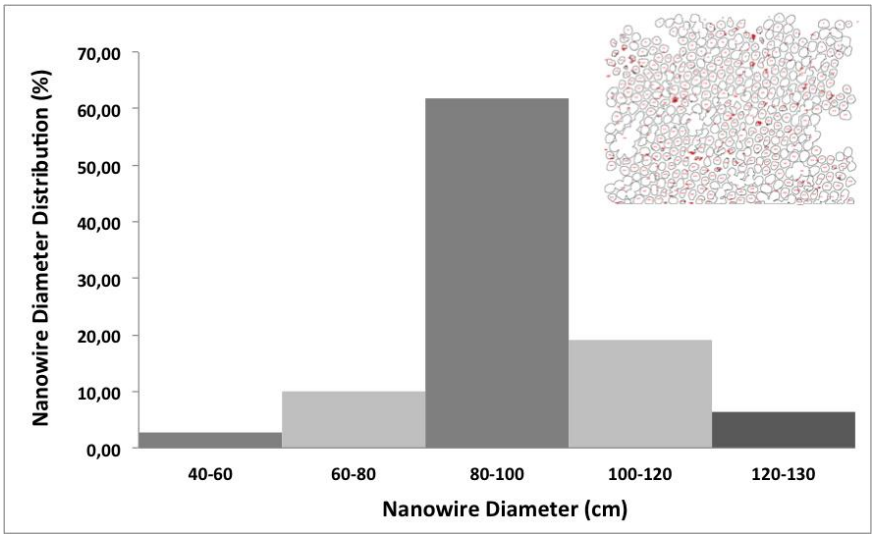

Figure 5.3 : Diameter distribution of freestanding gold nanowires.

Figure 5.4 shows the evaluation of the enhancement capacity of the freestanding gold nanowire substrate when compared to flat gold surface. The probe molecule was 10^{-5}

M R6G. The enhancement factor EF for the substrate was estimated using the following expression (Kahraman et al, 2010):

$$EF= (I_{SERS}.M_{Ads}) / (I_{RAMAN}.M_{Bulk}) \quad \textbf{(5.1)}$$

where I_{SERS} and I_{Raman} are intensities of a vibrational mode in SERS and Raman spectra. M_{bulk} is the concentration of analyte, used in the Raman measurements conducted on bulk samples, for our measurement 10^{-1} M. M_{ads} is the concentration of the analyte used for SERS activity measurement, which is 10^{-6} M R6G for this study. Using the intensity ratio of the vibrational mode at 1514 cm^{-1} and the molarity ratios (10^{-4}), the enhancement factor was calculated as 5 x 10^{6}. Since the measurements are non resonant at 632.8 nm laser wavelength for R6G and flat gold surface had no SERS activity, the enhancement of the Raman signal can only be attributed to the gold nanowires. The reproducibility of the results was confirmed via repeating experiments on the same substrate for at least three times.

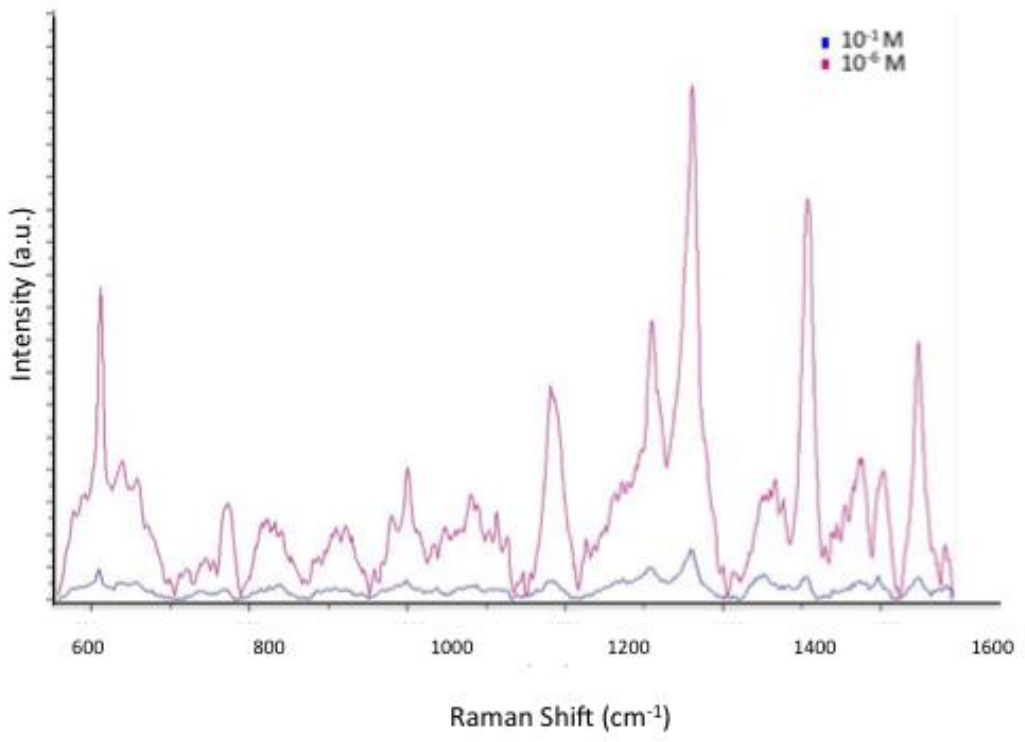

Figure 5.4 : SERS spectrum of 10^{-6}M Rhodamine 6G on gold nanowire array and 10^{-1} M Rhodamine 6G on flat gold surface.

Raman spectroscopy of proteins is governed more strongly by electron carrying groups, peptide main chains, aromatic side groups and sulphur containing side chains

due to the induced polarizability changes of these groups. For BSA, cystide disulphide stretching vibrations, amide I and amide III bands and skeletal stretching modes are characteristics of the Raman spectrum (Iosin et al., 2008). The most important feature in a protein's Raman spectrum is the place, shape and intensity of the amide I band. Amide I band characteristics reflects protein's secondary structure information. The band is seen in the 1550 - 1750 cm^{-1} spectral region. The strong peak of amide I band comes from C=O stretching mode along with C-N and N-H vibrational motion contributions. In the Raman spectrum of solid BSA amide I band is situated at 1656 cm^{-1} meaning that the structure is dominated by α-helices (whereas β-sheet peak would be seen towards 1680 cm^{-1} region) (Iosin et al., 2009). The characteristic of albumin structure is the 17-disulfide bridges present in the sequence located between two helical segments. The disulphide pairing Raman band for BSA is observed at ~510 cm^{-1} (in the Figure 5.5 It is marked as 506 cm^{-1}). This disulphide stretching vibration is closely related to the conformation (Nakamura et al., 1997). The Raman band seen at ~940 cm-1 (in the Figure above at 943 cm-1), occurring due to C-C stretching vibration is also a proof of the dominant α-helix structure of BSA. The amide III band is seen at 1325 cm^{-1} and it is due to the in-phase motions of NH bending and C-C stretching modes. The spectrum also shows several bands occurring due to $C-H_3$ and $C-H_2$ deformation vibrations coming from the side chains of different amino acids. Other bands and their assignments according to the literature data can be seen on table 5.1 (Iosin et al., 2009, Nakamura et al., 1997).

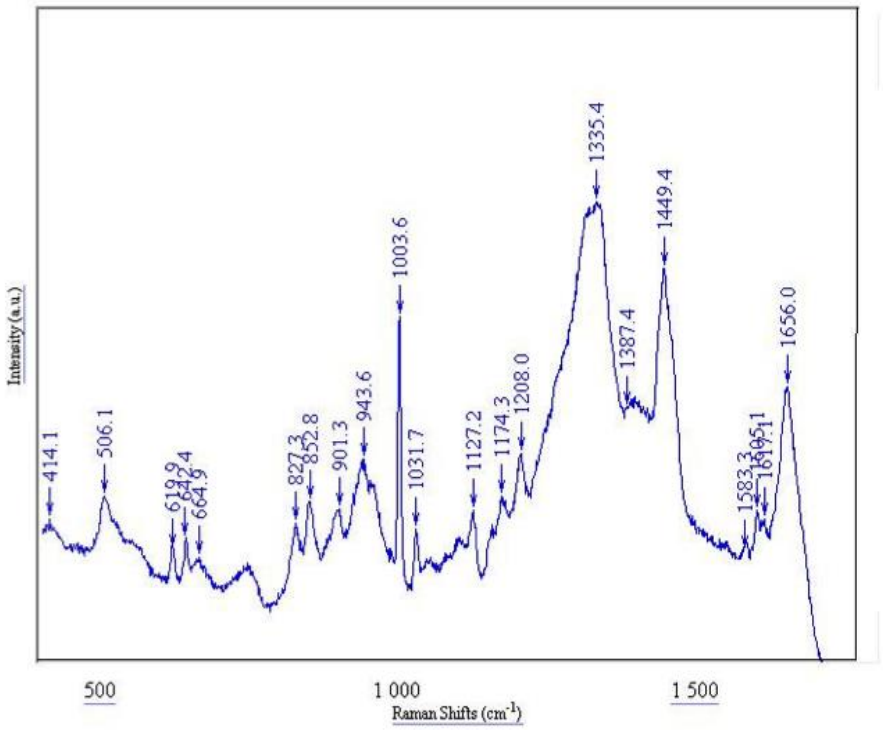

Figure 5.5 : Raman spectrum of solid BSA.

Table 5.1 : Band assignment of the Raman spectrum of solid BSA

Raman Shifts (cm^{-1})	**Band Assignments**
1656	alpha-helices Amide I
1583	Phe
1449	CH_2 and CH_3 vibrations
1403	symmetric vibration of the
1325	Amide III
1211	Tyr
1207	Phe
1033	Phe
1005	Phe
860	Tyr
827	Tyr

SERS measurements of 0.5 mg/mol BSA is presented in Figure 5.6. SERS spectrum is expected to enhance only portions of the molecule, which are in close proximity (1-2 nm) of the metallic structures. Hence several differences can be observed between the SERS and normal Raman spectrum of the molecule especially when a relatively big molecule such as BSA is studied. The most abundant amino acids in BSA are leucine, lysine, glutamic acid, alanine, aspartic acid, cysteine, threonine, valine, serine, proline and phenylalanine respectively. The whole amino acid content of BSA is given in table 5.2.

To accomplish the tentative peak assignments SERS spectrum of BSA has been background subtracted and peak positions are determined using LabSpec 5 software (Horiba Scientific) (Figure 5.6). Based on the literature data of Raman and SERS investigation of proteins and amino acids, the SERS bands of BSA have been tentatively assigned to individual amino acids (Table 5.3).

Table 5.2 : Amino acid content of BSA

Amino Acid	Letter Symbol	Kind	Number (except signal and propeptid sequences)
Leucine	L	aliphatic, hydrophobic	61
Lysine	K	positively charged	59
Glutamic Acid	E	negatively charged	58
Alanine	A	aliphatic, hydrophobic	47
Aspartic acid	D	negatively charged	41
Valine	V	aliphatic, hydrophobic	36
Cysteine	C	sulfur containig, uncharged	35
Threonine	T	alcoholic group, uncharged	33
Serine	S	alcoholic group, uncharged	28
Proline	P	aliphatic, hydrophobic	28
Phenylalanine	F	aromatic, hydrophobic	26
Arginine	R	basic, positively charged	23
Glutamine	Q	uncharged, containing COOH group	21
Tyrosine	Y	aromatic, hydrophobic	20
Glycine	G	aliphatic, hydrophobic	16
Histidine	H	basic, positively charged	16
Isoleucine	I	aliphatic, hydrophobic	14
Asparagine	N	basic, positively charged	14
Methionine	M	sulfur containig, uncharged	5

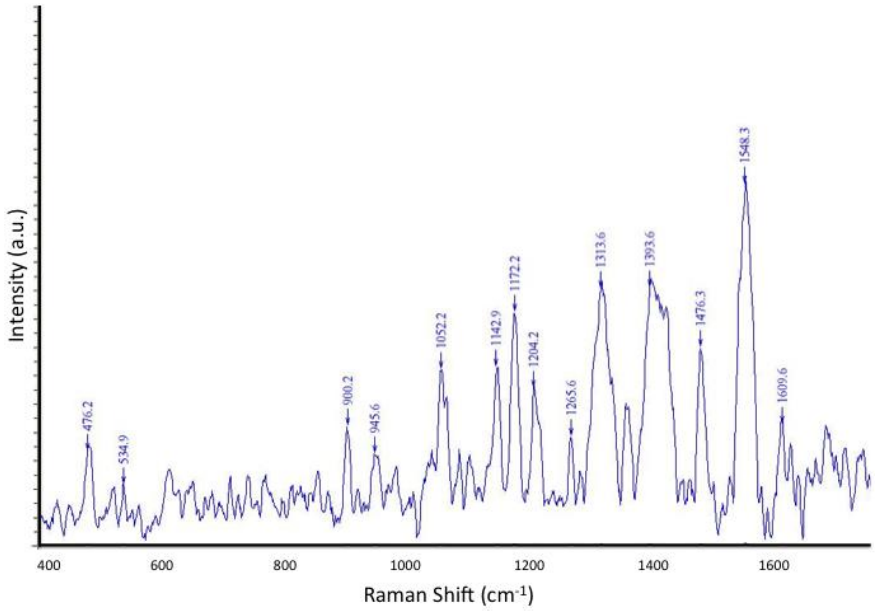

Figure 5.6 : SERS of 0.5 mg/ml BSA acquired on Au nanowire substrate.

Raw data of the SERS spectrum of BSA seen in Figure 5.7 shows the four main characteristics of protein vibrational spectra. The cystide disulphide vibration around 500 cm^{-1} is an indication that disulphide bonds are unbroken upon adsorption of the protein and the protein is not denaturated at room temperature when adsorbed to the metallic nanowires. The skeletal stretching, the amide III band and the amide I band are the other vibrational fingerprints of proteins.

According to SERS results it can be speculated that no (or very small) conformational change occurred in the BSA structure upon adsorption to the surface since the amide I band at position around 1600 cm^{-1}, the protein side chain deformation around 1400 cm^{-1} and the amide III band of the alpha helix structure at around 1200 cm^{-1} are clearly seen.

Strong signatures were identified coming from the following amino acids: leucine lysine and glutamic acid. This is not surprising since those are the most abundant amino acids in the BSA structure. On the other hand the strong bands situated around 600 cm^{-1} and 700 cm^{-1} let us strongly conclude that the sulphur atoms from methionine and especially cysteine are also involved in the adsorption mechanism.

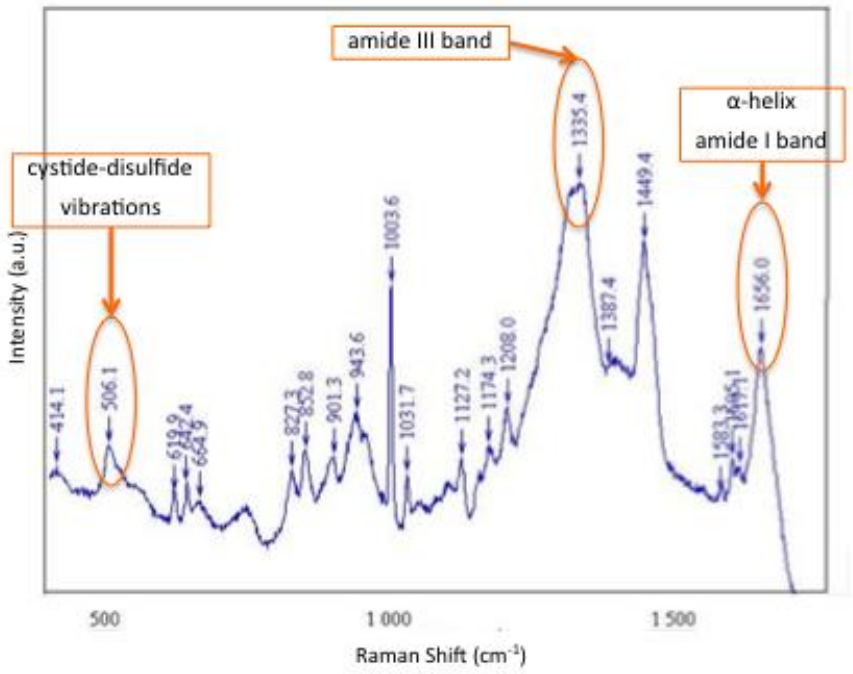

Figure 5.7 : SERS spectrum of 0.5 mg/ml BSA.

Table 5.3 : Tentative band assignments of BSA SERS bands.

Frequency (cm^{-1}) in BSA spectrum	**Tentative Assignment**	**Probable Amino Acids**	**Frequency (cm^{-1}) in reference spectrum**	**Frequency (cm^{-1}) in solid BSA spectrum**
478 (m)	vibrational frequency for S-S link	C	499	505
535 (w)	Rocking of CO^{2-}, skeletal deformation	V,**T**,I	542	530 (shoulder)
608 (w)	Bending of CO^{2-}	V		619
649 (w)	vibrational frequency for S-S link	M	645	642
709 (w)	C-S asymmetric stretching	M		
738 (w)		M	721	
767 (w)	CO2 deformation	**L**		
811 (w)	Out of plane CO_2 vibration	**L**		
851 (m)	skeletal stretching vibration for P, C-C-N	**Y**,**P**,S	831,843,854	
900 (m)	C-C and C-COOH stretch for G	P,**G**	921, 906	901

Table 5.3 (continued) : Tentative band assignments of BSA SERS bands.

Frequency (cm^{-1}) in BSA spectrum	**Tentative Assignment**	**Probable Amino Acids**	**Frequency (cm^{-1}) in reference spectrum**	**Frequency (cm^{-1}) in solid BSA spectrum**
979 (w)	C-C and C-N stretch for L, ring breathing vibrations for P,H twisting of the benzene ring for F	**L**,P,F	936,986	broad shoulder
1054 (m)	C-C stretch for K	**K**		1003
1150 (s)	Rocking of NH^{3+} unit, C-C stretch and NH_2 twist	**L**	1151	1127
1172 (s)	CN-NH_2 for Y	**Y**	1170	1174
1205 (m)	CH_2 Twist and rock for E	**E**	1213	1208
1264 (m)	Torsion of CH_2	**L**	1243	
1316 (s)	CH2 Twist and wagging for G,S,E,A	**G,S,E,A**	1300	
1352 (m)	C-H deformation and COO^- symmetric stretch for L, CH bending vibration for D	**L,D**	1338	1335
1475 (s)	COO- symmetric stretch for L and G, CH2 bending vibration for P, CH deformation for S	**L,G,K,P,S**	1447, 1453, 1468	1449
1550 (s)	C-C stretch and pyrole ring for V	**COO- symmetric stretch for L,**	1530	
1609 (m)	NH3 asymmetric bending for K, overlap of amide I band, NH2 shear	**K, all amino acids**	1609	
1679 (m)	Overlap of Amide-I band	**D, all amino acids**	1695	1656
1741 (m)	Overlap of Amide-I band	**All amino acids**		

5.5 Conclusions

In this chapter freestanding gold nanowire arrays are fabricated by tuning their structural properties according to give stronger enhancement when excited with 785 nm wavelength. The nanowire diameter is approximately 90 nm.

The enhancement factor of the substrates is again calculated by using rhodamine 6G as the probe molecule with 10^{-6} M concentration. The enhancement factor was calculated as 5 x 10-^{6} with 632.5 nm excitation source.

The SERS functionality of the substrates was tested with respect to a large biological molecule: BSA. The study of BSA on the substrates was realized under 785 nm wavelength excitement. The spectra showed unbroken cystide-disulphide vibration around 500 cm^{-1} suggesting strongly that no denaturation of the protein took place upon adsorption. Strong bands originating from lysine, leucine and glutamic acid were observed. This outcome was expected since those are the most abundant amino acids in the BSA structure.

Our results of the BSA study are in agreement with the literature data and show the usability of the substrates for the SERS investigation of biological molecules. The homogeneity of the enhancement all over the area, the reproducibility of the results and the robustness of the substrates make them ideal candidates for the study of small biological molecules and this topic will be further illustrated in the next chapter.

The next chapter will cover the SERS study of a small genetically engineered peptide (gold binding peptide) and its adsorption characteristics under different pH conditions via the interpretation of SERS results for the first time.

6. PROBING PROTEIN STRUCTURE AND ORIENTATION OF GOLD BINDING PEPTIDE (GBP) ON FREE-STANDING GOLD NANOWIRES BY SERS

6.1 Introduction

Up to this point we have characterized and showed the functionality of our SERS substrates produced by the novel template based preparation method introduced by our group. We believe that this substrate formed of freestanding gold nanowire arrays is highly suitable for protein adsorption studies at interfaces due to its robustness, ease of handling and homogeneous and well-defined geometry.

On the other hand using SERS to elucidate the adsorption characteristics of small peptides is relatively a new research topic. Previous works concerning SERS analysis of peptide orientation or adsorption were challenged by the lack of appropriate substrates. Inconsistent results were common both due to random adsorption of peptides to solid surfaces and to the unknowns (or inhomogeneities) of regular SERS substrates, such as colloids or electrochemically roughened surfaces.

We propose in this section to use our SERS substrate to monitored the adsorption behaviour of a small genetically engineered solid binding peptide by altering the solution charge at peptide-solid interface. The model peptide chosen for this study is gold binding peptide (GBP), which has been thoroughly characterized by several groups. Albeit the presence of excellent works on the adsorption mechanism of GBP to gold surface (So et al, 2009, Suzuki et al., 2007, Kulp et al., 2004, Donatan et al., 2012), to comment on the true nature of this interaction at charged interfaces is only possible via the merging of several techniques and we believe that SERS has outstanding prospects at this point.

In this chapter the adsorption behaviour of gold binding protein to freestanding gold nanowire array SERS substrate at charged interfaces will be investigated. The effect of the solution charge to the peptide adsorption will be monitored by alteration of the

solution pH. The pH values are determined with reference to pH 7.4, a neutral pH value where most of the GBP related research is performed. The other pH values are set in order to obtain 1) zero net surface charge, 2) a negative charge and 3) a positive charge on the peptide. The results will be evaluated with respect to the previous studies.

First a short background information on genetically engineered peptide for inorganics (GEPI's) will be given. Subsequently, gold binding peptides and the effect of the surface charge to the proteins will be introduced briefly.

6.1.1 Genetically engineered peptides for inorganics (GEPI's)

Molecular recognition is definitely amongst one of the most outstanding features of the Nature. Ordered and self-assembled structures are formed by this way one atom by atom at a time through self-assembly mechanisms to form bigger, functional macromolecular organizations. Almost every biological process from protein folding to energy synthesis relies on this simple yet elegant mechanism. The same mechanism takes also place between organics and inorganics. Hybrid architectures are formed as a result of bio mineralization processes such as bone, coral, pearl, woods etc. are frequently found in nature (Lehn, 1990; Tamerler&Sarıkaya, 2007; Sarıkaya et. al. 2003) through molecular recognition.

Mimicking natural conditions leading to bio mineralization and formation of hybrid bio-nanostructures between organics and inorganics is now of a great interest for materials scientists and biologists. Although bio mineralization is governed mainly by genetic control, specific morphology, size, shape and crystal structure factors are also crucially influential upon the final outcomes of the hybrid structures. Proteins, one of the key players of bio mineralization process, exhibit a central role for controlling several aspects such as nucleation, growth and mechanical and physical properties of the resulting structures (Tamerler et al., 2010). To lead the bio mineralization in a way to obtain previously designed, functional bio-nanostructures, genetically engineered proteins for inorganics, or GEPI's, have been constructed from isolated short peptides. GEPI's have the ability to interact exclusively via physico-chemical, non-covalent mechanisms with selected inorganic surfaces. Sarıkaya group, one of the pioneers of the GEPI research named this exciting new field as "molecular biomimetics". The philosophy behind the molecular biomimetic

approach is to design and build hybrid functional materials via bottom-up methods by mimicking biologic systems (Sarıkaya et al, 2003).

GEPI's are constructed of short amino acid sequences, involving usually 7 to 14 amino acids. They are selected by adapting traditional bicombinatorial approaches (cell surface display and phage display methods) to organic-inorganic systems. The first peptides obtained by this approach had specific affinity to Fe_2O_3 surface (Brown, 1992). Many other peptides with specificity towards various functional materials: semiconductors (Whaley et al., 2000), noble metals (Hnilova et al., 2008), minerals (Gungormus et al., 2008), mica (Donatan et al., 2009) and polymers (Kenan et al., 2006), etc. have been selected and characterized thereafter. The details of the selection methods are given thoroughly in several papers and it is not handled in this dissertation (Sarıkaya et al., 2004, Baneyx and Schwartz, 2007, Evans et al., 2008).

After the selection of a GEPI, its selectivity (and/or affinity) towards a specific inorganic is governed by the adsorption/recognition strength and mechanism (Tamerler et al., 2006). Despite the extensive amount of work on GEPI's, elucidating thoroughly the organic-inorganic interaction mechanism, which defines the nature of the relationship between solid binding peptides and inorganics remains still today a challenging subject. Before going to the details of this problem a specific GEPI, gold binding peptide will be introduced.

6.1.2 Gold binding peptides (GBPs)

Gold, with its biological inertness, high conductivity and plasmonic character is definitely one of the most important materials for bionanotechnology. This is why it was also one of the first metals that provoked an interest for peptide based biomimetic architectures. The first gold bind peptide sequence (GBP_1) was obtained by Brown in 1997. The sequence has been selected from a cell surface display library by using an outer membrane protein, carrying a random genetic sequence, linked to alkaline phosphatase (Brown, 1997). The GBP_1 is used in this dissertation in its triple repeated form therefore will only be noted as 3rGBP and will be shortly reviewed here. Detailed information can be found elsewhere (Brown, 1997, Tamerler et al., 2006).

The amino acid sequence of GBP is MHGKTQATSGTIQS. The same sequence is repeated three times to increase the binding affinity and strength. They recognize and bind to gold surfaces under high salt concentration conditions where proteins usually do not bind to the surfaces (Braun et al., 2002). The adsorption mechanism of GBP to gold surface is not governed by conventional chemisorption systems such as thiol-gold linkages. This assumption is validated by the fact that the sequence is cysteine free (cysteine is known to be responsible to make a covalent bond with the gold surface through Au-thiol linkage).

This GBP sequence defined by Brown (1997) remains still today as one of the most abundantly used one although many research groups continued to work on GBP variations (Hnilova et al. 2008, Peelle et al., 2005). Once this sequence was determined, understanding the binding mechanism and configuration of GBP on the gold surface has triggered the interest among several groups. The first work published on the subject came form Braun et al. in 2002. This work brought a deep insight about the structure of GBP by using statistical sequence alignment methods and molecular dynamics on different gold surfaces. Their results indicated that 3rGBP has an anti-parallel beta-sheet structure with repetitive random coils and extended structure. The adsorption was found to be governed by the periodic hydroxyl groups on the peptide's surface. They also showed that the {111} Au lattice was more favourable for protein adsorption than the {211} lattice (Figure 6.1). This was interpreted with relation to the higher atomic density of the {111} surface and the presence of trapped water on the surface corrugations of {211} lattice interrupting the interaction of the protein with the surface. Although there are equal number of polar and hydrophobic side chains in GBP it can be seen from Figure 6.1 that the amino acids from the polar side chains are the ones that are in close contact with the gold surface according to the molecular dynamic calculations (Braun et al., 2002).

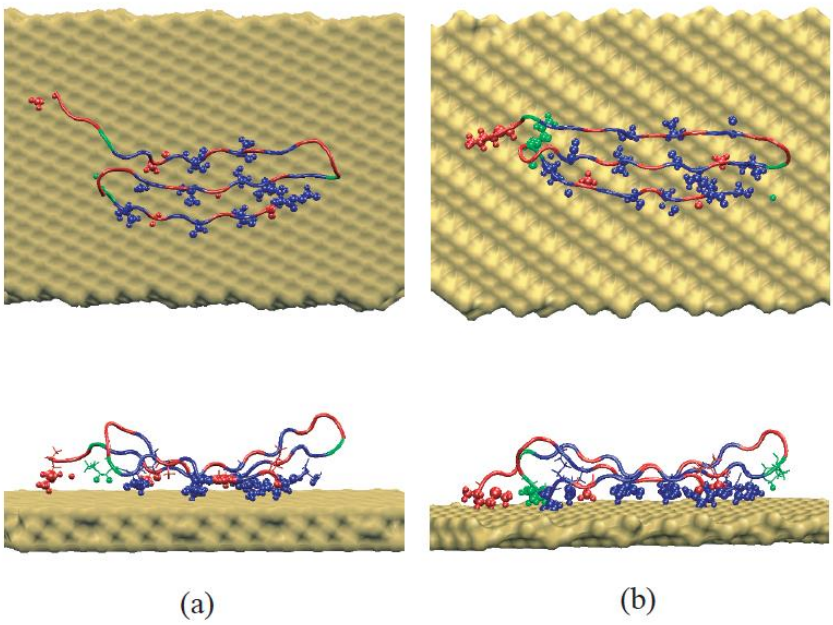

Figure 6.1 : The positionment of GBP on a) (111) gold surface and b) (211) gold surface. Blue residues are polar, green represents charged residues and red residues are the hydrophobic ones (adapted from Braun et al., 2002).

Another study realized by Sarıkaya and Evans groups came upon with three important outcomes about 3rGBP. First, they stated that 3rGBP had an unfolded, unstable conformation in the presence of Au^{3+} ions in solution. According to the NMR studies they showed that the interaction of the peptide with the Au^{3+} ions was made through the –KTQATS- motif (Kulp et al, 2004). And third they postulated that 3rGBP interacted with Au^{3+} ions in its labile, unfolded conformational state. SPR and QCM studies realized by Tamerler group pointed out to two coinciding adsorption reactions (with two different adsorption equilibrium constants) on the gold surface with up to 90% surface coverage in 20 min over a large pH range (Sarıkaya et al., 2004). Several other studies also compared and evaluated the gold surface affinity and selectivity of GBP (Tamerler et al., 2006, Suzuki et al., 2007). The self-assembly properties of the GBP has been also demonstrated by Sarıkaya group (So et al., 2009) via atomic force microscopy. The results of this study show that the adsorption process of GBP to gold surface takes place in two successive steps, first the formation of small independent island-like structures upon adsorption and second the coalescence of those islands accompanied by some structural changes on the peptide structure to form a peptide network respectively. This specific outcome also proves that the peptide is mobile and intermolecular interactions are dynamically happening on the surface.

In a follow-up study So et al. predicted the geometric reconstruction of the peptide on gold surface in 2009 by atomic force microscopy (AFM). The results of this work's findings indicate that 3rGBP is eventually formed of alternating coil-extended-strand structure and is intrinsically disordered because of its labile unfolded conformation. This coil or loop-like structure opens the way to surface-peptide interaction via alternating anionic (glutamine, serine, threonine) and cationic (histidine, lysine) residues among with complementary interactions with neighbouring GBP molecules. Moreover due to the lack of internal folding (or stabilization) by side-chain interactions, the peptide sequence is almost entirely in contact with Au surface, which may result also in intermolecular associations. A schematic representation of gold surface-3rGBP interaction is given in Figure 6.2.

To sum up the conformation of 3rGBP is intrinsically disordered and labile hence it undergoes conformational changes once in contact with the gold surface (Kulp et al., 2004). However 3rGBP do not loos its functionality in the unfolded form and this is one of the main properties of peptides involved in bio mineralization and molecular recognition processes (Evans, 2003).

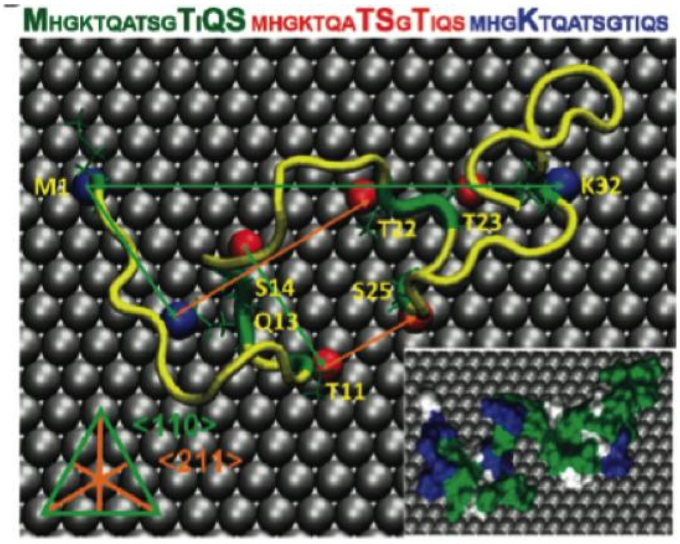

Figure 6.2 : Representation of the predicted geometric orientation of 3rGBP1 on the Au{111} surface. The inset shows surface representation of potential inter-molecular interactions with 3rGBP1 while bound to Au{111}, highlighting free polar (green), nonpolar (white), and cationic (blue) surfaces. The polypeptide backbone is represented in ribbon format (yellow) with docking residues (M1, T11, Q13, S14, T22, S23, T25, and K32, identified along the sequence shown on the top of the figure) (adapted from So et al., 2009).

Analysing the adsorption process of peptides at solid-liquid interfaces represents today still a great challenge. Imaging techniques such as AFM (So et al., 2009, Gettens et al., 2005), electrochemical methods such as cyclic voltammetry and electrochemical impedance spectroscopy (Ding et al, 2007), and kinetic measurement methods such as QCM (Donatan et al., 2012) are used to measure adsorption kinetics and thermodynamics. However, SERS as a simple spectroscopic method can give both compositional and structural information and can guide about commenting about the portions of the peptide playing a key role on adsorption process (Sengupta et al., 2008).

6.1.3 Protein behaviour at solid liquid interfaces

Since GBP adsorption properties are discussed in this dissertation, a short background information on the protein behaviour at solid liquid interfaces will be given thereafter. Proteins are intrinsically surface-active molecules because of their two main intrinsic properties. As mentioned earlier in the previous chapter, proteins are formed through the random association of 20 different amino acids. The amino acids in a protein sequence are linked together by their amino/carboxyl ends. As a result each protein chain is left at both ends with a de/protonated amino (NH_3^+) or carboxyl (COO^-) terminus. For this reason they have zwitterionic character according to different pH values (Figure 6.3). Moreover a single protein chain may contain both polar amino acids (which behave as hydrophilic molecules in water) and non-polar residues (which behave as hydrophobic molecules in water) giving to the whole chain an amphiphilic character (Israelachvili, 1992). These charged and polar groups also maintain the structural stability of proteins. For instance hydrogen bonding referred as salt-bridge is formed between two charged residues that are so close to each other that a water molecule cannot be trapped among them.

The net charge of a protein molecule is determined by the ionization constants of the carboxyl and amino ends and the pH of the solution. Non-polar residues, found usually in the interior parts of the molecule in aqueous environments, are responsible for the folding of the protein chain. The specific location of polar residues in the periphery of a protein and non-polar residues in the interior parts is what causes the formation of alpha helices and beta sheets by stabilizing the protein backbone through hydrogen bonds.

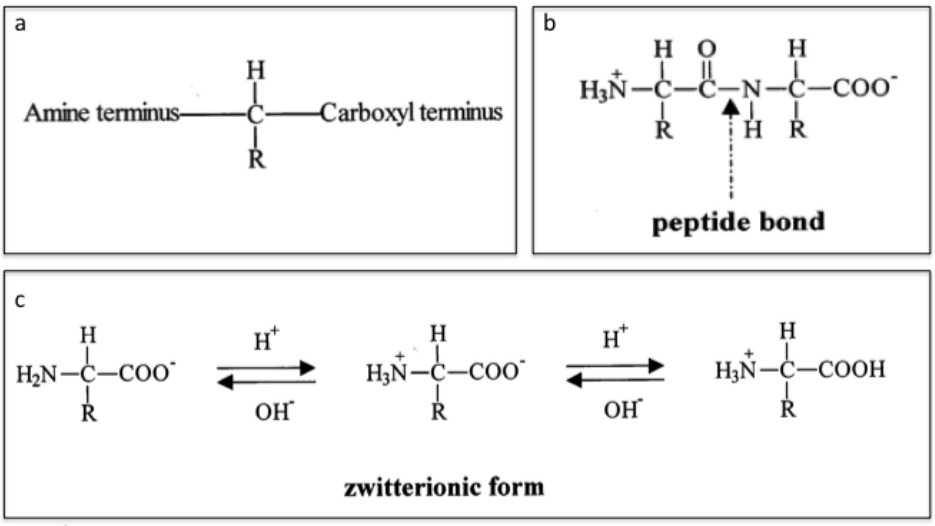

Figure 6.3 : Representation of the amino acid structure, R represents the side chain (a) formation of a covalent peptide bond to form a dipeptide (b) Zwitterionic state formed through ionization of amino acids (c) (Adapted from Stewarts and Fredericks, 1999).

The configuration of the protein backbone is called "the secondary structure" and is named according to the set of dihedral angles (ϕ,φ). The α-helix structure is formed when $\phi \approx -60°$ and $\phi \approx -45°$ and β-sheet is formed when $\phi \approx -130°$ and $\phi \approx 120°$. (Pelton & McLean, 2000).

The adsorption of proteins to solid surfaces is mainly governed by hydrophobic interactions but the net charge of the protein also play a crucial role and may interfere with the adsorption process according to the pH and ionic strength of the solution (Donatan, 2012). At peptide–solid surface interface protein adsorption is governed by two main mechanisms. The first one is the intermolecular forces, namely Coulombic forces, Van der Waals forces and hydrophobic interactions. The second mechanism involves intramolecular forces related to the conformation (Haynes and Norde, 1994).

In addition to those interactive forces, the charging state of the solid- liquid interface plays also a key role in both the diffusion of peptides towards the surface and the adsorption to the surface. Therefore the electrical state of the solid surface at the specific pH conditions should not be overlooked.

As we know, at the solid-liquid interface the area next to the solid surface is negatively charged either by ionization or dissociation of surface groups, by adsorption of ions from solution to a previously charged surface or by electrostatic

attraction forces between two dissimilar very closely placed surfaces. The electric charge of the solid surface is balanced by an equal amount of the opposite ions situated in the interfacial region between the solid-liquid boundaries. This interfacial region is constituted of two separate layers. The one closest to the solid surface is called *Stern* or *Helmholtz* layer. The ions in the Stern layer are bound to the surface. The outer layer is called the *diffuse electric layer.* The double layer structure is illustrated in Figure 6.4. Along the double layer an exponentially decaying electric potential exist at the solid-liquid interface (Israelachvili, 2011).

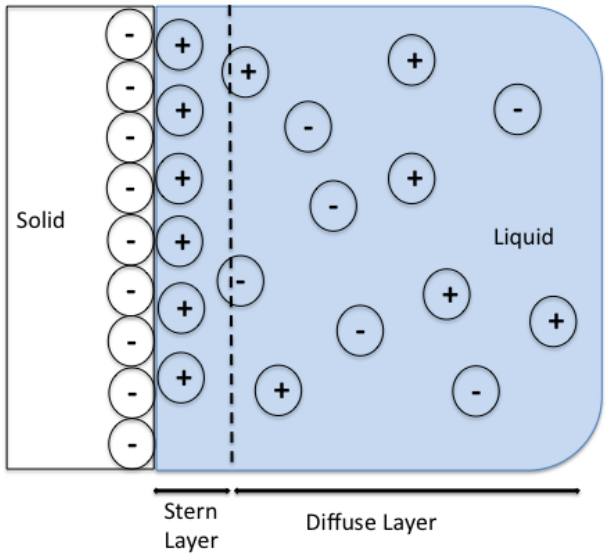

Figure 6.4 : Electrical double layer at solid-liquid interface.

The main parameters defining the electrical state of a surface are isoelectric point, point of zero charge (PZC) potential and open circuit potential (OCP). The isoelectric point corresponds to the pH value where the net charge of the Stern layer is zero. The same definition is valid for the PZC potential thus isoelectric point and PZC potential may be the same if the solution contains only H^+ and OH^- ions. PZC is the equivalent of the electrode potential. It is the condition where there is net zero surface charge on a solid surface immersed in an electrolyte.

6.2 Materials and Methods

The GBP used in this study are prepared by the synthesis of 3rGBP in a solid phase peptide synthesizer (CS336X, CSBio Inc., Menlo Park, CA). The synthesis process

leaves the N and C terminus of the peptide unblocked. The purification of the peptide was done by C-18 reverse phase liquid chromatography up to 95%.

The protein buffer solutions were prepared at four different pHs (4.5, 7.4, 10.28 and 12) by adjusting with 1M HCl and NaOH in ultrapure water. GBP concentration was prepared as 100 ng / 1ml.

SERS substrates consist of free standing gold nanowire arrays prepared as described in the previous chapters. The substrates were cleaned several times in an ultrasonic bath prior to usage.

Renishaw inVia Raman microscope (Renishaw instruments, United Kingdom) attached to a Leica upright microscope equipped with 10X, 20X, 50X and 100X objectives. For all peptide experiments 514 nm green laser and 632.8 nm visible lasers were used. 1200 lines /mm or 2400 lines /mm gratings were used according to the excitation wavelength. Integration time for all spectra varied between 30-100 sec. The system is attached to a high sensitivity ultra-low noise RenCam CCD detector. Raman scattering was collected again with a 180° backscattering geometry.

6.3 Experimental

In all experiments drop casting deposition Raman (DCDR) method was used. SERS substrates were gold nanowire arrays identical to the ones used in the previous section for BSA experiments.

All protein solutions were prepared with ultrapure water (Merck & Co, Inc., USA). The pH studies were done with four different pHs: 4.5, 7.4, 10.28, 12. The solution pHs were adjusted by using 1M of NaOH and HCl solutions.

All SERS measurements were repeated from 3 different areas of the substrate on two different identically prepared substrates. Wire 3.2 software was used for data processing (background subtraction and baseline correction with multiple point linear curve fitting baseline correction).

6.4 Results and Discussions

Raman spectroscopy of proteins and correlation of this spectra to their structural information has been first studied by Lippert et al.. In this work Lippert and co-

workers developed a method for the quantitative analysis of the secondary structure composition of proteins based on the intensities of some specific bands (amide I and III). This was followed later by Williams and co workers who used the amide I spectra of proteins with known structure as a reference spectrum (Williams and Hendrickson, 1984). This referencing method has been used by others although it presented several inconsistent results mainly due to solvent contributions (Sane et al., 1999).

General properties of the Raman / SERS spectra of peptides and proteins evolve around two critical spectral regions. The first one is usually around 500-1750 cm^{-1} region where the major characteristic protein bands are seen. The second one is around 3000 cm^{-1} where broad overlapping CH stretching vibrations and NH_2 stretching bands appears (Kinalwa et al., 2011, Thomas, 2001).

The vibrational spectrum of characteristic protein structures is detected around same frequencies for all proteins. The place of those distinctive bands is defined by intramolecular properties such as peptide bond angles (Φ and φ values determining whether if the peptide backbone structure is composed of α-helix, β-sheet, turn or random forms) and hydrogen bond occurrence (Pelton & McLean, 2000). This is why the vibrational spectra of proteins can be used to assess properly their secondary structure.

Of particular importance is the spectral region between 1600-1700 cm^{-1} reflecting the secondary structure of the proteins through the characteristic amide I band. Amide I band is composed of 80% C=O stretching mode (plus some small contributions from out-of-phase CN stretching, CCN deformation and NH in-plane bending vibrations) and is detected around 1650 cm^{-1}. The protein side chains do not contribute to the place of this band thus it is definitely and solely indicative of the secondary structure. However the amide I band of turns can not be distinguished easily from helices and sheets and therefore should be interpreted with precaution and together with the rest of the spectra (Pelton & McLean, 2000, Thomas, 2001, Barth, 2007). The α-helix structure is observed at 1648-1660 cm^{-1} whereas β-sheet is at 1625-1640 cm^{-1} and β-turns at 1660-1685 cm^{-1}. The amide I band of unordered peptides is seen between 1652-1660 cm^{-1}. Obviously those bands may be overlapped and the correlation between the structure and the band region may not be absolute as mentioned previously (Lippert et al., 1975, Maiti et al., 2005).

The secondary structure determination by amide I band is summarized in table 6.1.

Table 6.1: Amide I band positions (cm^{-1}) and their general attributions to the secondary structure of proteins.

Conformation	**Raman band (cm^{-1})**
α-helix	1650-1657
Antiparallel β-sheet	1612-1640 or 1670-1690 (weak)
Parallel β-sheet	1626-1640
Turn	1655-1675
Unordered	1640-1651

The amide II band results from 60% NH in-plane bending and 40 % CN stretching (plus some contributions from CO in plane bend and CC and NC stretching vibrations) and is recorded around 1550 cm^{-1} spectral region. This band helps to comment on the solvent accessibility of the protein and differentiate between unordered and helical conformations (Barth & Zscherp, 2002). Amide II band is also not influenced by side chain contributions. But unlike amide I band, amide II band does not allow to comment directly on the secondary structure and the correlation is more complicated (Barth, 2007).

Amide III band region is situated around 1300 cm^{-1} and is also used to determine the α-helix and β-sheet content of the protein structure. The amide III band vibration is composed of 40% CN stretch and 30% NH bend. Unlike amide I and II this mode is influenced by side chain contributions in polypeptides.

Other characteristic vibrational regions are 1555-1605 cm^{-1} for asymmetric COO^- stretching vibrations, 1490-1530 cm^{-1} for symmetric NH_3^+ vibrations, 1315-1340 cm^{-1} for CH deformations, around 1400 cm^{-1} for COO^- symmetric stretching, around 1430 cm^{-1} for CH_2 bending vibration, 1300 cm^{-1} for CH_2 group wagging, 1343 cm^{-1} for CH bending, 1100 cm^{-1} for CCN asymmetric mode, 784 cm^{-1} for CH_2 group rocking, 500-700 cm^{-1} for S-S stretching deformations (Podstawka, 2008, Maiti et

al., 2005). All SERS spectra of 3rGBP are therefore evaluated according to those major bands.

6.4.1 Raman Spectrum of Solid GBP

First the Raman spectrum of the solid 3rGBP molecule is recorded. The structure is important to evaluate SERS results by comparison and to assess the relationship with previous studies handling the solid molecule.

The characteristic Raman bands of gold binding peptide and their tentative assignments to probable amino acids are given in table 6.2. The Raman spectrum is given in Figure 6.5. The band assignments are made by comparison with similar amino acids and peptides according to the literature (Zhu et al., 2011, Stewart & Fredericks, 1999, Sengupta et al., 2008).

The strong amide I band situated at 1670 cm^{-1} confirms the disordered random coil-extended conformation of 3rGBP. The structure is probably mixed with anti-parallel β-sheets and turns. The amide II band is located around 1550 cm^{-1} and is very weak since this mode is not strongly Raman active and may be influenced by side chain contributions. The amide III region (1200-1300 cm^{-1}) can also be clearly distinguished in the spectrum with two strong bands at 1237 cm^{-1} and 1266 cm^{-1} respectively. The other weak to moderate intensity bands observed in the spectrum can be attributed to the side chain groups of several amino acids.

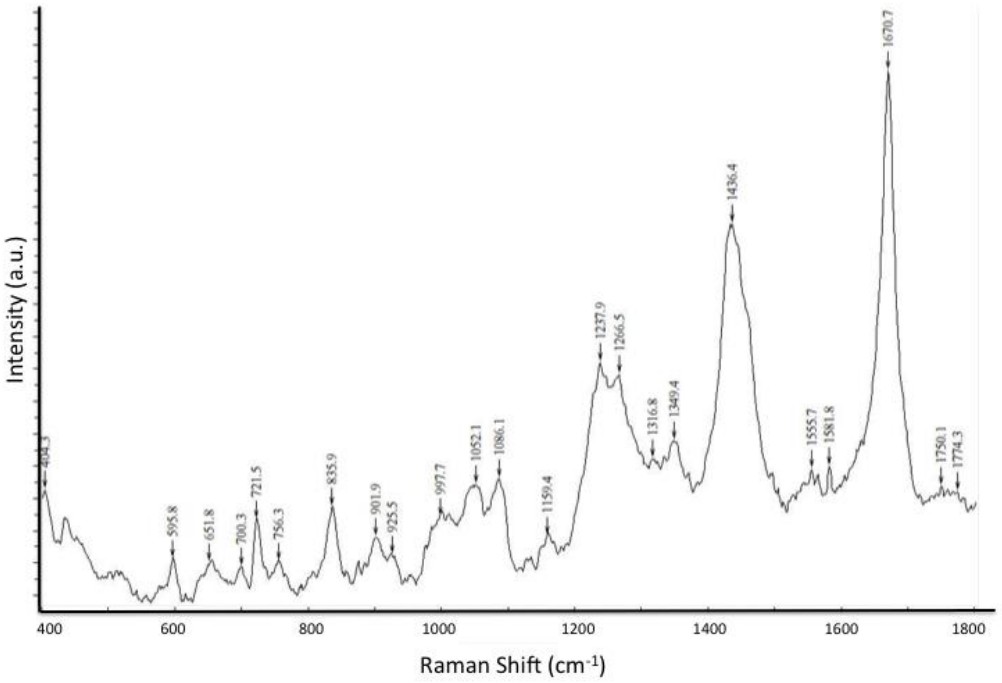

Figure 6.5 : Raman bands of solid GB

Table 6.2: Tentative Raman band assignments of solid GBP at pH 7.4.

Band Position (cm-1) Solid GBP	**Tentative Assignments**	**Literature**
404	M	M (m)
430	I	I (s) 536
595	I, H, S	I (s) 536, H (m) 539, S (m) 610
651	M	M (s) 645
700	M	M (m) 700
721	M	M (s) 721
756	M, H	M (m) 765, H (m) 731
835	A, S, K	A (s) 852 , S (m) 854, K (m) 849
901	G, T, M	G (s) 894, T (s) 872, M (m) 877
925	H	H (m) 929
997	H, S	H (m) 977, S (m) 969
1052	T	T (m) 1045

1086	A	A (m) 1105
1159	G	G (m) 1154
1237	I	I (m) 1252
1266	T, I	T (m) 1251, I (m) 1252
1316	H, S, I	S (s) 1319, H (s) 1327, I (s) 1329
1349	T, I	T (s) 1341, I (s) 1355
1436	K, T, M	K (s) 1456, T (w) 1458, M (m) 1447
1581	All Amino acids	
1670	All Amino acids	

6.4.2 Assessment of the influence of the solution charge to the adsorption behaviour of GBP monitored by SERS

Proteins have ionisable groups on their side chains and amino and carboxyl ends. They may be positively or negatively charged according to solution charge via deprotonating or protonation of their acidic and basic groups. The pH value where the net charge of a protein is zero is called the isoelectric point. At this pH the protein is unstable and least soluble. Above the isoelectric point the protein is negatively charged thus behave like a cation. Below this point it is positively charged hence behaving like an anion. Therefore the alterations of the solution charge might affect the protein adsorption by two ways: First solution pH affects the solubility of a protein and second it determines the net charge of the protein molecule.

But before discussing the effect of the solution charge on the adsorption properties of GBP, it should also be mentioned that changing the solution pH interferes inevitably with the electrical double layer properties at the metal solution interface. Donatan et al. measured the open circuit potential (OCP) of flat gold surface at different pH values and constructed a pH-potential diagram (Figure 6.6). Although the SERS

substrates used in this study are nanowire arrays we assume that the OCP-pH relationship will not be greatly affected (Borghi et al., 2013).

The PZC is measured against standard hydrogen electrode as 143±10 mV. The PZC potential means that at this potential (at pH 5,2 corresponding to the PZC potential) the net surface charge of the gold surface is zero. As seen from the Figure 6.6, when the OCP value is above PZC the surface is negatively charged and at OCP below PZC the surface is positively charged. Therefore the electrical charged state of the surface is linked to the pH of the solution and should be considered when commenting on the adsorption studies of the proteins.

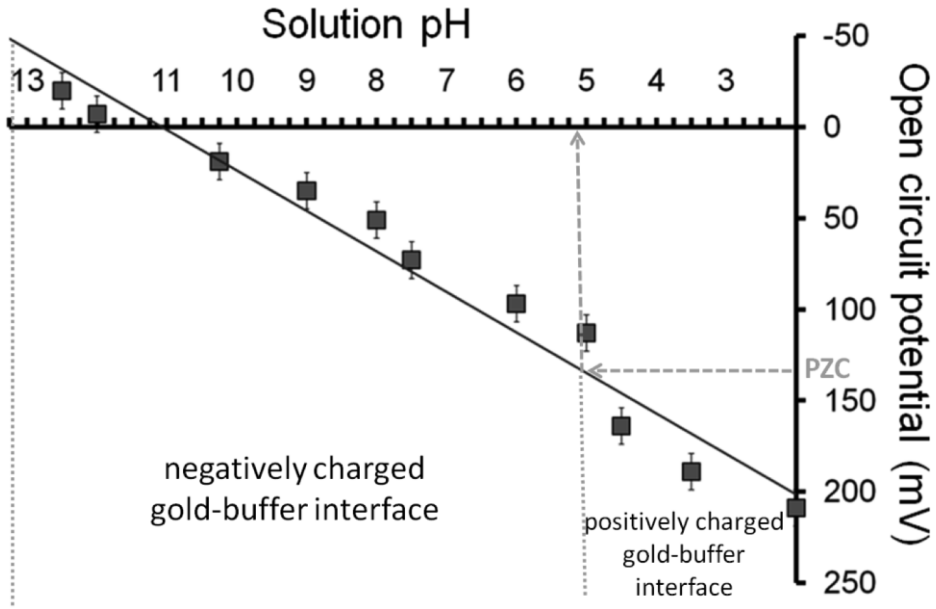

Figure 6.6 : Variation of potential with pH of the gold coated QCM electrode in 100 ml KCl containing phosphate buffer. (Donatan et al., 2011).

The effect of the solution charge is studied for four different conditions summarized in table 6.4.

The first SERS spectra to be analysed is at pH 7.4. This pH value is taken as the reference point since the majority of adsorption studies of 3rGBP are performed at this pH

Table 6.3 : Surface and peptide charge conditions according to solution pH.

Solution pH	Net charge on $3rGBP_1$	Sign of excess charge on the gold

		surface
4.5	+6	+
7.4	+3	-
10.28[a]	0	-
12	-1	-

a pH 10.28 is the isoelectric point (pI) of $3rGBP_1$

At pH 7.4 the net surface charge of 3rGBP is +3. This charge is calculated as the sum of the negatively charged carboxyl end at C-terminus, the positively charged amino terminus and three positively charged lysine residues (Berg et al., 2006).

The SERS spectrum at pH 7.4 is presented in Figure 6.7. The observed spectrum was mostly constituted of several weak bands on top of an enhanced general background. None of the bands was strong enough to comment on a possible distinct binding regions or orientation of the peptide on the surface. This outcome was not surprising when interpreted in correlation with previous works. Kulp et al., 2004 reported that 3rGBP interacted with the gold surface in its unfolded state composed of random coil and extended structure. Our results is in agreement with Kulp et al.'s conclusion since the recorded spectrum show a mixture of bands, which may originate from several different amino acids all interacting with the surface. On the other hand studies by So et al., 2009 suggested a possible binding of the peptide to the gold surface via polar (e.g. glutamine, serine or threonine) and cationic residues (e.g. lysine or histidine) at pH 7.4 through electrostatic interactions. When the most distinct bands at the spectrum are examined closely it is noticed that defined bands such as 833 cm^{-1} and 1454 cm^{-1} are probably due to lysine residues and 998 cm^{-1} and 1358 cm^{-1} to histidine residues (see table 6.2) (Zhu et al., 2011). Although neither of these residues showed a noticeable enhancement in our SERS spectrum their presence is a strong indication of the interaction of the peptide with the underlying gold surface.

When the surface charge of the interface is investigated the solid surface-solution interface is negatively charged at pH 7.4 (Figure 6.6). So the peptide was expected to

adsorb to the surface through its positively charged polar residues such as lysine or histidine via electrostatic attraction interactions. Again, bands originating from the positively charged amine terminus and positively charged lysine residues were not particularly enhanced on the SERS spectrum. This outcome could be explained in correlation with Donatan's work (Donatan et al., 2012) that predicts a decrease of the total coverage area of the peptide at negatively charged interfaces. Hence the peptide is probably in contact with the underlying gold surface through only a small portion of its positively charged residues (thus their presence in the spectrum without enhancement) while polar residues on the peptide's backbone and negatively charged C terminus lie away from the surface. The limited interaction of the peptide with the gold surface was not strong enough to promote a more pronounced enhancement yet the presence of several defined bands with almost equal enhancement shows that the peptide has placed itself on close proximity of the surface. Plus, the absence of strong and defined amide bands in the spectrum suggests a possible conformational change towards a more disordered, open linear structure. This hypothesis is also in agreement with previous studies by So's previous reports stating that the peptide attach itself to the surface without an internal folding causing side chain intramolecular interaction within 3rGBP thus leaving the majority of the sequence available to the surface (So et al, 2009).

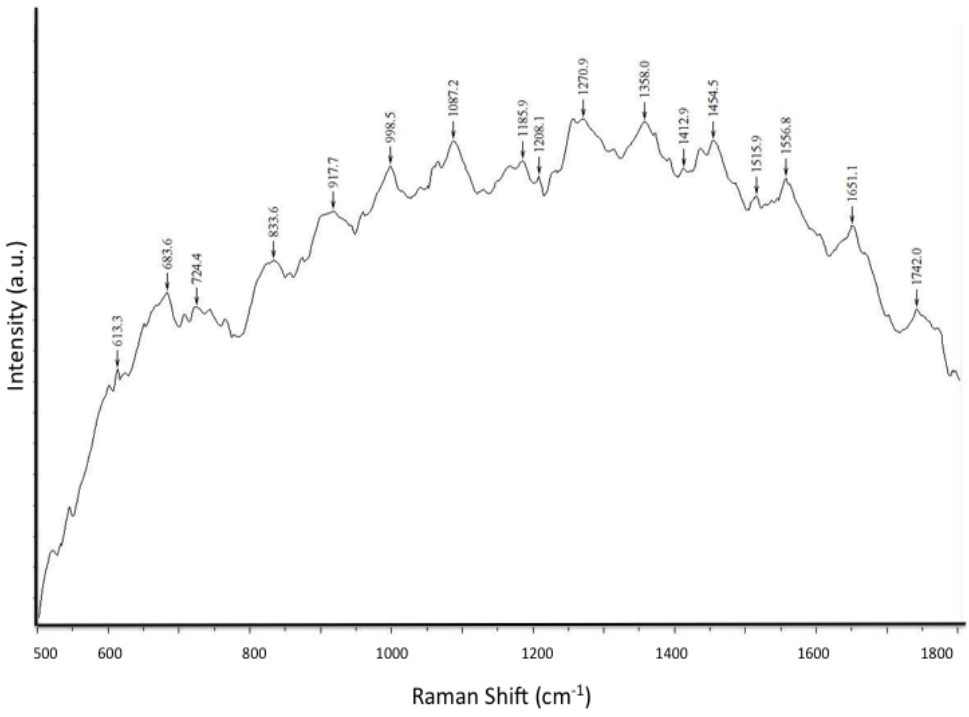

Figure 6.7 : SERS spectra of GBP at pH 7.4

When the solution charge is adjusted to pH 4.5 to assess the effect of excess positive charges on the interface a completely different adsorption mechanism was encountered. At pH 4.5 the net charge of the peptide is +6 arising from 3 protonated lysine and histidine residues. The SERS spectrum of the peptide at pH 4.5 is given in Figure 6.8. The presence of strongly enhanced bands allowed us to comment on how the peptide might be situated on the gold nanowire surface. The portions of the peptide structure leading to a more defined enhancement were the areas of the peptide that were situated in the closest proximity of the gold surface hence possible adsorption sites.

The strongest intensity bands were seen at 841 cm^{-1} (C-COO^- and CCN stretching modes), 1004 cm^{-1} (C-N stretching) and 1434 cm^{-1} (COO^- symmetric stretching and CH_2 bending vibration). The amide I band was still present although not enhanced strongly. Its position was slightly shifted compared to solid GBP and another band, at 1638 cm^{-1} was seen in the SERS spectrum suggesting a conformational change (probably towards β-sheet structure) upon adsorption to the gold surface. This is in agreement with Suzuki's statement saying that the antiparallel β-sheet structure is the thermodynamically most favourable conformation for adsorption (Suzuki et al, 2007). Furthermore the presence of the amide I band suggests that the peptide might be placed on the surface with all its amino acid residues lying horizontally on the surface since all amino acids in the structure contribute to this band.

Since, under these conditions (pH 4.5 total peptide charge +6). according to the model proposed by Donatan et al the carboxyl terminal of the peptide should be in close proximity to the gold surface while the amine terminus is lying away from it Two regions in the SERS spectrum support this model. First one is the presence of a strong band at 1563 cm^{-1} originating from the asymmetric COO^- stretching mode. And the second one is the presence of the main enhanced region in the spectrum around 1500 cm^{-1} occurring mainly from the presence of the bands assigned to the carboxyl terminus of the various side groups. The shift and enhancement of other bands such as 724 cm^{-1} and 1434 cm^{-1} are highly possibly related to the deformation and symmetric stretching modes of the carboxyl group, which are also indicators of the interaction between the peptide and gold surface through the peptide's carboxyl terminus. Under these conditions, the positive charge state of the surface (Figure

6.6) is expected to repel positively charged amine terminus of the peptide from the surface due to electrostatic interactions. This statement is justified by Donatan's work showing that in case of excess positive interfacial charge there are more adsorption sites on the peptide and the peptide is interacting with the surface with its maximum contact area at its stretched form (Donatan et al., 2012).

The comparison of the SERS spectrum with solid GBP Raman spectrum is presented in Figure 6.8. By simple observation of these two spectra it is noticed that some residues of the molecule were strongly enhanced upon adsorption while some features of the solid GBP spectra were shifted and/or lost their intensity. Therefore The evaluation of GBP SERS spectra at pH 4.5 compared to solid 3rGBP Raman spectra shows that several bands were enhanced in the SERS spectrum when the surface charge is altered (Figure 6.9). This result is not surprising when evaluated together with molecular dynamic studies done by So et al., in 2009 stating that the peptide is mobile on the surface through a disordered fibrilar structure similar to elongated nanodomains.

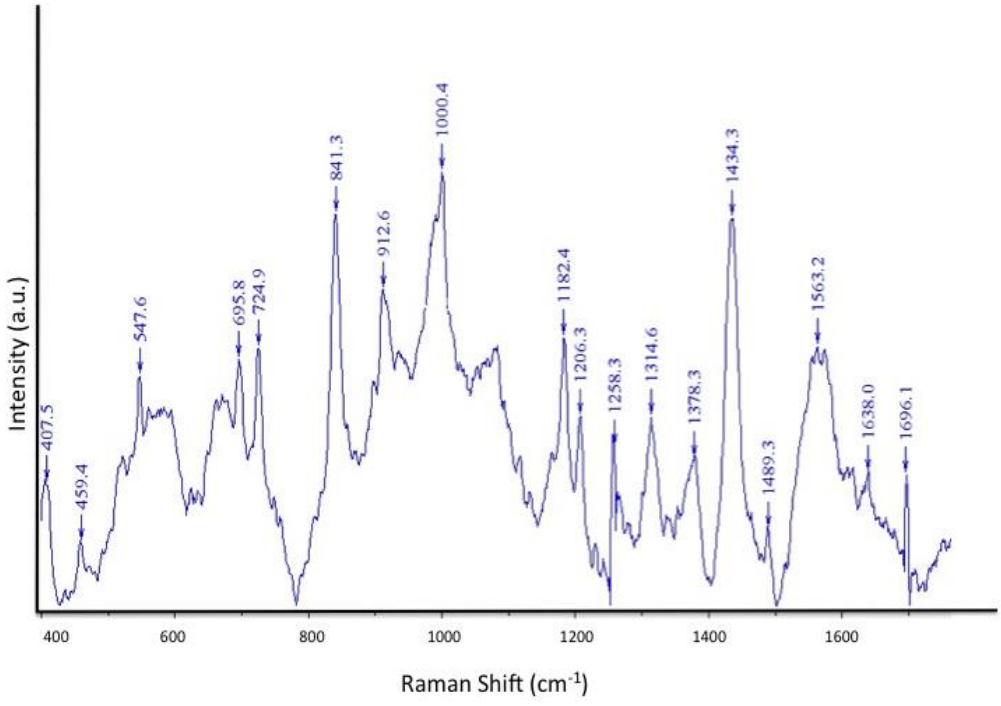

Figure 6.8 : SERS spectra of GBP at pH 4.5.

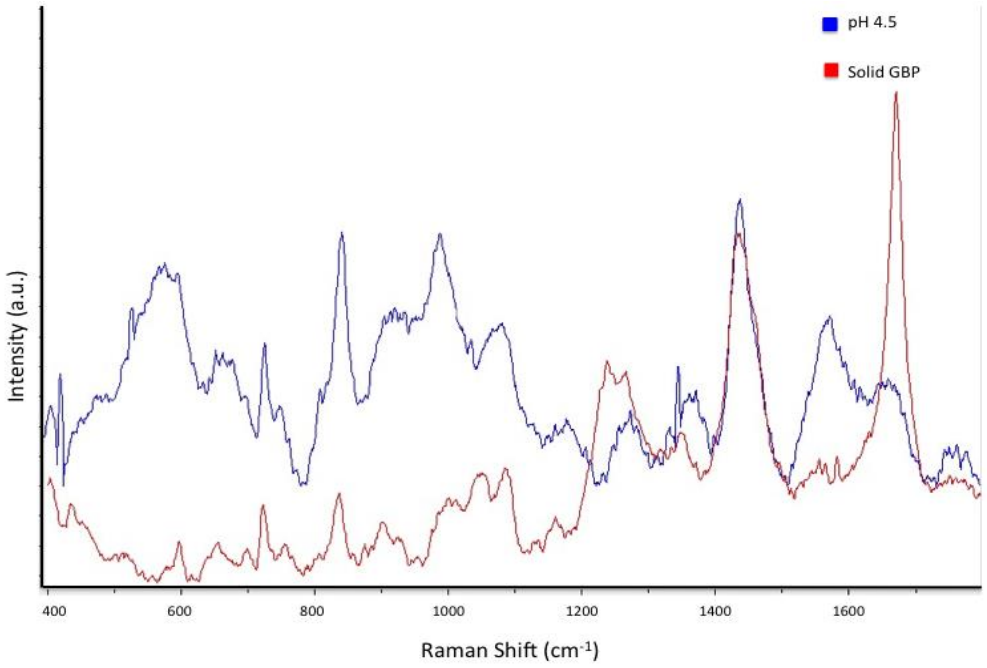

Figure 6.9 : Comparison of the solid GBP Raman bands with the SERS spectrum of GBP at pH 4.5.

In the next step the surface charge is brought to match the isoelectric point (pH 10.28), where the net surface charge of the peptide is zero. Figure 6.10 presents the SERS spectrum at this pH. First of all, amide III band was not observed on the spectra. This particular result may suggest that the peptide was adsorbed to the surface in its disordered form. Secondly, the strongest band on the spectra was observed around 580 cm^{-1}, which is the region of sulphur-based interactions. The sulphur based interaction could only result from the thiolether group of the side chain of the methionine residues present at the structure. Thirdly, several weak bands were observed, which is similar to the results of the experiments conducted at pH 7.4.

At isoelectric point the absence of the net charge on the peptide structure suggests minimum electrostatic interactions. This is supported by Donatan's results obtained when the net surface charge was zero (at PZC conditions). Therefore hydrophobic interactions between the peptide and the surface should be favoured in the adsorption mechanism. The strong band coming from methionine residues is in agreement with this hypothesis.

When the SERS spectrum was compared to solid GBP Raman spectra noticeable changes were observed easily (Figure 6.11). For instance the amide II band situated between 1540-1580 cm^{-1} regions was enhanced. Being not a strong Raman active

vibration, amide II band could only be enhanced in SERS in the case of adsorption of the molecule to the surface (Podstawka et al., 2008). This particular result suggested strongly that the peptide was adsorbed to the surface however it did not undergo any conformational rearrangement upon the adsorption process. Therefore the peptide structure was probably in a homogeneously aligned form on the surface but due to the lack of electrostatic adsorption forces the peptide-gold interaction was not sufficient enough to promote binding and rearrangement on the gold surface (thus the absence of particular enhancements).

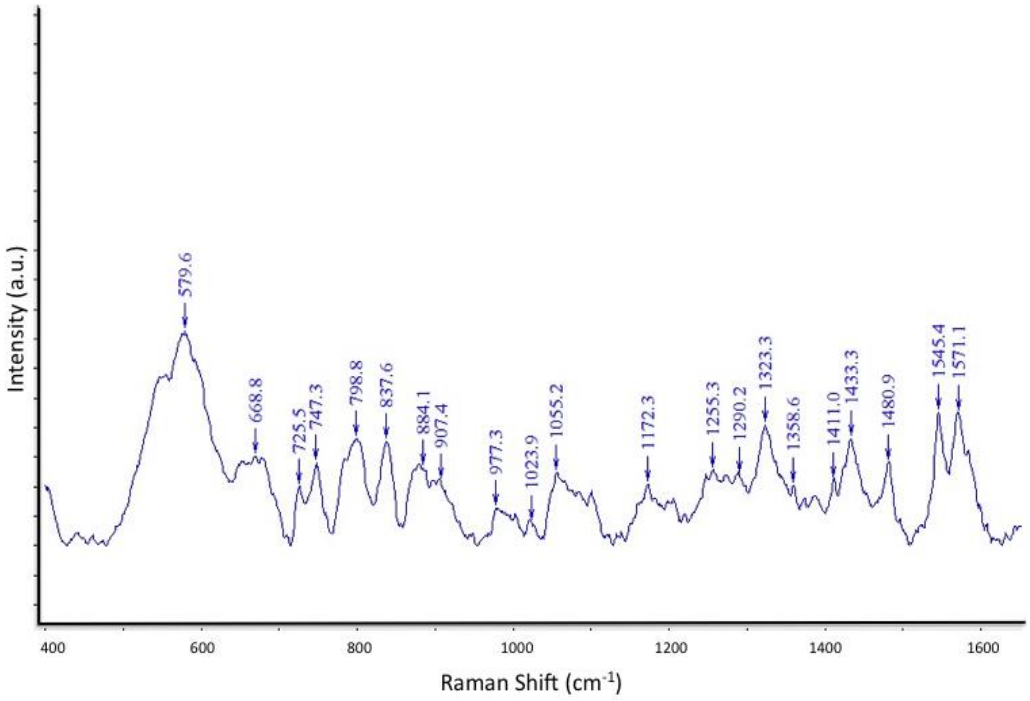

Figure 6.10 : SERS spectra of GBP at pH 10.28.

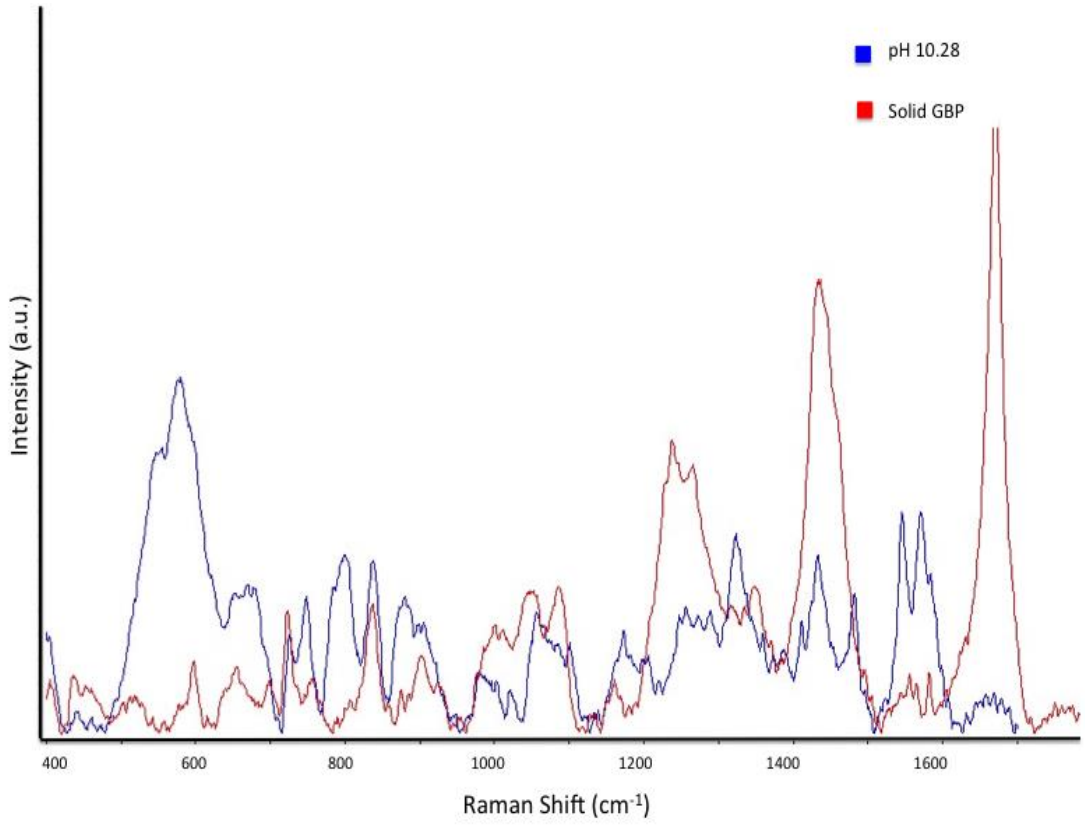

Figure 6.11 : Comparison of solid GBP Raman bands with the SERS spectra of the GBP at pH 10.28.

Finally in the case when the surface and the peptide (-1) are both negatively charged (at pH 12) low adsorption was expected due to electrostatic repulsion forces (Donatan, 2010). The SERS spectrum of GBP at pH 12 is presented in Figure 6.12.The amide III band was only weakly present in the spectrum. The sulphur-based interaction via methionine residues may again be involved in the adsorption mechanism since the band around 600 cm^{-1} was again enhanced. Other polar amino acids such as serine, glutamine, threonine and glycine were probably contributing to the adsorption since several defined bands were observed although not enhanced strongly. The moderate enhancement and the presence of several bands suggested that the adsorption conditions were far from being site specific and a relatively low adsorption process was taking place. The decreased adsorption was in case of excess negative surface charge was also predicted by Donatan (Donatan et al., 2012).

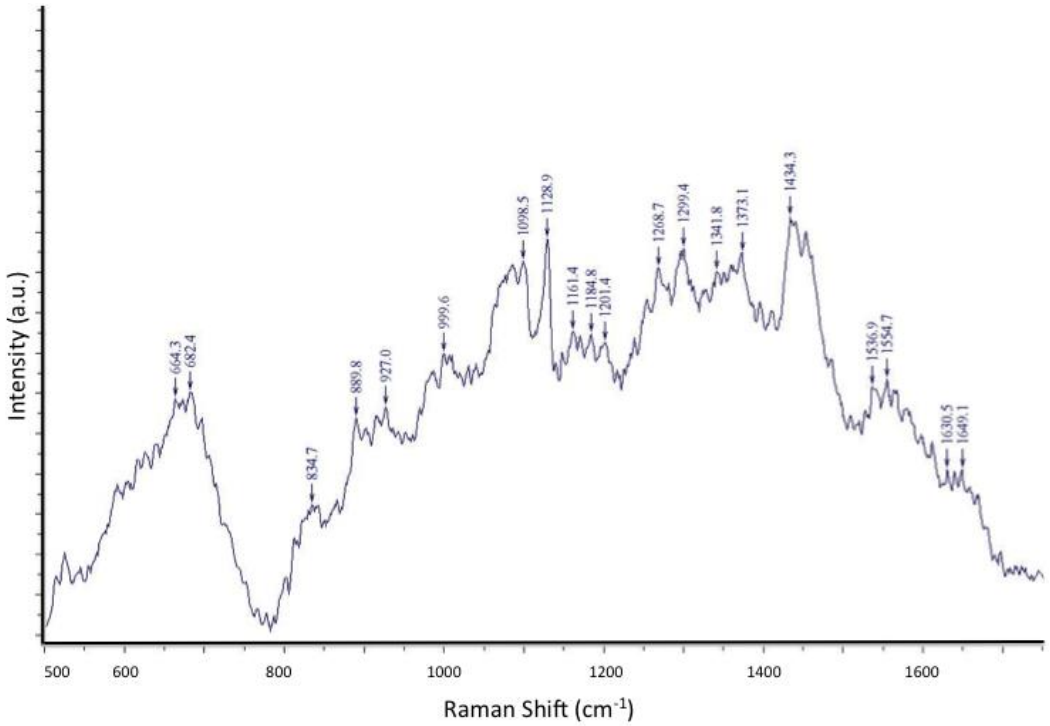

Figure 6.12 : SERS spectra of GBP at pH 12.

When all experiments performed at the four different surface charge states were compared, strong and clear enhancements were observed for the spectrum obtained at solution pH 4.5 (Figure 6.13). Previous studies correlating protein net charge density and adsorption properties carried out by Donatan stated that positive net charge accelerated the adsorption rates and generated a full coverage of the gold surface with a close packed monolayer peptide film (Donatan et al, 2012). Our findings supports this hypothesis since the strongest enhancements arousing from the negatively charged C-terminus of the peptide dominates the SERS spectrum at pH 4.5. Moreover at this pH value conformational change of the peptide towards an increase of the β-sheet structure was observed which suggested that GBP molecule went through a conformational reorganization upon adsorption. This outcome is in agreement with So's works (So et al., 2009, So et al., 2009).

Since GBP is found in its intrinsically disordered form in solution (meaning that its residues were not involved in either internal folding / stabilization or side-chain interactions within the peptide) the majority of the residues were exposed to the gold surface (So et al., 2009, Kulp et al., 2004). The presence of several other bands in the SERS spectrum was also in agreement with this condition.

From Figure 6.13 illustrating the superposition of all four SERS results at different surface charges it can easily be noticed that the strongest enhancement of the spectrum was obtained at pH 4.5. The spectrum at pH 12 presented almost entirely the same bands albeit much weaker. This similarity was not surprising since both conditions are under electrostatic repulsion forces between the substrate and GBP molecule and hydrophobic interactions are probably governing the adsorption process through the same amino acid residues.

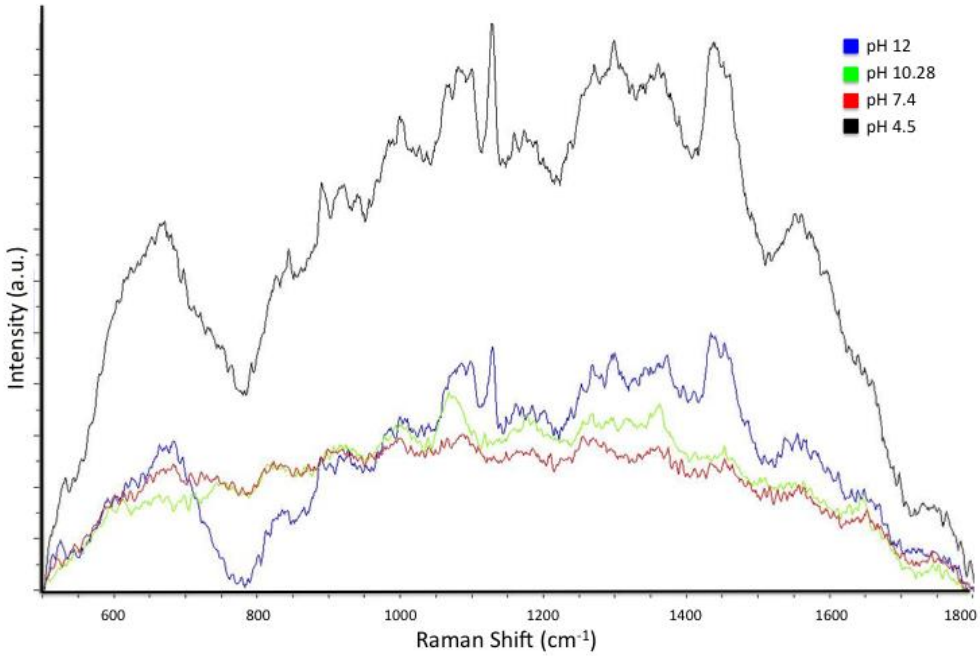

Figure 6.13 : SERS spectrum of GBP at various pH values. All of the spectrums are background subtracted.

6.5 Conclusions

In summary, we investigated herein the effect of the surface charge alteration to the adsorption behaviour of 3rGBP with SERS for the first time. Results indicate that electrostatic attraction forces play a key role in the adsorption of 3rGBP to gold surface under appropriate conditions. Moreover on charged surface states 3rGBP is capable to adapt its conformation and flexibility on the surface suggesting that the adsorption of 3rGBP is a dynamic process.

When results of the study is briefly summarized we see that:

At pH 7.4:

- Several weak bands are observed without significant enhancement.

- No particular enhancement of positively charged amino acids is seen but their distinct presence in the spectrum suggest an interaction of the peptide with gold surface through those residues

At pH 4.5:

- The spectrum shows strongly enhanced bands. The strongest intensity is observed for the bands related to the negatively charged C terminus of the peptide
- The presence and shift of the amide I band suggests a conformational rearrangement of the peptide at the interface.

At pH 10.28:

- The amide III band was absent from the spectrum, suggesting a possible disorder of the structure.
- Sulphur-based interactions may play a role stronger than other kinds of interactions.
- Several weak bands are again observed which is similar to the pH 7.4.

At pH 12:

- The spectrum is similar to the one at pH 4.5 but much weaker.
- Due to electrostatic repulsion, it is highly probable that hydrophobic interactions take place at this pH.

By this work, we demonstrated the versatility and the utility of surface enhanced Raman spectroscopy as a straightforward, reproducible and reliable technique, which is capable of giving strong information to enlighten adsorption mechanisms of biological molecules if appropriate substrates are used. The present study signifies an example for the utility of SERS in order to evaluate the adsorption conditions of 3rGBP to gold SERS substrates. Even thought there is a pervious report on the literature for the investigation of adsorption behaviour of a GEPI (silver binding peptide) this study represents the first example of using a solid substrate instead of colloidal conventional substrates (Sengupta et al., 2008).

The same method is potentially a highly valuable tool that can be easily adapted for other selected GEPI's by modifying the substrate material i.e. silver, copper, and

platinum instead of gold. We have also previously showed that our template-based approach was suitable for the fabrication of other freestanding nanowire arrays (i.e. silver and nickel). Hence by careful design and tailoring of the template (AAO) and thus the final SERS substrate (arrays of free standing metallic nanowires) properties, the method can therefore successfully be expanded to the analysis of other GEPI's. The work realized in this chapter can form a precursor for SERS based peptide-material interaction studies and can surely be extended to a more elaborate research under different conditions.

7. CONCLUSIONS AND FUTURE PROSPECTS

We had three objectives when starting the ensemble of works constituting this dissertation. The first one was to determine and qualify what formed a good SERS substrate and design and fabricate this substrate in an economical, simple yet effective way. This objective was attained successfully by using a template-based approach adapted for electrochemical deposition of metallic nanowires. Freestanding arrays of metallic nanowires obtained by DC electrodeposition on zincate treated AAO templates were produced for the first time. Zincate treatment technique was optimized for specific temperature and treatment time parameters in order to obtain nanowire arrays within predesigned size ranges. The resulting arrays were standardized in terms of length and pore diameter distribution (with approximately 70 % of all diameters for three different metals, Au, Ag and Ni, being between 100 - 150 nm).

Our second objective was to establish the SERS activity, efficiency and functionality of freestanding gold nanowire arrays as a versatile SERS substrate. The enhancement sensitivity was optimized with respect to the aspect ratio of nanowires by using Rhodamine 6G as the probe molecule for the evaluation of the enhancement power. The enhancement factor was calculated as 5×10^{-6} with 632.5 nm excitation source. Once it was established that the substrates were well performing, robust, reproducible and homogeneous it was clear that our approach created a straightforward, simple and elegant methodology for the production of SERS substrates. The best SERS performance was obtained from the arrays with an aspect ratio of 7.74 (with 140 nm pore nanowire diameter and 1100 nm length). The anodization conditions leading to this result was optimized as 40 V for 1 h at the first anodization step and 70 V for 5 min at the second anodization step. Those conditions are very convenient when compared to anodization times in the literature and results easily and quickly in appropriate sized templates. Therefore the nanowire aspect ratios obtained prepared via those AAO templates were in suitable ranges for an

excitation wavelength of 632.5 nm to promote localised surface Plasmon oscillations for SERS enhancement. Moreover under these conditions the small distance between two neighbouring nanowires (15 ± 3 nm average gap size) was found to be highly suitable for forming hot spots where Plasmon coupling between the nanowires occurs. Raman mapping studies of the gold nanowire array have also been done and the results proved a highly homogeneous distribution of the enhancement capabilities for both 611 cm^{-1} and 1340 cm^{-1} bands of the R6G molecule.

To establish the SERS functionality of the substrates a large biological molecule: BSA was used. Moreover AAO templates and hence their resulting SERS counterparts were tuned to a size range suitable for 735 nm laser excitation, which also proves the tenability of the technique. The results indicated unbroken cystide-disulphide vibrations around 500 cm^{-1} and the presence of amide bands showing that besides being strong Raman enhancers, the substrates were not causing any chemical instability leading to the denaturation of the protein upon adsorption. Strong bands originating from lysine, leucine and glutamic acid residues were observed, which was an expected outcome since those were the most abundant amino acids in the BSA structure. The correlation of the BSA study with the literature data showed that our gold nanowire arrays were ideal candidates for more complex biological studies avoiding commonly occurring problems of conventional templates such as aggregation, random binding, and inhomogeneous surface areas. By this way the usability of the substrates for SERS analysis of biological molecules was successfully demonstrated.

Our third objective was to investigate, for the first time in the literature, the effect of the surface charge alteration to the adsorption behaviour of 3rGBP with SERS. Herein we showed the versatility of the templates for the investigation of protein adsorption studies. For the first time in this study, 3r GBP has been investigated by SERS on gold nanowire array substrates at four different surface charge states (pH 4.5, pH 7.4, pH 10.28 and pH 12). Our findings indicate that the best adsorption was achieved at pH 4.5 through the negatively charged C-terminus of GBP. The adsorption behaviours at pH 7.4 and 10.28 were hard to differentiate from each other. All pH conditions resulted with adsorption behaviours conform to what was previously reported in the literature.

In summary, we demonstrated the utility and the versatility of a template-based approach via pore bottom activation of AAO to produce good quality, well performing and reproducible and robust SERS substrates. We showed the potential of those substrates in the detailed investigation of small biological molecules through the example of GBP. It is obvious that those results can lead to more elaborate studies in terms of both other metallic SERS substrates, biological molecules and under different experimental conditions.

REFERENCES

Aizpurua, J. and Hillenbrand, R. (2012). Localized Surface Plasmons: Basics and Applications in Field-Enhanced Spectroscopy, *Plasmonics*, Springer Series in Optical Sciences *16***,** p. 151, Eds., S. Enoch and N. Bonod, Springer-Verlag Berlin Heidelberg.

Albrecht, M. G. and Creighton, J.A. (1977). Anomalously intense Raman spectra of pyridine at a silver electrode, *J. Am. Chem. Soc.*, *99***,** 5215-5217.

Alexander, T. and Wickenden, A. (2004). Electron-beam-lithography (EBL)-engineered nanostructures for biosensing, *SPIE Proceedings*,Smart Medical and Biomedical Sensor Technology II, *5588***,** p. 78-86, Eds., Brian M. Cullum.

Allain, L. R. and Vo-Dinh, T. (2002). Surface-enhanced Raman scattering detection of the breast cancer susceptibility gene BRCA1 using a silver-coated microarray platform, *Analytica Chimica Acta*, *469*, 149-154.

Baia, M., Baia, L. and Astilean, S. (2005). Gold nanostructured films deposited on polystyrene colloidal crystal templates for surface-enhanced Raman spectroscopy, *Chemical Physics Letters***,** *404***,** 3-8.

Baneyx, F. and Schwartz D.T. (2007). Selection and analysis of solid binding peptides, *Curr. Opin. Biotechnol.*, *18*, 312-317.

Barth, A. (2007). Infrared spectroscopy of proteins, *Biochimica et Biophysica Acta, **1767***, 1073-1101.

Barth, A. and Zscherp, C. (2002). What vibrations tell us about proteins, *Quarterly Reviews of Biophysics 35*, *4*, 369-430

Bayata, F. Akıncı, Z. B., Donatan, A. S., and Urgen, F. (2012). A novel free-standing nanowire substrate with surface enhanced Raman scattering (SERS) activity, *Materials Letters*, *67*, 387-389.

Benjamin, D.C. and Teale, J.M. (1978) The antigenic structure of Bovine, Serum Albumin, *The Journal of Biological Chemistry*, *253*, 8087-8092

Brahma, A., Mandal, C. and Bhattacharyya, D. (2005). Characterization of a dimeric unfolding intermediate of bovine serum albumin under mildly acidic condition, *Biochimica et Biophysica Acta, 1751*, 159-169.

Braun, R., Sarıkaya, M. and Schulten, K.J. (2002). Genetically engineered gold-binding peptides: structure prediction and molecular dynamics, *Biomatter. Sci. Polymer Ed., 13***,** 747-757.

Brown, S. (1997). Meal recognition by repeating polypeptides, *Nature biotechnology, 15*, 269-272.

Bryant, G. W., Abajo, J. F. and Aizpurua, J. (2008). Mapping the Plasmon Resonances of Metallic Nanoantennas, *Nano Letters, 8*, 631-636.

Campion, A. and Kambhampati, P. (1998). Surface-enhanced Raman scattering, *Chem. Soc. Rev.*, *27*, 241–250.

Chan H.Y.H., Takoudis, C.G., & Weaver, M.J. (1997). High-pressure oxidation of ruthenium as probed by surface-enhanced raman and x-ray photoelectron spectroscopies, *Journal of Catalysis,**172***, 336-345.

Choi, J. (2003). Fabrication of monodomain porous alumina using nanoimprint lithography and its applications, (Ph.D. Thesis), Martin-Luther-Universitat Halle, Wittenberg.

Cobley, C. M., Chen, J., Cho, E. C. C., Wang, L. V and Xia, Y. (2011). Gold nanostructures: a class of multifunctional materials for biomedical applications, *Chem. Soc. Rev., 40*, 44-56.

Delfino, I., Bizzarri, A.R. and Cannistraro, **S.** (2005). Single-molecule detection of yeast cytochrome c by Surface-Enhanced Raman Spectroscopy, *Biophysical Chemistry, 113*, 41– 51.

Dietzek, B., Cialla, D., Schmitt, M., & Popp., J. (2010). Introduction to the fundamentals of Raman spectroscopy, in *Confocal Raman microscopy*, Springer Series in Optical Sciences, 158, p.21-41, Eds. Dieing, T., Toporski, J., and Hollricher, O., Springer, Heidelberg.

Diggle, J.W., Downie, T.C. and Goulding C.W. (1969). Anodic oxide films on aluminum, *Chem. Rev., 69*, 365-405.

Ding, X., Yang, M., Hu, J., Li, Q., and McDougall, A. (2009). Study of the adsorption of cytochrome c on a gold nanoparticle – modified gold electrode by using cyclic voltammetry, electrochemical impedance spectroscopy and chronopotentiometry, *Microchimica Acta, 158*, 65-71.

D.S. Lashmore, (1980). *Painting and Surface Finishing*, 67 37.

Donatan, S., Sarıkaya, M., Tamerler, C. and Urgen, M. (2012). Effect of solid surface charge on the binding behavior of a metal binding peptide, *Journal of the Royal Society Interface,75,* 2688-2695.

Donatan, S. (2011). Specific recognition of a genetically engineered gold binding peptide on gold substrate: ınterfacial charge mechanisms, (*Ph.D. Thesis),* I.T.U., Istanbul.

El-Brolossy T.A., Abdallah, T., Mohamed M.B., Abdallah S., Easawi, K., Negm, S. and Talaat, H. (2008). Shape and size dependence of the surface plasmon resonance of gold nanoparticles studied by Photoacoustic technique, *Eur. Phys. J. Special Topics, 153*, 361–364.

Etchegoin, P., Liem, H., Maher, R.C., Cohen, R.F., Brown, R.J.C., Milton, M.J.T. and Gallop, **J.C.** (2003) Observation of dynamic oxygen release in hemoglobin using surface enhanced Raman scattering, *Chemical Physics Letters, **367,*** 223–229.

Evans, J.S., (2003). Apples and oranges:comparing the structural aspects of biomineral and ice interaction proteins, *Curr. Opin. Colloid Interface Sci., 8*, 48-54.

Evans, J.S., Samudrala, R., Walsh, T.R., Oren, E.E. & Tamerler, C. (2008). Molecular design of inorganic binding polypeptides, *MRS Bull.,33,* 514-518.

Fang, J.X., Lebedkin, S., Yang, S.C., and Hahn, H. (2011). A new route for the synthesis of polyhedral gold mesocages and shape effect in single-particle surface-enhanced Raman spectroscopy, *Chemical communications, 47*, 5157-5159.

Fleischmann, M., Hendra, P. J., and McQuillan, A. J. (1974). Raman spectra of pyridine adsorbed at a silver electrode, *Chem. Phys. Lett., 26*, 163–166.

Freeman, R.G., Grabar, K.C., Allison, K.J., Bright, R.M., Davis, J.A., Guthrie, A.P., et al. (1995). Self-assembled metal-colloid monolayers: an approach to SERS substrates, *Science, 267*, 1629-1632.

Furneaux, R.C., Rigby, W.R. and Davidson, A.P. (1989). The formation of controlled-porosity membranes from anodically oxidized aluminium, *Letters to Nature, 337*, 147-149.

Fusina, A., Lee, S., Sofin, R.G.S., Shvets, I.V. and Natelson, D. (2008). Nanogaps with very large aspect ratios for electrical measurements, *Applied. Physics Letters, 92*, 113102 .

Gamburg, Y.D. and Zangari, G. (2011). *Theory and practice of metal electrodeposition*, Springer, New York.

Gettens, R.T.T., Bai, Z., and Gilbert, J. (2005). *Quantification of the kinetics and thermodynamics of protein adsorption using atomic force microscopy*, Wiley periodicals Inc., 246-257.

Gungormus, M., Fong, H. Kim, I.W., Evans, J.S., Tamerler, C. and Sarıkaya, M. (2008). Regulation of n vitro calcium phosphate mineralization by combinatorially selected hydroxyapatite binding peptides, *biomacromolecules, 9*, 966-973.

Han, X.X., Jia, H.Y., Wang, Y.F., Lu, Z.C., Wang, C.X., Xu, V.Q.,Zhao, B. and Ozaki, Y. (2008). Analytical technique for label-free multi-protein detection based on western blot and surface enhanced Raman scattering, *Anal. Chem., 80*, 2799-2804.

Han, X.X., Kitahama, Y., Itoh, T., Wang, C.X., Zhao, B. and Ozaki, Y. (2009). Protein mediated sandwich strategy for surface enhanced Raman Scattering: application for versatile protein detection, *Anal. Chem., 81*, 3350-3355.

Han, X.X., Zhao, B. and Ozaki, Y. (2009). Surface-enhanced Raman scattering for protein detection, *Anal Bioanal Chem, 394*, 1719-1727.

Hnilova, M., Oren, E., Seker, U.O.S., Wilson, B.R., Collino, S., Evans, J.S., Tamerler, C. and Sarıkaya, M., (2008). Effect of molecular conformations on the adsorption behavior of gold-binding peptides, *Langmuir, 24*, 12440-12445.

Hossain, M.K. and Ozaki Y. (2009). Surface enhanced Raman scattering: facts and trends, *Current Science, 97*, 192-201.

Ignat, T., Miu, M., Kleps, I, Bragaru, A., Simion M. and Danila M. (2010). Electrochemical characterization of BSA/11-mercaptoundecanoic acid on Au electrode, *Materials Science and Engineering B, 169*, 55-61.

Israelachvili, J., (1992). *Intermolecular and surface forces*, 2nd Ed. Academic Press Inc., San Diego.

Iosin, M., Toderas, F., Baldeck, P.B. and Astilean, S. (2009). Study of protein–gold nanoparticle conjugates by fluorescence and surface-enhanced Raman scattering, *Journal of Molecular Structure, 924*, 196-200.

Iosin, M., Canpean, V. & Astilean, S. (2011). Spectroscopic studies on pH- and thermally induced conformational changes of Bovine Serum Albumin adsorbed onto gold nanoparticles, *Journal of Photochemistry and Photobiology A: Chemistry, 217*, 395-401.

Jain, P.K., Huang,W., and El-Sayed, M. (2007). On the universal scaling behavior of the distance decay of plasmon coupling in metal nanoparticle pairs: a plasmon ruler equation, *Nano Letters, 7*, 2080-2088.

Jain, P.K., Lee, K.S., El-Sayed, I.H. and El-Sayed, M.A. (2006). Calculated Absorption and Scattering Properties of Gold Nanoparticles of Different Size, Shape, and Composition: Applications in Biological Imaging and Biomedicine, *J. Phys. Chem. B, 110*, 7238-7248.

Jeanmaire, D. L. and Van Duyne, R. P., (1977). Surface Raman spectroelectrochemistry: Part I. Heterocyclic, aromatic, and aliphatic amines adsorbed on the anodized silver electrode, *J. Electroanal. Chem., 84*, 1–20.

Jessensky, O., Müler, F. and Gösele, U. (1998). Self-organized formation of hexagonal pore arrays in anodic alumina, *Appl. Phys. Lett., 72*, 1173-1175.

Kahraman, M., Sur, I. and Çulha, M. (2010). Label-free detection of proteins from self-assembled protein-silver nanoparticle structures using surface enhanced raman scattering, *Anal. Chem, 82*, 7596-7602.

Keating, C., Kovaleski, K.M. and Natan, M. (1998). Protein:colloid conjugates for surface enhanced Raman scattering: Stability and control of protein orientation, *J. Phys. Chem, 102*, 9404-9413.

Keller, F., Hunter, M.S. and Robinson D.L. (1953). Structural features of oxide coatings on aluminum, *J. Electrochem. Soc., 100*, 411-419.

Kenan, D.J., Walsh, E.B., Meyers, S.R., O'Toole, G.A., Carruthers, E.G., Lee, W.K., Zauscher, S. Prata, C.A.H. & Grinstaff, M.W. (2006). Peptide-geg amphiphils as cytophobic coatings for mammalian and bacterials cells, *Chem Bio, 13*, 695-700

Kneipp, K. (2007). Surface enhanced Raman scattering, *Physics Today, 60*, 40-46.

Kinalwa, M., Blanch, E.W. and Doig, A.J. (2011). Determination of protein fold class from Raman or Raman optical activity spectra using random forests, *Protein science, 20*, 1668-1674.

Kneipp, K., Haka, A.S., Kneipp, H., Badizadegan, K., Yoshizawa, N., Boone, C., et al., (2002). Surface-enhanced Raman Spectroscopy in single living cells using gold nanoparticles, *Applied Spectroscopy, 56*, 150-154.

Kneipp, K., Kneipp, H., Manoharan, R., Hanlon, E.B., Itzkan, I., Dasari, R.R., & Feld, M.S. (1998). Extremely large enhancement factors in surface-enhanced Raman scattering for molecules on colloidal gold clusters, *Applied Spectroscopy, 52*, 1493-1497.

Kneipp, K., Wang, Y., Dasari, R.P., and Feld, M.S. (1995). Approach to single-molecule detection using surface-enhanced resonance Raman-scattering (SERRS) - a study using Rhodamine 6G on colloidal silver, *Applied Spectroscopy, 49*, 780-784.

Krishnan, R.S., and Shankar, R.K. (1981). Raman Effect: History of the discovery, *Journal of Raman Spectroscopy, 10,* 1-8.

Ko., H., Singamaneni, S., and Tsukruk, V.V. (2008). Nanostructured surfaces and assemblies as SERS media, *Small, 4,* 1576-1599.

Kulp, J.L., Sarıkaya, M. And Evans, J.S. (2004). Molecular characterization of a prokaryotic polypeptide sequnce that catalyzes au crystal formation, *J. Matter Chem*., *14,* 2325-2332.

Larkin, P. (2011). Infrared and Raman spectroscopy principles and spectral interpretation, USA, Elsevier.

Laurent, G., Félidj, N., Aubard, V. and Lévi, G. (2005). Evidence of multipolar excitations in surface enhanced Raman scattering, *Physical Review B, 71,* 045430.

Lee, W., Ji, R., Gösele, U. and Nielsch, K. (2006).Fast fabrication of long-range ordered porous alumina membranes by hard anodization, *Nature Materials, 5,* 741-747.

Le Ru, E., and Etchegoin, P. (2008). *Principles of Surface-Enhanced Raman Spectroscopy: and related plasmonic effects*, Elsevier, Oxford, UK.

Le Ru, E., Blackie, E., Meyer, M., & Etchegoin, P. (2007). Surface enhanced raman scattering enhancement factors: a comprehensive study, *J. Phys. Chem*., *111,* 13794-13803.

Le Ru, E., Meyer, M., & Etchegoin, P. (2006). Proof of single-molecule sensitivity in surface enhanced raman scattering (sers) by means of a two-analyte technique, *Phys. Chem. B, 110,* 1944-1948

Lehn, J.M., (1990). Perspectives in Supramolecular Chemistry—From Molecular Recognition towards Molecular Information Processing and Self-Organization, *Angewandte Chemie, 29,* 1304-1319.

Li, X., Xu, W., Zhang, J., Jia, H., Yang, B., Zhao, B., Li, B., & Ozaki, Y. (2004). Self-assembled metal colloid films: two approaches for preparing new SERS active substrates, *Langmuir, 20,* 1298-1304.

Lin, X., Cui, Y., Xu, Y.,Ren,B., & Tian, Z. (2009). Surface-enhanced Raman spectroscopy: substrate-related issues, *Anal. Bioanal. Chem., 394,* 1729-1745.

Link, S., Mohamed, M.B., and El-Sayed, M.A. (1999). Simulation of the optical absorption spectra of gold nanorods as a function of their aspect ratio and the effect of the medium dielectric constant, *J. Phys. Chem. B, 103,* 3073-3077.

Lippert J.L., Tyminski, D. and Desmeules, P.J. (1975). Determination of the secondary structure of proteins by laser Raman spectroscopy, *Journal of American Chemical Society, 98*, 7075-7080.

Long, D.A. (2002). *The Raman effect: A unified treatment of the theory of Raman scattering by molecules*, West Sussex, England, John Wiley & Sons Ltd.

Luo, H., Park, S., Chan, Y.H., and Weaver, M.J. (2000). Surface oxidation of platinum-group transition metals in ambient gaseous environments: role of electrochemical versus chemical pathways, *J. Phys. Chem. B., 104*, 8250-8258.

Maiera, S.A. and Atwater, H. A. (2005). Plasmonics: Localization and guiding of electromagnetic energy in metal/dielectric structures, *Journal of Applied Physics 98*, 011101.

Maiti, N.C., Apetri, M.M. and Zagorski, M.G. (2004). Raman Spectroscopic Characterization of Secondary Structure in Natively Unfolded Proteins: r-Synuclein, *Journal of American Chemical Society, 126*, 2399-2408

Masuda, H., and Fukuda, K. (1995). Ordered metal nanohole arrays made by a 2-step replication of honeycomb structures of anodic alumina, *Science, 268*, 1466-1468.

McQuillan, A.J. (2009). The discovery of surface-enhanced Raman scattering, *Notes Rec. R. Soc., 63*, 105-109.

Menzies, A.C. (1930). The Raman effect, *Nature, 125*, 205-207.

Michnik ʾ A., Michalik, K. and Drzazga, Z. (2005). Stability of bovine serum albumin at different pH, *Journal of Thermal Analysis and Calorimetry, 80*, 399-406.

Miranda, M. M., Gellini, C. and Innocenti, M. (2012). *SERS spectroscopy and microscopy in Raman Spectroscopy for Nanomaterials Characterization*, pp. 553-586, Ed. Kumar, S. S. R., Springer-Verlag Berlin Heidelberg.

Mohanty, U.S. (2011). Electrodeposition: a versatile and inexpensive tool for the synthesis of nanoparticles, nanorods, nanowires, and nanoclusters of metals, *Journal of Applied Electrochemistry, 41*, 257-270.

Morton, S. M., and Jensen, L. (2008). Understanding the molecule-surface chemical coupling in SERS, *J. Am. Chem. Soc., 131*, 4091-4098.

Moskovits, M. (1978). Surface roughness and the enhanced intensity of Raman scattering by molecules adsorbed on metals, *J. Chem. Phys. 69*, 4159-4162.

Moskovits, M. Tay, L.L., Yang, J. & Haslett, T. (2002). SERS and the single molecule in *Optical properties of nanostructures random media*, 82, p.215-226, Ed Shalaev, V.M., Springer, Berlin.

Moskovits, M. (2005). Surface-enhanced Raman spectroscopy: a brief retrospective, *J. Raman Spectrosc., 36,* 485–496.

Munro, C.H., Smith, W.E., Garner, M., Clarkson, J., and White P.C. (1995). Characterization of the surface of a citrate-reduced colloid optimized for use as a substrate for surface-enhanced resonance raman scattering, *Langmuir, 11*, 3712-3720.

Nakamura, K., Era, S., Ozaki, Y., Sogami, M., Hayashi, T. and Murakami, M. (1997). Conformational changes in seventeen cysteine disulfide bridges of bovine serum albumin proved by Raman spectroscopy, *FEBS Letters, 417*, 375-378.

Natan, M.J. (2006). Concluding remarks Surface enhanced Raman scattering, *Faraday Discuss., **132**,* 321-328.

Naya,M., Tani, T., Tomaru, Y., Li, J. and Murakami, N. (2008). Nanophotonics bio-sensor using gold nanostructure, *Proceedings Of The Society Of Photo-Optical Instrumentation Engineers (Spie), 7032,* 321-321.

Newhouse, R.J. and Zhang, J.Z. (2012). Optical Properties and Applications of Shape-Controlled Metal Nanostructures, *Reviews in Plasmonics, 2010*, 205-238.

Nie, S. and Emory, S. R., (1997). Probing single molecules and single nanoparticles by surface-enhanced Raman scattering, *Science*, *275*, 1102–1106.

Oh H., Jang, K., Lee, J., Ki, B., Heo, C., Kwon, S. and Chi, C. (2006). Effects of annealing treatment of aluminum substrate on nanopore arrangements in anodic alumina, *Solid State Phenomena, 118,* 549-554.

Ortiz, C., Zhang, D., Xie, Y., Ribbe, A. and Ben-Amotz, D. (2006). Validation of drop coating deposition Raman method for protein analysis, *Analytical Biochemistry,353*, 157-166.

O'Sullivan, J.P. and Wood, G.C. (1970). The morphology and mechanism of formation of porous anodic films on aluminium, *Proc. R. Soc. Lond*. A, *317*, 511-543.

Otto, A. (2002). What is observed in single molecule SERS, and why, *J. Raman Spectrosc*., *33*, 593–598

Otto, A. (1984). Surface-enhanced raman-scattering classical and chemical origins, *Topics in Apllied Physics, 54*, 289-418.

Patermarakis, G., and Karayannis, H.S. (1995). The mechanism of growth of porous anodic Al_2O_3 films on aluminum at high film thicknesses, *Electrochemica Acta*, *40*, 2647-2656.

Pavel, I., McCarney, E., Elkhaled, A., Morrill, A., Plaxco, K., & Moskovits M. (2008). Label-free SERS detection of small proteins modified to act as bifunctional linkers, *J. Phys. Chem*, *112*, 4880-4883.

Peelle, B.R., Krauland, E.M., Wittrup, K.D., and Belcher, A.M. (2005). Probing the interface between biomolecules and inorganic materials using yeast surface display and genetic engineering, *Langmuir*, *21*, 6929-6933.

Pelton, J. T. and McLean, L. R. (2000). Spectroscopic methods for analysis of protein secondary structure, *Analytical Biochemistry*, *277*, 167-176.

Pinzaru, S.C., Peica, N., Schimidt, U. and Kiefer, W. (2007). New substrate handling and micro-Raman sensing methods for biomolecular analysis, *journal of optoelectronics and advanced materials*, *9*, 768-771.

Pristinski, D., Tan, S., Erol, M., Du, H. and Sukhishvili, S. (2006). In situ SERS study of Rhodamine 6G adsorbed on individually immobilized Ag nanoparticles, *journal of Raman Spectroscopy*, *37*, 762-770.

Podstawka, E., Borszowska, R., Grabowska, M., Drag, M., Kafarski, P. and Proniewicz, L.M. (2005). Investigation of molecular structure and adsoption mmechanisms of phosphonodipeptides by surface-enhanced Raman, Raman and infrared spectroscopies, *Surface Science*, *599*, 207-220.

Raman, C.V. (1922). Molecular diffraction of light, University of Calcutta, Calcutta, India.

Raman, C.V. (1922). On the molecular scattering of light in water and the colour of the sea, *Proceedings of the Royal Society of London [A]*, *101*, 64–80.

Raman, C. V. (1928). A new radiation, *Indian J. Phys. 2*, 387-398.

Raman, C.V. (1930). *The molecular scattering of light*, Nobel Lecture.

Rayleigh, J.S. (1922). On the transmission of light through an atmosphere containing small particles in suspension, and on the origin of the blue of the sky, *Philosophical Magazine*, *47*, 375–384.

Robertson, S. and Ritchie,I. (1997). The role of iron(III) and tartrate in the zincate immersion process for plating aluminium, *Journal of Applied Electrochemistry*, *27*, 799-804.

Saedi, A. and Ghorbani, M. (2005). Electrodeposition of Ni–Fe–Co alloy nanowire in modified AAO template, *Materials Chemistry and Physiscs, 91*, 417-423.

Saini, G.S.S., Sharma, A., Kaur, S., Bindra, K.S., Sathe, V., Tripathi, S.K. and Mhahajan, C.G. (2009). Rhodamine 6G interaction with solvents studied by vibrational spectroscopy and density functional theory, *Journal of Molecular Structure, 931***,** 10-19.

Sane, S. U., Steven, M. C. and Przybycien, T. M. (1999). A holistic approach to protein secondary structure characterization using amide I band Raman spectroscopy, *Analytical Biochemistry, 269*, 255-272.

Sarıkaya, M., Tamerler, C., Jen, A.K.Y., Schulten, K. and Baneyz, F. (2003). Molecular Biomimetics: Nanotechnology through biology, *Nature Materials, 2*, 577-585.

Sarıkaya, M., Tamerler, C., Schwartz, D. T., and Baneyx, F. (2004). Materials assembly and formation using engineered polypeptides, *Annual reviews of materials research, 34*, 373-408.

Schatz, G., Young, M.A. and Van Duyne, P.R. (2006) Surface enhanced Raman Sacattering Physics and applications, Topics Appl. Phys. **103**, 19-46, Eds. Kneipp, K., Moskovits, M. and Kneipp, H. Springer-Verlag Berlin Heidelberg.

Sengupta,A., Thai, K.C., Sastry, M.S.R., Matthaei, J.F., Schwarts, D.T., Davis, E.J. and Baneyx, F. (2008). A genetic approach for controlling the binding and orientation of proteins on nanoparticles, *Langmuir*, *24*, 2000-2008.

Shafer-Peltier, K.E., Haynes, C.L., Glucksberg, M.R., & Van-Duyne, R.P. (2003). Toward a glucose biosensor based on surface-enhanced Raman scattering, *Journal of the American Chemical Society, 125*, 588-593.

Sharma, B., Frontiera, R.R., Henry, A., Ringe, E., & Van-Duyne, R.P. (2012). SERS: Materials, applications and the future, *Materials Today, 15*, 16-25.

Singh, R. (2002). C.V. Raman and the discovery of the Raman effect, *Physics in Perspective*, **22**, 399-420.

Sivashanmugan, K., Liao, J., You, J. & Wu, C. (2013). Focused-ion-beam-fabricated Au/Ag multilayered nanorod array as SERS-active substrate for virus strain detection, *Sensors and Actuators B: Chemical, 181*, 361-367.

Smith, E., and Dent, G. (2005). *Modern Raman spectroscopy-A practical approach*, West Sussex, England, John Wiley & Sons Ltd.

So, C.R., Tamerler, C. and Sarıkaya, M., (2009). Adsorption, diffusion and self-assembly of an engineered gold-binding peptide on Au (111) investigated by atomic force microscopy, *Angew. Chem.Int. Ed., 48,* 5174-5177.

So, C.R., Kulp, J. L., Oren, E. E., Zareie, H., Tamerler, C., Evans, J. S. and Sarıkaya, M., (2009). Molecular recognition and supramolecular self assembly of a genetically engineered gold binding peptide on Au {111}, *Acs Nano, 3,* 1525-1531.

Soleimany, L., Dolati, A., Ghorbani, M. (2010). A study on the kinetics of gold nanowire electrodeposition in polycarbonate templates, *Journal of Electroanalytical Chemistry, 645,* 28-34.

Stewart, S. and Fredericks, P.M. (1999). Surface enhanced Raman spectroscopy of peptides and proteins adsorbed on electrochemically prepared silver surfaces, *Spectrochimica Acta, 55,* 1615-1640.

Sulka, G.D. (2008). Highly ordered anodic porous alumina formation by self-organized anodizing in *Nanostructured Materials in Electrochemistry,* Eds. Eftekhari, A., Wiley-VCH Verlag GmbH & Co. KGaA, Weinheim, Germany.

Suzuki, N., Gamble, L., Tamerler, C., Sarıkaya, M., Castner, D. and Ohuchi, F.S., (2007). Adsorption of genetically engineerd proteins studied by time-of-flight secondary ion mass spectroscopy Part B, hierarchical cluster analysis, *Surf. Interface Anal., 39,* 427-433.

Tamerler, C. and Sarıkaya, M., (2007). Molecular Biomimetics: Utilizing nature's molecular ways in practical engineering, *Acta Biomateriala, 3,* 289-299.

Tamerler, C. and Sarıkaya, M., (2008). Molecular Biomimetics: Genetic synthesis, assembly and formation f materials using peptides, *MRS Bull, 33,* 504-512.

Tamerler, C.Duman, M., Ören, E:, Gungormuş, M., Xiong, X., Kacar., T., Parviz, B.A. & Sarıkaya, M. (2006). Material specificity and directed assembly of a gold binding peptide, *Small, 2,* 1372-1378.

Tamerler, C. and Sarıkaya, M., (2009). Molecular Biomimetics: Nanotechnology and bionanotechnology using genetically engineered peptides, *Philosophical Transactions of the Royal Society a-Mathematical Physical and Engineering Sciences, 367,* 1705-1726

Tao, A., Kim, F., Hess, C., Goldberger, J., He, R.R., Sun, Y.G., Xia, Y.N., & Yang, P.D. (2003). Langmuir-Blodgett silver nanowire monolayers for molecular sensing using surface-enhanced Raman spectroscopy, *Nano Letters, 3,* 1229-1233.

Tao, A., Sinsermsuksakul, P., and Yang, P. (2007). Tunable plasmonic lattices of silver nanocrystals, *Nature Nanotechnology, 2*, 435-440.

Thomas Jr., G. J. (1999). Raman spectroscopy of protein and nucleic acid assemblies, *Annu. Rev. Biophys. Biomol. Structure, 28*, 1-27

Thompson, G.E. (1997). Porous anodic alumina: fabrication, characterization and applications, *Thin solid films, 297*, 192-201.

Tom, T.R., Samal A.K., Sreeprasad, T.S. and Pradeep, T. (2007). Hemoprotein bioconjugates of gold and silver nanoparticles and gold nanorods: structure-function correlations, *Langmuir,23,* 1320-1325.

Url-1 <http://www.horiba.com/scientific/products/raman-spectroscopy/tutorial-faqs/raman-faqs/what-is-a-ccd-detector/>, date retrieved 11.01.2013.

Url-2 <http://www.pnas.com />, date retrieved 14.01.2013.

Wang, F. and Shen, Y.R. (2006). General Properties of Local Plasmons in Metal Nanostructures, *Physical Review Letters, 97*, 206806-1-4.

Williams, R. W., and Hendrickson, W. A. (1984). Raman spectroscopic analysis of the secondary structure in Panulirus interruptus hemocyanin, *FEBS letters.* 165**,** 223-226

Whaley, S.R., English, D.S., Hu, E.L., Barbara, P.F. and Belcher, A. M. (2000). Selection of peptides with semiconductor binding specificity for directed nanocrystal assembly, *Nature, 405***,** 665-668.

Wustholz, K.L., Henry, A.L., McMahon, J.M., Freeman, R.G., Valley, N., Piotti, M.E., et al. (2010). Structure-activity relationships in gold nanoparticle dimers and trimers for surface-enhanced Raman spectroscopy, *journal of American Chemical Society, 132*, 10903-10910.

Van Duyne, R.P. (1979). Laser Excitation of Raman Scattering from Adsorbed Molecules on Electrode Surfaces, in *Chemical and Biochemical Applications of Lasers*, 4, p.101-185, Ed. CB Moore, Academic Press, New York .

Vlckova, B., Moskovitz, M., Pavel, I., Siskova, K., Sladkova, M. & Slouf, M. (2008). Single-molecule surface-enhanced Raman spectroscopy from a molecularly-bridged silver nanoparticle dimer, *Chemical Physics Letters, 455***,** 131–134.

Vo-Dinh, T., Stokes, D.L., Griffin, G.D., Volkan, M., Kim, U.J., and Simon, M.I. (1999). Surface-enhanced Raman scattering (SERS) method and instrumentation for genomics and biomedical analysis, *Journal of Raman Spectroscopy, 30*, 785-793.

Zhang, D., Xie, Y:, Mrozek,M., Ortiz, C., Davisson, J., and Ben-Amotz, D. (2003).Raman detection of proteomic analytes, *Anal Chem, 57*, 5703-5709.

Zhu, X.F., Li, D.D., Song, Y. and Xiao, Y. H. (2005). The study on oxygen bubbles of anodic alumina based on high purity aluminum, *Materials Letters, 59*, 3160–3163.

Zhu, G., Zhu, X., Fan, Q. and Wan, X. (2011). Raman spectra of amino acids and their aqueous solutions, *Spectrochimica Acta part A: Molecular and biomolecular Spectroscopy,78*, 1187-1195.

CURRICULUM VITAE

Name Surname: Zehra Beril Akıncı

Place and Date of Birth: Istanbul, 22.05.1981

Address: Ferahevler Erciyes sok 19/6 Tarabya Istanbul

E-mail: berilakinci@gmail.com

B.Sc.: Metallurgical and Materials Engineering, Istanbul Technical University, 2001-2005

M.Sc.: Materials Science and Engineering, Istanbul Technical University, 2005-2007

List of Publications and Patents:

International Journal Papers

Bayata F., **Akıncı Z. B**., Donatan S., Urgen M., A novel free-standing nanowire substrate with surface enhanced Raman scattering (SERS) activity, Materials Letters 67 (2012) 387–389

Akıncı Z. B., Urgen M, A Simple Method for the Production of AAO Templates for DC Electrodeposition of Nanostructures, *ECS Electrochemistry Letters*, ***3*** (11) D1-D4 (2014)

International Conference Papers

Z. Beril Akıncı, Mustafa Urgen, Investigation of the Aspect Ratio – Surface Enhanced Raman Excitation Relationship on Free Standing Gold Nanowire Arrays, October 22-24 2012, International Conference and Expo on Materials Science & Engineering, Chicago, USA

Z. Beril Akıncı, Candan Tamerler, Mustafa Urgen, Probing the protein orientation on free standing gold nanowire with surface enhanced Raman

spectroscopy, Oral presentation, 25-27 June 2012, 8th Nabotechnology and Nanoscience Congress, NanoTr VIII, Ankara, Turkey

Z. Beril Akıncı, Mustafa Urgen, A Novel Method For The Selective Opening Of The Barrier Layer In Porous Anodic Alumina, 27 June-01 July 2011, 7th Nabotechnology and Nanoscience Congress, NanoTr VII, Istanbul, Turkey

Z. Beril Akıncı, Senem Donatan, Mustafa Urgen, Freestanding Gold Nanowire Substrate with Surface Enhanced Raman Scattering Activity, October 9-14, 2011, 220th ECS Meeting, Boston, MA.

Z. Beril Akıncı, Senem Donatan, Mustafa Urgen, International Workshop on Molecular Biomimetics and Bionanotechnology II, 2007 Maslak, ITU Turkey, Poster presentation, Best poster selected for short oral presentation